

Advanced Construction Technologies

Edited by
Husain Abbas and TAN Kiang Hwee



TRANS TECH PUBLICATIONS

Advanced Construction Technologies

Edited by
Husain Abbas
TAN Kiang Hwee

Advanced Construction Technologies

Selected, peer reviewed papers from the
2014 4th International Conference on
Structures and Building Materials
(ICSBM 2014),
March 15-16, 2014, Guangzhou, China

Edited by

Husain Abbas and TAN Kiang Hwee



Copyright © 2014 Trans Tech Publications Ltd, Switzerland

All rights reserved. No part of the contents of this publication may be reproduced or transmitted in any form or by any means without the written permission of the publisher.

Trans Tech Publications Ltd
Kreuzstrasse 10
CH-8635 Durnten-Zurich
Switzerland
<http://www.ttp.net>

Volumes 919-921 of
Advanced Materials Research
ISSN print 1022-6680
ISSN cd 1022-6680
ISSN web 1662-8985

Full text available online at <http://www.scientific.net>

Distributed worldwide by

Trans Tech Publications Ltd
Kreuzstrasse 10
CH-8635 Durnten-Zurich
Switzerland

Fax: +41 (44) 922 10 33
e-mail: sales@ttp.net

and in the Americas by

Trans Tech Publications Inc.
PO Box 699, May Street
Enfield, NH 03748
USA

Phone: +1 (603) 632-7377
Fax: +1 (603) 632-5611
e-mail: sales-usa@ttp.net

Preface

The International Conference on Structures and Building Materials (ICSBM) is the premier forum for the presentation of new advances and research results in the fields of civil engineering and materials. This conference series bring together international scientific community, academics and practitioners, researchers and students and provide an opportunity to discuss and share recent advances in both research and practice about all aspects of building materials and diagnostics of civil engineering, building, structures and geotechnics. After the very successful previous issues ICSBM'2011 (Guangzhou, China), ICSBM'2012 (Hangzhou, China) and ICSBM'2013 (Guiyang, China), the ICSBM'2014: 4th International Conference on Structures and Building Materials was held successfully in Guangzhou, China, from March 15 to 16, 2014.

This book is a collection of accepted papers. All these accepted papers were subjected to strict peer-reviewing by 2-4 expert referees. The book is divided into 24 chapters, including Structural Engineering, Monitoring and Control of Structures, Structural Rehabilitation, Retrofitting and Strengthening, Reliability and Durability of Structures, Disaster Prevention and Mitigation, Bridge Engineering, Geotechnical and Geological Engineering, Tunnel, Subway and Underground Facilities, Seismic Engineering, Roads, Railway Engineering and Traffic Engineering, Hydrology, Coastal and Hydraulic Engineering, Computational Mechanics and Mathematical Modeling, Construction Technology, Project Management and Engineering Management, Architectural Design and Its Theory, Urban Planning and Design, Landscape Planning and Design, Architectural Environment, Eco-Building and Green Building, Building Energy Saving Technology, Construction Materials Research, Materials Science, Data and Signal Processing, Environmental Engineering and Wastewater Treatment, etc. This book will not only provide the readers a broad overview of the latest advances but also provide the researchers a valuable summary and reference in this field.

We would like to express our sincere appreciations to all the authors for their contributions to this volume. We are indebted to all the referees for their constructive comments on the papers. Thanks are also given to Trans Tech Publications for producing this volume.

The Committee of ICSBM 2014

2014 4th International Conference on
Structures and Building Materials
(ICSBM 2014)

Conference Organization

Chairmen

Prof. Husain Abbas, Chair Professor, King Saud University

Prof. TAN Kiang Hwee, National University of Singapore

Prof. Genda Chen, Missouri University of Science and Technology, USA

Technical and Organizing Committee

Prof. Xiuli Du, Beijing University of Technology, China

Prof. Yong Huang, Guizhou University, China

Prof. Jianjun Zheng, Zhejiang University of Technology

Prof. Chaohe Chen, Hainan University, China

Prof. Weiliang Jin, Zhejiang University, China

Prof. Jianguo Nie, Tsing Hua University, China

Prof. Bo Wu, South China University of Technology, China

Prof. Shilang Xu, Zhejiang University, China

Prof. Yiqiang Xiang, Zhejiang University, China

Prof. Jianjun Zheng, Zhejiang University of Technology

Prof. Boyang Ding, Zhejiang University of Technology

Prof. Minyun Hu, Zhejiang University of Technology

Prof. Zhiyong Dong, Zhejiang University of Technology

Prof. Xinjun Zhang, Zhejiang University of Technology

Prof. Fuying Liu, Zhejiang University of Technology

Academician Prof. Wei Sun, Southeast University, China

Prof. Ailin Zhang, Beijing University of Technology, China

Prof. Weiming Yan, Beijing University of Technology, China
Prof. Bin Xu, Hunan University, China
Prof. Feng Fan, Harbin Institute of Technology, China
Prof. Lijuan Li, Guangdong University of Technology
Prof. Yiqiang Xiang, Zhejiang University, China
Prof. Peiyu Yan, Tsinghua University, China
Prof. Feng Liu, Guangdong University of Technology
Prof. Jun Deng, Guangdong University of Technology
Prof. Jianxun Ma, Xi'an Jiaotong University, China
Prof. Jichao Zhang, Guangzhou University, China
Prof. Linhai Han, Tsinghua University, China
Prof. Wenguang Liu, Shanghai University, China
Prof. Yanpeng Zhu, Lanzhou University of Technology, China
Prof. Yun Zhou, Guangzhou University, China
Prof. Zhengliang Li, Chongqing University, China
Prof. Zhihua Chen, Tianjin University, China
Prof. Guangfan Li, Hainan University, China
Prof. Jiping Hao, Xi'AN Univ. of Architecture and Tech., China
Prof. Jihong Ye, Southeast University, China
Prof. Zixiong Guo, Hua Qiao University, China
Prof. Xuejun Zhou, Shandong Jianzhu University, China
Prof. Ayman Mosallam, Univ of California Irvine, USA
Prof. Aftab Mufti, University of Manitoba, Canada
Prof. Antoine E. Naaman, University of Michigan, USA
Prof. A. Kaveh, Iran University of Science & Technology, Iran
Prof. Aftab Mufti, University of Manitoba, Canada
Prof. B. H. V. Topping, Heriot-Watt University, Edinburgh, UK
Prof. David Hui, University of New Orleans, USA
Prof. Faris Albermani, University of Queensland, Australia

Prof. Hamid Ronagh, The University of Queensland, Australia
Prof. Han-Bin Ge, Meiju University, Japan
Prof. I. E. Harik, University of Kentucky, USA
Prof. J-G. Teng, Hong Kong Polytechnic University, Hong Kong
Prof. J. H. Bungey, University of Liverpool, Liverpool, UK
Prof. Jian-Fei Chen, the University of Edinburgh, UK
Prof. Kang Seok Lee, Chonnam National University, South Korea
Prof. K. J. Bathe, Massachusetts Institute of Technology, USA
Prof. Lawrence C. Bank, University of Wisconsin-Madison, USA
Prof. Luciano Feo, University of Salerno, Italy
Prof. M. N. Soutsos, University of Liverpool, Liverpool, UK
Prof. Mark G Stewart, The University of Newcastle, Australia
Prof. Marcus M.K. Lee, the University of Southampton, UK
Prof. R. Sri Ravindra rajah, University of Technology, Australia
Prof. Ramiro Sofronie, University of Bucharest, Romania
Prof. Steve.G.Millard, University of Liverpool, UK
Dr.Tianjian Ji, The University of Manchester, UK
Prof. Tamon UEDA, Hokkaido University, Japan
Prof. Tan Kiang Hwee, National University of Singapore
Prof. Tim Ibell, University of Bath, UK
Prof. Zong Woo Geem, iGlobal University, USA
Prof. Zhi-Shen Wu, Ibaraki University, Japan

Table of Contents

Preface and Conference Organization

Chapter 1: Structural Engineering

A Nonlinear Model for Beam-Column Joint Based on OpenSees Y.Z. Ju, Y. Mu and D.H. Wang	3
A Study on the Effect of a Dyke Reinforced by Geotextile-Encased Sand Columns F. Ouyang, J.W. Bi, J.W. Han and W.M. Liao	7
Analysis of a Transmission Tower Structure with Dynamic Elastic-Plastic Time History Method Z.G. Xu, K. Qin and C.G. Deng	10
Analysis of Composite Beam with Different Web Openings W.Y. Liao, D.H. Zhou and L.Q. Li	15
Analysis of Reconstruction and Reinforcement Design for a Thermal Power Plant Boiler Frame J.L. Wu, P.Z. Cao and C. Liu	19
Axial Strains in FRP-Confined Normal- and High-Strength Concrete: An Examination of Strain Measurement Methods T. Vincent and T. Ozbakkaloglu	23
Comparison of Stress-Strain Relationships of FRP and Actively Confined High-Strength Concrete: Experimental Observations J.C. Lim and T. Ozbakkaloglu	29
Construction Control of a Continuous Beam Arch Composite Bridge C.Y. Zhou, J.R. Yang, W.M. Zhu and J. Shi	35
Construction Technique of Cast <i>In Situ</i> RC Grillage Shear Wall Building Formed with Thermal Insulation Hollow Blocks W.J. Zhang, Q. Zhang and P.R. Fu	39
Damage Identification Based on Power Spectral Density Sensitivity Analysis of Structural Responses W.H. Chen, C.Y. Ding, B.Q. He, Z.R. Lv and J.K. Liu	45
Damage Location Identification of Truss Structure Based on Strain Modal Method B.D. Ding, M. Tang and Y.N. Shang	51
Design Analysis of Steel Frame for Denitrification through Existing Structure C. Liu and P.Z. Cao	58
Design and Numerical Simulation on Concrete Two-Way Slab Strengthened with Partially Bonded Steel Plate J.H. Hu and X.C. Li	64
Discussion on the Rationality Simplified Calculation Method of Reinforced Concrete Two-Way Slab S.Z. Liu	68
Displacement Control Technology on High-Rise Steel Structure about Main Power House of Thermal Power Plant H.Q. Liu, W.B. Li and K. Ma	72
Dynamic Analysis of Tapered Plates Based on Higher Order Beam Theory S.M. Ibrahim, Y.A. Al-Salloum and H. Abbas	79
Effect of Loading Pattern on Performance of FRP-HSC-Steel Double Skin Tubular Columns B.A. Louk Fanggi and T. Ozbakkaloglu	83
Evaluation of Snow Load Using a Wind Tunnel on the Arched House S.Y. Paek, J.Y. You, K.P. You and Y.M. Kim	88
Evaluation of the Fire Resistance of H-Section Made of High Strength Structural Steels with a Difference of Length I.K. Kwon	95

Experiment Design of the Scale Model of the RC Frame Structure under Internal Blast Loading	
X.W. Zhu, B. Jia, T. Liu and J.L. Tao	99
Experimental Study of Reinforcement Effect of Injured Frame Joints under Different Axial Compression Ratio	
M.X. Fang, Z.Y. Yang, Z.F. Chang, S.H. Liu and G. Wang	106
Experimental Study of Strengthening of Reinforced Concrete Beams with Externally Bonded GFRP Sheets	
H.Y. Hu, Y.C. Zhang and Z.M. Huang	115
Experimental Study on Early-Age Crack of RC Using TSTM	
N.N. Shi and D.H. Huang	119
Experimental Study on Glued Bamboo Beam	
L.F. Zhang, H.T. Li, J.W. Su, X.Y. Chen, W. Liu, M.H. Xu, J. Dai, F. Wu, Z. Song, B. Li, Z.Q. Zhou and J. Chen	123
Experimental Study on the Flexural Behavior of Stone Slabs with near Surface Mounted Steel Bar	
E.X. Dong, Z.F. Chen and M. Xu	128
Failure Analysis of Reinforced Concrete Beams Subjected to Explosion and Post-Explosion Fire	
J.K. Zhao, P. Yan, B. Gu and J. Gu	133
Finite Element Software for Optimization of Triangular Light Roof Truss Structure of Gymnasium	
T. Li and H. Wang	139
Geometric Nonlinear Shallow Shells for Variable Thickness Investigation	
L.U. Stupishin and A.G. Kolesnikov	144
Interfacial Slip Calculation of RC Beams Strengthened with FRP Plate under Mid-Span Concentrated Loads	
A.X. Liu and J. Yang	148
Isolation Performance Analysis of Concrete-Filled Steel Tubular Composite Structure Based on the Lead Rubber Bearing	
S.W. Duan, X. Tan and W. Huang	152
Lifting Point Optimization of Large Steel Truss on the Principle of Minimum Potential Energy	
X.C. Fan, H. Chen, Y. Liu and W.C. Lv	158
Non Shrinkage Self-Compacting Steel Box Concrete Application in a Landscape Tower	
S.J. Li, X.Y. Xu, W.J. Lu and Y.G. Fu	164
Nonlinear Buckling Analysis of Long-Span Suspended Latticed Intersected Cylindrical Shell	
M.L. Zhu and Y. Sun	169
Nonlinear Finite Element Method Ultimate Strength Analysis of Open Box Girders	
V.T. Vu and W.G. Wu	177
Nonlinear Numerical Study of Cold-Formed Lipped Channel Beam-Columns	
M. Chen, Z.B. Feng, Z. Zhou, Y.L. Wang and Q. Zhang	183
On Expected Performance of a Frame-Structure Made by All GFRP Pultruded Profiles	
A. dal Cin	188
Parametric Sensitivity Analysis of Long-Span Arch-Truss String Structure	
Z.X. Bai, X.M. Hou, S. Tian and J.Z. Wu	193
Performance Based Optimized Design of Steel Structure	
L.L. Zhang, X.G. Song and J.J. Zhang	199
Prediction Method of the Load Resisting Mechanisms in the Corroded RC Beams	
W. Dong, H. Oshita and T. Tsutsumi	203
Research on Compressible Flow around Cylinder and Truncated Cone with LES Method	
M. Zhao, J. Mao and G.W. Yang	210
Snow Wind Tunnel Experiment for Snowdrift Prediction of Domed Stadium	
S.Y. Paek, B.H. Nam, J.Y. You, K.P. You and Y.M. Kim	216
Stress and Stability Analysis of a Cooling Tower by ANSYS	
M.L. Cao and X.J. Qiu	222

Study on Collapse Numerical Simulation Method of Frame Structures Based on Explicit Dynamics K. Hu	226
Study on Dynamic Characteristics of a New Space Latticed Shell String Structure Y.L. Yao, G.Y. Ma and S.L. Dong	239
Study on New Reinforcing Method of Composite Beam with Web Openings under Negative Moment W.Y. Liao, D.H. Zhou and C.X. Han	243
Test Scheme and Result Analysis of New-Type Frame Structure with Column End of Steel-Concrete Composite Joint G.H. Lu and Z. Wang	247
The Dynamic Characteristic and Response's Discussion of External Prestressing Curved Beam M.Y. Huang	254
The Effect of Splicing Area Parameters on Mechanical Behavior of Beam-Column Connection with Cantilever Beam Splicing J.R. Pan, Z.T. Yang, L.Q. Zheng and R.B. Gao	258
The Numerical Simulation Experiment of Exploded in the Flat Box Sealed Structure Z. Wen, B. Jia, T. Liu and J.L. Tao	262
The Optimization Calculation and Analysis of Trough Solar Collector Bracket System G. Li, L.Y. Zhou and Z.D. Ai	267
Thermal Effect Test of Outer Compressive Ring of the Roof of Bao'an Stadium H. Deng, X.L. Sun, Y. Cao and X.L. Zhang	271
Transverse Free Vibration of Timoshenko Beams Resting on Viscoelastic Foundations L. Peng and Y. Wang	275
RPC Pole Composite Cross Arm Design and Wind-Induced Dynamic Analysis Y.Z. Ju, N. Tong and Q. Wu	280
Exterior-Template Design for Concrete Engineering in an Arched Structure D.Q. He and W.H. Wu	284
The Strain Change Rules of Full-Scale High Strength Concrete Frame Columns with High Axial Compression Ratios G.J. Zhang, Y.B. Jia and X.L. Lu	288
Upheaval Buckling Analysis of Buried Offshore Pipelines under High Temperature and High Pressure P. Liu, S.Y. Wu and L. Kang	292
A Case Study on the Use of Aluminum Forms in Nuclear Power Plant Construction G.H. Kim, H.M. Song and Y.S. Shin	296

Chapter 2: Monitoring and Control of Structures

A DE-Based Algorithm for Structural Damage Detection Y.M. Fu and L. Yu	303
Construction Monitoring of Prestressed Concrete Continuous Beam Bridge C.Q. Li, W.J. Ge, D.F. Cao and B.Y. Wang	308
Experimental Measurement of Two-Dimensional Circular Boundary Temperature Field by Acoustic Method L.W. Zhang, M.J. Wang and W. Cao	313
Knowledge of the Construction Technique of the Multiple Leaf Masonry Facades of Palazzo Ducale in Venice with ND and MD Tests G. Boscato, A. dal Cin, G. Riva, S. Russo and F. Sciarretta	318
Modal Parameter Identification of Concrete Filled Steel Tube Arch Bridge Based on Stochastic Subspace Method L.X. Wang and S.K. Di	325
Moving Force Identification Based on Firefly Algorithm C.D. Pan and L. Yu	329
Static Monitoring and Non-Destructive Test of a Historic Damaged Palace G. Boscato and A. dal Cin	334

Structural Damage Detection by Fusion of GA and PSO L. Yu and Y.M. Fu	338
Structural Diagnosis of a Historic Tower Hit by Earthquake A. dal Cin	344
Test of Thick Rubber Bearings on its Compressive Properties H.W. Chen, P. Pan, J.C. Liu, Y. Sakurai, M. Nakamura and N. Murota	348
The Vibration Modal Displacement Component Method of Identifying the Crack Damage from Simple Supported Beam Z.H. Fang and X.Y. Liu	355
Development of On-Site Fast Detector Used for Waterproof Membrane Joint Peeling Strength J.L. Xu, Y. Zheng, T.X. Wang, P. Du and Z.H. Liu	359
Analysis of Displacement Influence Line Characteristics of Simply Supported Beam with Local Damage K. Sun and Y.Q. Zhang	364
Detection and Monitoring Technologies of Bridge Cable Force and Disease Y. Zheng	369
Edge Detection Technology and its Application in the Model Test of Vehicle Bridge Coupled Vibration J. Wu and X.R. Yuan	373
Critical Application Technology of PIV in Dynamic Centrifugal Test and Design Method of Instrumentation Y.Z. Wang and X.M. Yuan	378
Detection of Unfavorable Karst Cavities in the Carbonaceous Bedrock Area at the Kaihua Segment of Hangzhou-Xinanjiang-Jingdezhen Expressway M. Xu, Z.H. Chen, B. Zeng, W.L. Ye and K.F. Chen	382
Ubiquitous Sensor Network for Construction Site Monitoring J.M. Shin, S.Y. Kim, G.H. Kim, M.G. Jung and D.W. Shin	388
Research on the Environmental Effects of GB-SAR for Dam Monitoring C. Xing, J.J. Huang and X.Q. Han	392

Chapter 3: Structural Rehabilitation, Retrofitting and Strengthening

A New Reinforcement Measure Suited for Space Truss with No-Fire Operation Z.Y. Mei, C.Q. Liu, X. Mi and P. Wu	401
Experimental Investigation on Axial Compressive Behavior of Masonry Column Strengthened by SGFRP Z. Zhang and Q. Gu	406
Experimental Investigation on Shear-Reinforced Masonry Sample with FRP Bars G. Boscato	411
Experimental Study on the Bonding Behavior of GFRP-to-Brick Interface J. Zhao, W.B. Sun, Q.Q. Zhu and H.B. Yong	416
Model's Calibration for Masonry Reinforced with FRP Mesh-Bars A. dal Cin	421
Reinforcement Planning Decision of Old Bridge Based on TOPSIS-AHP Method X.F. Liang and Y. Xu	426
Review of the Study on the FRP Strengthened Masonry Walls J. Zhao, W.B. Sun, H.B. Yong and Q.Q. Zhu	430
Simulation on Strengthening of a Cement Fresh Material Silo Y.S. Chen, L. Liu and X.L. Lei	434
The Concrete Protective Effect of Silane Impregnated Materials with Different Molecular Chain Structure H.S. Wang, W. Wang, R. Wang, W.B. Wang, L. Li and Q. Tian	439
Safety Evaluation of Reinforced Concrete Girder Bridge after Strengthened with Pasting Technology Z.M. Zhao, K.D. Liu, J.Y. Chai, L.L. Lei, Q. Wang, X.S. Qi and R.X. Liu	443

Chapter 4: Reliability and Durability of Structures

Application of Fuzzy Pattern Recognition in Spalling Risk Evaluation of Concrete Structures at High Temperature R.T. Li	451
Application of the Failure Assessment Method for Cracked Pipeline Y.Q. Bai, L.H. Lv, T. Wang and X.F. Zhang	455
Experimental Study on Influence of Bending Load on Chloride Ion Concentration of Concrete in Marine Environment H.Y. Jin, H.X. Zhuang, R.T. Liu, J.L. Shi and J.Z. Zhang	460
National Road 209 Line Shibi Mountain Bridge Concrete Anti-Carbonation Performance Analysis H. Liang, X.D. Liang and W.L. Du	465
Safety Assessment of Large-Scale Crude Oil Tank after Fire Process W.H. Wang, H.X. Li, Z.S. Xu and D. Liang	469
The Effect of Section Optimization on the Double Nonlinear Global Stability of Latticed Shell S.Y. Chen, X.Z. Liu, H.L. Wang and X.Y. Lu	473
The Influence of Main Components of Building under Residual Deformation in Subsidence Area J.B. Yu	477

Chapter 5: Disaster Prevention and Mitigation

Explosion Experimental Study Based on the Small Tailings Pond Model S.R. Lv, Q.N. Wei and K. Yang	485
Fire Resistance of Reinforced Concrete Column Exposed to Fire with Cooling Phase J.K. Zhao, P. Yan, D.P. Li and Y. Liu	491
Modeling of Mechanical Damage in Traditional Brickwork Walls after Fire Exposure F. Sciarretta	495
Research on HSE Risk Assessment and Control in Oil-Gas Drilling Operations F. Li and G. Zhang	500
Study on Fire Risk Assessment on Irradiation Room under Stuck Radioactive Sources X.L. Yao	507
Study on Fire Risk Assessment on Round Irradiation Room of Stacking under Stuck Radioactive Sources X.L. Yao	512
Wind Tunnel Test of Symmetrical Twin-Tower Tall Building Model J.G. Zhang and H.M. Zhuang	518
Work at Height in Safety Work Plan Management I. Tureková, V. Tomková and T. Bagalová	523

Chapter 6: Bridge Engineering

A Revised the B3 Creep Prediction Model Based on Short-Time Tests S.X. Hu, Q. Huang and S.F. Lin	529
An Analysis on the Deformation of an Arch Bridge under the Action of Live Load by Using ANSYS L.L. Duan, Y.M. Zhao and X.W. Wang	533
Dynamic Model Scheme Optimization Based on Fuzzy Decision Theory of Self-Anchored Cable-Stayed Suspension Bridge M. Feng	538
Effect of Wheel Pressure on Vibration of Straddle Monorail Transit Vehicle-Bridge System G. Liu, B. Jang, Z.H. Zhou and Q.Y. Zeng	542
Estimation Method for Prestress Loss of Externally Prestressed Composite Girder Bridges Y.M. Zhao, H.X. Li and X.W. Wang	547

Finite Element Simulation of Large Segment Hoisting Construction for Hong Kong-Zhuhai-Macao Bridge H.X. Li, L.L. Duan, X.W. Wang and B. Zhu	551
Hybrid Vibration Control of Self-Anchored Cable-Stayed Suspension Bridge M. Feng	556
Influence of Tensioning Stress to Web Cracking of Rigid Frame Bridge in Cantilever Construction D.J. Yin, X.J. He, D.Q. You and B.K. Liu	560
Investigation on Nonlinear Vibration of the Cable in Cable-Stayed Bridge in 3D Space T. Wang	564
Key Technologies Research in Incremental Launching Demolition Construction of Beijiang Bridge W.X. Lin, D.L. Xu, C. Yang, B.Y. Jia, Z.Z. He and D.Y. Chen	570
Optimal Design of Suspension Bridge Based on Minimization of Life Cycle Cost M.S. Bang	577
Research on Mechanical Behavior of Box Girder with Corrugated Steel Webs of Cable Stayed Bridge L. Lv and B. Liang	583
Research on the Wave Load Effect Based on Time History Analysis of Donghai Island Bridge W.G. Yuan and M.Y. Liu	587
Risk Prevention Measures for Three-Tower and Four-Span Suspension Bridge under Vehicle Fire M.Y. Liu, W. Tian, Y. Wang, W. Jing and X. Chen	590
Structure Calculation of Die Carrier and Determination of Pre-Camber of Main Girder of Cable Stayed Bridge H.Y. Xu, D.Y. Cui and C. He	598
Study on Nonlinear Structural Behaviors of Steel and Concrete Composite Slab S. Xu and T.Y. Xiang	602
The Key Technologies Research in Demolition Construction of Liuxi River Bridge H.Q. Wen, Z.L. Zhang, W.J. Luo, B.Y. Jia, Z.Z. He and D.Y. Chen	607
The Local Stress Analysis of Slide Beam Taking into Account the Roughness of Girder Undersurface Y.B. Wang, Z.Y. Li and R.D. Zhao	615
Bridge Pavla Wonky in Pardubice. Diagnostics of Corrosion Condition of External Cables and Use of Special Materials for Proposal of Treatment J. Kolísko, P. Huňka and S. Řeháček	619

Chapter 7: Geotechnical and Geological Engineering

A Constitutive Model with Effect of Temperature for Frozen Soil X.T. Xu, C.X. Fan and T.Y. Zhang	627
A Statistical Damage Constitutive Model for Brittle Rocks Based on the Lade-Duncan Failure Criterion Z.Y. Tian, W. Wang, X.H. Li and W.Y. Xu	632
Analysis and Study on Slope Stability of High Fill Subgrade Q. Zhang	637
Analysis of One-Dimensional Thermal Consolidation for Saturated Soil Considering Different Permeabilities C.X. Guo and R.Q. Wu	641
Analysis on the Influence of the Primary Consolidation Settlement of the e~p Curves and the Soil Bulk Density of the Soft Soil Foundation W.S. Wang and J.Q. Yu	645
Analysis the Influence of Non-Prestressed Reinforcement for Horizontal Bearing Capacity of PHC Pipe Pile P.S. Xi and X.K. Sun	649
Characteristics of Xinjiang Bad Foundation Soil J.H. Zhang	654

Discussion on Application of Empirical Formulas for Ultimate Bearing Capacity H.W. Jin and H.W. Song	660
Effects of Ice Content on Mechanical Behavior of Frozen Loess under Uniaxial Compression X.T. Xu, C.X. Fan and J.H. Yuan	666
Experimental Study and Numerical Simulation on the Large-Sized Models of Micro Anti-Slide Piles X.S. Tang, Y.R. Zheng and J.P. Xin	670
Experimental Study of Meijiang Artificial Island Fill X.C. Su, X.Y. Wang and Z. Liu	678
Ground Response of Seasonal Frozen Site under Moderate Intensity Earthquake Z.S. Chen, X.M. Yuan and S.J. Meng	682
Influence Factor on Dilatancy of Coarse-Grained Soil Based on Large-Scale Triaxial Test F.Y. Chu	687
Influence of Existing State of Pore Aqueous Solution on the Swelling Pressure of Expansive Soils Z.Q. Huang	693
Numerical Analysis of the Excavation of Deep Pit Based on Mohr-Coulomb Failure Model H.J. Sun and Y.Q. Li	697
Numerical Simulation of Unloading Zone Division for Excavated Rock Slope X.X. Wang and C.J. Deng	701
Numerical Tests on Laterally Loaded Drilled Shafts Socketed in Rock S.J. Yuan, K.Y. Zhang, Z.J. Liu and J.C. Li	706
On Atypical Affection on Environment due to Dewatering of Foundation Pit in Developed River System Area D. Li, N.F. Li, B. Tang and J.W. Gong	710
Predicts Based on Multi Modality Support Vector of the Settlement of Composite Foundation L.H. Zhang, H.B. Liu and F.P. An	716
Research of Stratigraphic Classification Based on Difficult Degree of Construction Y.Q. Duan and Y.Q. Li	723
Research on Application of Suction Bucket Foundation for Transmission Tower in River Network Area L. Qin, J.X. Zhu and S.W. Zhao	727
Research on Improved AHP Evaluation in Supporting the Right to Determine the Weight of Deep Foundation H.Y. Jiang and G.G. Yu	731
Stability Analysis of Surrounding Rock with Two Groups Parallel Joints Using DDARF Method H.P. Ma, L.G. Wang and X.W. Li	735
Stress-Strain State of Weightless Inhomogeneous Array with Cylindrical Hole V.I. Andreev	740

Chapter 7: Geotechnical and Geological Engineering

Study of Reasonable Length of Coal Seam Mining under Different Fault Dips Y.J. Zhang and T. Xu	747
Study of Reinforcement Scheme for Tunnel Heaving due to Excavation of Sunken Plaza over Subway Tunnels H. Lin, J. Yang, J.T. Chen and Q.Q. Luo	751
Study on Coal Seam Mining Face Floor Failure under Imbalance High Water Pressure C.J. Song, C. Fan and L. Song	758
Study on Effect of Excavation Depth on Internal Force of Retaining Structure of Arc Row Piles with Arc Ring Beam on the Pile Top Z.W. Zhang, R.G. Deng and Z.S. Chen	762
Study on Expansion Properties Experimental of the Different Stratification Slates in Chongqing Y.J. Zhang and C. Fan	769

Study on the Interfacial Shear Stress Distribution Characteristics of Geotechnical Prestressed Anchorage Structure S.F. Zhang, L. Zhang, L. Li and X.G. Song	773
Testing and Numerical Simulation Research on Shear Band of Soil S.W. Hou, J.H. Qu and X.L. Du	777
The Application of Stepwise-Discriminant-Analysis Oriented FCM Method in Debris Flow Classification Y.L. Shangguan, Q. Wang, J.P. Chen, L.X. He and J.Y. Yan	783
The Comparison of the Loess Mechanical Properties under Plane Strain and Conventional Triaxial Experiments L. Ma	791
The Experiment on Soil Water Characteristic Curve Considering the Effect of Urea Concentration G.Q. Dai, D.F. Tian, Y. Ruan, L. Tian and Y.L. Wang	795
The Preliminary Study on the Impact of the Velocity <i>Situ</i> Test Standard Deviation to the Response Spectra in Deep-Soft Sites Z.S. Chen, X.M. Yuan and S.J. Meng	800
The Strength Calculation Method of Foundation Treated with Sand Well Y.C. Zhang, H.Y. Hu and Z.M. Huang	805
The Study of Jinnan Loess Collapsible and Depth K.F. Yuan and J.B. Zhao	809
Study on the Prevention Measures and Causes of Cracks in Arch Crests of Galleries in High Concrete Dams P.P. Chen and G.X. Zhang	813
Analysis of the Influence of Water Content on Shanxi Loess CBR and Rebound Module X.R. Wu and L.L. Zhu	820
Study on Group Piles Effects of Offshore Engineering under Lateral Load S.J. Di, M.Y. Wang and W.B. Du	824
Model Tests on Additional Stress Transmission between Different Granular Materials in Foundation Soils C.D. Wang, S.H. Zhou and H. Su	828
Experimental Research of Matrix Suction of the Unsaturated Red Clay W.F. Zhao, L. Li and Y.H. Xiao	835

Chapter 8: Tunnel, Subway and Underground Facilities

A Scale Model Test on Hydraulic Resistance of Tunnel Elements during Floating Transportation Z.Q. Ying, L.W. Su and M.H. Lin	841
Effect Analysis on Tunnel Serviceability State by the above Expressway Extension in Loess Area K.G. Sun, C. Kong, W.G. Qiu, K. Liu, W.P. Xu and L. Gong	846
Ground Treatment and its Application in Shallow Subway Tunnel Crossing Urban River by Shield Tunneling Method X.J. Zhou	853
Key Technology for the Structure Design of Mining Metro Station in Rock Strata J. Wang	857
Mechanism Analysis of Hydraulic Cutting Outburst Prevention Measure Applied to Mining Area of Heilongjiang Province X.M. Liu, M.H. Liu, Y. Kang and J. Zhou	860
Research of Train Wind Characteristics in High-Speed Railway Tunnel R.Z. Fei, L.M. Peng, W.C. Yang and W.G. Yan	865
Research on Influence of Span on Surrounding Rock Quality of Tunnels X.J. Geng, X.W. Du and Q. Yan	869
Stress Management in Rock Drivage Team Based on Fault Tree Analysis Method R.L. Shan, S.H. Dong, B.L. Huang, F. Huang, S.J. Wu and Q.A. Wu	873
Study of the Safety Evaluation of Urban Subway Operation Based on Extenics S.M. Bai, H.S. Sun and Y.C. Zhao	878

Study on Model of Back-Filled Grouting of Shield Tunnel D.Y. Wang, D. Li and J.X. Yuan	883
Study on Structural Design and Driving Process of Subway Station Passageway Crossing Urban Trunk Road by Tunneling Method X.J. Zhou	887
Study on the Model Test of Tunnel Lining Deformation Characteristic under the Frost Heaving Force Y. Hu, Z.Y. Li and M.F. Qu	891
The Analysis of Stratum Settlement for a Large Diameter Slurry Shield Obliquely Under-Passing Embankment of the Yangtze River Z.Y. Jiang and J. Yu	895
The Operation Safety Evaluation of Xi'an Subway Y.F. He and C.X. Ji	902
Safety Assessment of Secondary Lining on the Basis of Load Structure Method and Strength Reduction Method K. Liu, G. Wang and C. Kong	907

Chapter 9: Seismic Engineering

Analysis of the Potential of Seismic Stability for the Southern Region of Tangshan Based on ArcGIS C.C. Li and X.M. Yuan	915
Dynamic Response Analysis of Soil Slope under Strong Earthquake S. Huang, H.Y. Yan, D.G. Cai and B. Song	921
Experimental and Numerical Study of Enhancing the Seismic Behavior of Rammed Earth Buildings K. Liu, Y.A. Wang and M. Wang	925
Finite Element Analysis on Low Cycle Fatigue Properties of HRBF RC Pile Tip Q. Fu, S.T. Liang and X.J. Zhu	932
Research on the Reparability of Structures Based on Post-Earthquake Residual Deformation J.B. Hao and G. Wu	938
Seismic Performance Evaluation of Residential Structures in Egypt Y.E. Ibrahim, O. Shallan, A. Elshihy and M. Selim	945
Seismic Performance of T-Shaped CFT Column to Steel Frame Beam Connection – Experimental Study Y.T. Li, C.X. Xu and G.F. Du	951
Shaking Table Test of Underground Pipeline under Three Dimension Seismic Excitation – Numerical Simulation X. Fu, J.W. Bi, Z.J. Wang and C.W. Yang	960
Study on Corrugated Steel Web Bridge Seismic Isolation Technology in High Intensity Seismic Region H.X. Li and Y.M. Zhao	965
Study on Resilience Model of High-Strength Concrete Frame Columns G.J. Zhang, X.L. Lu and B.Q. Liu	969
The Improvement Ways to Equivalent Linearization Method Based on the Difference between Results of Two Programs in Moderate Weak Site X.B. Yu, R. Sun and S.J. Meng	973
The Research Status of Wheel-Rail Interaction Study under the Seismic Load Condition Z.J. Wu, Z.J. Wang and J.W. Bi	977
The Seismic Performance Analysis for the Ceramsite Concrete Frame – Shear Wall Structure J.X. Chen, Y.W. Liu, J.R. Yang and X.X. Hou	981
The Stiffness Change and Dynamic Characteristics of the RC Frame Weak Layer under Strong Earthquakes H.H. Jia and D.M. Wei	989
Verification of the Applicability of Seismic Safety Evaluation Program LSSRLI-1 in Stiff and Half-Stiff Sites Using Exact Solution R.S. Li and X.M. Yuan	994

Nonlinear Seismic Responses Analysis of Jinwan Square No.9 Building L. Qi, Z.W. Huang and X.Y. Hu	999
Finite Element Analysis on Seismic Behavior of Steel Frame-Steel Reinforced Concrete Lateral Resistance Wall Structure Y. Guan, P.S. Liu and S.N. Song	1003
Research of Seismic Design Method of RC Frame Structure Retrofitted by FRP D.Z. Yang, Y.P. Peng and Q. Xie	1007
Seismic Reinforcement Application of Buckling-Restrained Braces in the Bottom Frame-Shear Wall Structure P.S. Liu and L. Bai	1012
The Finite Element Analysis on Seismic Performance of Ring Beam and Constructional Column with Different Storey in Masonry Building X.Y. Xiong, R.J. Xue, S. Zhang and L.J. Wang	1016
Damage Assessment of Historic Buildings Hit by Earthquake G. Boscato and A. dal Cin	1020
A Method of Optimum Installation of the Viscoelastic Damper on the Steel Frame Structure L.M. Li, C.W. Huang, C. Shen and Y. Tian	1027
Study on the Comparison of Ground Response Analysis for Class I Site X.F. Li and R. Sun	1031
Considering Seismic Acceleration Distribution Coefficient of Highway Roadbed Stability Study X.C. Su, Z. Liu and X.Y. Wang	1035
Research on Seismic Displacement Response of Cable Stayed Bridge without Back Stays L. Lv, B. Liang and W.S. Wang	1039
Comparative Study on Seismic Design Method of High-Piled Wharf of Different Depth in China and Japan B. Song, H.L. Wang and S.J. Liu	1043
Reliability of Pile Foundation of Offshore Jacket Platforms Subjected to Seismic Action Z.W. Shen, X.H. Wang and W.L. Jin	1047

Chapter 10: Roads, Railway Engineering and Traffic Engineering

A Column Generation Algorithm for High-Speed Railway Seat Inventory Control Y. Huang, H. Song and L.X. Tian	1055
Aeronautical Study for Flight Time Estimation Applying Artificial Neural Network and Genetic Algorithm Y.C. Lin, L.K. Lin and S.H. Tsai	1063
Analysis on Coal Transportation Network Invulnerability Based on Edge Failure L.N. Sun, H.S. Sun and Y.L. Zhao	1075
Analysis on the Impact of the Type and Content of SBS on the Performance of the Modified Asphalt Mixture S. Han, D.Y. Niu, Y.M. Liu, D. Chen and D.W. Liu	1079
Analysis on the Main Factors Influencing the High-Speed Railway Passenger Flow Y. Huang, H. Song and C.Y. Jia	1085
Applied Research of the Relational Matrix Analysis in the Road Traffic Safety Measures Decisions Z.Y. Li	1091
Durability Test Research of Asphalt Mixture with Rubber Particles under the Condition of Freeze-Thaw Cycle H.Y. Xu, S.Y. Dang and D.Y. Cui	1096
Establish of the Mutual Relation of Resilient Modulus and CBR in Loess Region of Shanxi Province X.R. Wu and L.L. Zhu	1100
Experiment of Slurry Shield Tunnel Recycling Waste Sand in Sand-Pebble Layer C.R. Pang and X. Wen	1104
Experimental Study on Foamed Asphalt Warm Mix Technology Y.B. Wu, J.J. Shi, C.F. Yang and S.X. Song	1110

Influence of Large Track Maintenance Machine on Sleeper Supporting Stiffness M.N. Zhang, Y.B. Wu, X.C. Ma and P. Wang	1115
Maximum Shearing Stress Analysis of Asphalt Pavement Structure J.H. Gao	1120
Numerical Study Porosity of Railway Ballast during Tamping Process T.Y. Zhou, B. Hu, X.Y. Zhao and B. Yan	1124
Optimization of Coal Transportation Network Robust Control J.S. Qiao, X.F. Wang, X.S. Shen and L. Shi	1128
Railway Maintenance Analysis Based on Big Data and Condition Classification B.Y. Song, Y. Zhong, R.K. Liu and F.T. Wang	1134
Research on the Information Management of Maintenance-of-Way Infrastructure X.C. Pan, R.K. Liu and F.T. Wang	1139
Review of Applied Study for Red Clay in Highway Subgrades J.X. Ding and Y.W. Meng	1144
Sliding Mechanism Analysis and Treatment for Rock Pile Subgrade in GuiZhou Province J.J. Zheng, L.J. Wu and R.H. Guo	1150
Study Behavior of Railway Ballast under Cyclic Loading T.Y. Zhou, B. Hu and B. Hua	1155
Study on the Relations of Strength Control Indicators of Road Subgrade in Shanxi Loess Region X.R. Wu and L.L. Zhu	1160
Vibration Analysis of Simply Supported Beams Traversed by Uniformly Distributed Two-Layer Spring-Mass System Y. Yang, Y. Wang and Y.F. Yang	1164
Effect of Micron Fly Ash and Nano Calcium Carbonate on Properties of Styrene-Butadiene-Styrene Copolymer Modified Asphalt D.J. Zhou and N.F. Han	1169
Study on the Anti-Cracking of GFRP Bars Asphalt Concrete Bridge Deck Pavement under the Vehicle Load X.X. Feng, X.J. He and Z.H. Yang	1173
The Application of High Content SBS Modified Asphalt Waterproof Layer in the Project of Jing-Jin-Tang Highway's Bridge Deck Maintenance H.F. Zhang, L.Y. Wei and N. An	1178
The Effect Analysis of the Thin-Walled Tubular Pile Technology Used in the Foundation Treatment of the High-Filling Railway Freight Yard J. Yu, T.Y. Chu and Q.M. Gong	1184
Applied Research of the Composite Antiager in Asphalt L. Zou and N.X. Zheng	1191
The Practice of Aluminum Plate Material in Modern Traffic Architecture H. Li, Z.Y. Feng, Y.J. Li, Y. Xiao and M. Zheng	1195

Chapter 11: Hydrology, Coastal and Hydraulic Engineering

A Stochastic Collocation Method for Simulating Groundwater Recharge Y.Q. Tang, L.S. Shi and J.Z. Yang	1201
Analysis of the DO Distribution and the Influencing Factors at the Downstream of Large Dam F.Q. Kong, Y. Wang and Y. Cheng	1206
Analysis on Mechanism of Coupling Fields of Seepage and Stress and its Modeling F.H. Wang, G.X. Yan and D.J. Zhao	1211
Analysis on the Stress of Arch Dam Heel C.T. Wang, H. Lv and Y.P. Wu	1216
Application of Tensile Stress Diagram in Calculating Reinforcement of Surge Tank P.X. Wang	1222
Application Study Based on Surfer Underwater Earthwork Calculation X.F. Chen and X. Shi	1226
Cascade Reservoirs Optimal Scheduling Method Based on Chaotic Ant Colony Algorithm Z.H. Zhu and H.M. Gao	1230

Modal Analysis on the Coupled Fluid-Structure Interaction of High Arch Dam C.T. Wang and Y.P. Wu	1234
Numerical Simulation of Seepage Field of Tailing Water Channel in Construction Period of Coupling Fields of Stress and Seepage G.X. Yan, W. Wu and D.J. Zhao	1240
Research Progress of Protected Plunge Pool of High Arch Dam Y.K. Wang and R.Q. Liao	1244
Study on Jiping Canal Water Line of South-to-North Water Transfer Project X.C. Su, Z. Liu and X.Y. Wang	1248
The Effect of Coal Mining on the Multi-Aquifer System J.Q. Lei, X.Q. Zheng and H.F. Zang	1252
Theoretical Application of Ensemble Kalman Filter to Adsorptive Solute Cr(VI) Transfer from Soil into Surface Runoff C.Q. Tan, J.X. Tong, B.X. Hu and J.Z. Yang	1257
Vortex-Induced Dynamic Response of Submerged Floating Tunnel Tether Based on Wake Oscillator Model Z.B. Su and S.N. Sun	1262
Construction of Evaluation Index System of Key Groundwater Levels of Typical Irrigation Area in Heilongjiang Province Y.H. Shang, C.L. Dai, P. Qi and J.S. Xing	1266

Chapter 12: Computational Mechanics and Mathematical Modeling

A Beam Element for Geometric Nonlinear Dynamical Analysis J. Duan and Y.G. Li	1273
A Quantum Mechanics Study on the Electronic Structure of Impurity-Bearing Sphalerite (ZnS) Y. Chen, J.H. Chen and Z.W. Wei	1282
An Algorithm for Computing Logarithms of R-Sum of First and Last Circulant Matrices Y. Mei	1286
Downhole Drilling Mechanics Analysis Based on Closed-Loop Rotary Steerable Drilling System Y.X. Yang, Y.P. Du and R.S. Wang	1290
Iterative and Non-Iterative Solution of Planar Resection H.E. Zeng	1295
Mixed Finite Element for Geometrically Nonlinear Orthotropic Shallow Shells of Revolution L.U. Stupishin and K.E. Nikitin	1299
Numerical Analysis of Effect of Restraint on the Fire Resistance of Concrete Structures R.T. Li	1303
Numerical Simulation for the Effects of Ice Thickness on the Overhead Transmission Cable Tension Z. Wang, J. Yao and S. Peng	1307
Numerical Simulation of Non-Contoured Aerial Cable Tension Z. Wang, J. Yao and S. Peng	1312
Some New Results on k-Circulant Matrices Y. Mei	1317
Studying a Sort of Special Circumstance of Variance Estimation of Unit Weight Y.H. Deng	1321
The Absolute Torsion of Circular Shaft and Neutral Cross-Section Q. Luo and L.B. Qin	1325
The Calculation of the Dynamic Problem for the Beam with Arbitrary Boundary Condition by Method of Convolution-Type Point Collocation Y.L. Li, Z.G. Zhao and H. Yang	1330
The Compilation of Nonlinear Analysis Program for Externally Prestressed Concrete Beams H.J. Cai, J.M. Zhou and Y. Gao	1334

The Study of Compactly Supported Orthogonal Two-Direction Vector-Valued Wavelet Packet	
L. Li	1340
An Improved Method of Determining the Disturbed State Concept Model Parameters	
W. Lu and J.J. Pan	1345
Numerical Simulation of Air Distribution and Particle Movement in a Displacement Ventilated Room	
Z.B. Wang, B.Q. Wang, R.H. Chen and S. Yao	1350
Influence Factors of High dam Reservoir Basin Deformation Based on Finite Element Analysis and Weights Analysis	
H. Gu, X.F. Huang and J. Ding	1354
Evaluation on Aerodynamic Across-Wind Response for a Tall Building Using Tuned Liquid Column Damper	
J.Y. You, K.P. You and Y.M. Kim	1361
Study General Peak-Pressure Formula on Flat-Structure Slamming into Water	
L.F. Yu, Y.Q. Zhang and L.S. Zhu	1371
Crack Calculation of Beams Reinforced with FRP Bars Based on Linear Bond-Slip Model	
X.D. Li, H.C. Feng and W.N. Yuan	1377
Design Method for the Normal Section of Carbon Textile Reinforced Concrete Beam	
L. Chen	1381
Numerical Simulation Method of Tensile Behavior of Glass Fiber Laminates	
S.C. Yang and J.H. Zhang	1386
A Study on the Non-Gaussian Property by the Method of Limiting Streamline	
X.F. Sun	1390
Research on the Calculation Method for Bending Rigidity of Recycled Concrete Beams	
B. Lei, H. Wu, Y.S. Yan and C.H. Rao	1396

Chapter 13: Construction Technology

Construction Control Technology of Cable Hoisting System for the Arch Rib of Steel Box Bridge	
Y. Wang, Y.H. Wei and G.F. Hu	1403
Construction Technology for Ultra-High Baseboard and Hopper of Silo	
Z.F. Zhu, Q.Z. Qu, J. Dong and H.F. Ding	1407
Construction Technology of one Unsymmetrical Loaded Deep Foundation Pit Adjacent to Expressway Subgrade	
B. Liu and P.S. Xi	1411
Design of Retaining and Protecting for a Deep Foundation Excavation	
H.W. Jin	1416
Study on Mass Concrete Construction Technology of Raft Foundation in Yantai Ocean Development Center	
J. Zhu, Y.B. Zhang, X.F. Du and Y. Jiang	1421

Chapter 14: Project Management and Engineering Management

Analyzing the Cost of High-Rise Buildings after Second Design Based on the Bill of Quantity Valuation Mode	
A.X. Wei and J.H. Yao	1429
Construction Project Cost Information Management Research	
Z. Wen	1433
Cost/Schedule Monitoring and Forecasting for Project Based on Earned Value Management (EVM)	
J.W. Huang, H.M. Pan, Y. Li, Y.T. Zhu and Z.Y. Liao	1437
Creative Industry Policies and International Comparison in Engineering Design Field	
W.L. Zhao and H.T. Cao	1441
Economic Life Prediction of Concrete Structure	
B. Manganeli	1447

Evaluation on the Development of Shanghai Suburban Infrastructure Based on AHP-Entropy Method	
Q.S. Xu, J.G. Shi and Y.G. Zhang	1451
Highway Project Investment Risk Factors and its Mechanism: Empirical Studies Based on Structural Equation Model	
W.Z. Zhao, L.L. Mu and N. An	1457
Matrix Method Application on the Civil Engineering Project Management	
H. Chang	1462
New Ideas to Resolve Construction GFA Specification	
H.P. Yang	1466
Research on Construction Engineering Quality Supervision Based on Artificial Neural Network	
G.B. Han and L.N. Zhang	1471
Research on Construction Safety Management of High-Rise Buildings Based on the Grey Hierarchy Evaluation Model	
H.W. Tian	1477
Research on Cost Control of Infrastructure Project with Prior Operation Function in Design Phase	
H. Ke, S.F. Gan and X.N. Liu	1482

Chapter 14: Project Management and Engineering Management

Research on Important Process of Project Monitoring and Control	
X.G. Li and L.X. Wang	1489
The Evaluation Model of Bridge Construction Safety Management Variable Fuzzy Sets	
J. Yang and S.L. Chen	1494
The Performance Evaluation of Construction Safety Supervision Based on Evidence Theory	
H.J. Wu	1499
The Research on Railway Construction Project Materials Supplier Selection Model	
A.M. Li, G.Q. Wang and J.J. Zhang	1503
Methods of Creation Basis Decisions of Management System Construction Waste Recycling	
P.P. Oleinik and L.S. Grigorieva	1509

Chapter 15: Architectural Design and its Theory

Analysis of Ancient Chinese Architecture Aesthetics	
Y. Zhang	1515
Analysis of China Ancient and Modern Sports Architecture	
X.J. Chen	1519
Analysis of Sports Architecture Technical Philosophy Characteristics	
X.J. Chen	1523
Application of Jiangxi Ancient Buildings Carved Window Shape in the Contemporary Design	
J.G. Yao and L. Wu	1527
Applied Research and Development Uygur Architectural Brick Mill Mosaic and Information Technology	
G. Li	1531
Study of Structural Morphological Design during the Stage of Architecture Composition	
W.Q. Xu, Q.R. Guo and H.J. Tong	1537
The Dominant Expression of the Qinling Mountains's Regional Culture in Residential Buildings' Regional Style	
Z.T. Xiao	1541
The Humane Care Implied in Chinese Architectural Aesthetics	
X. Liu	1545
The Relation between Sports Building and City Image	
X.J. Chen	1549

Sports Architecture Structure Stress Characteristics Analysis X.J. Chen	1553
---	------

Chapter 16: Urban Planning and Design

Naturalization Design of Urban Water Landscape Y.F. Ding, D.S. Tang, Y.H. Wei and Y.X. Sun	1559
Study on Correlation between Housing Construction and Influence of Urban Development in the Succession of Urban Dynamics M. Li	1563
Sustainable Urban Revitalization in Historic Districts: A Case Study of Huilongwo Area in Xuzhou Q. Liu and B.T. Liu	1567
Talking about the Residential Outdoor Environment Design in the Context of the Aging W.Y. Gong, D.L. He and B. Bai	1573
The Land Utilization Countermeasures on the Old Town of South Jiangsu in the Context of New-Type Urbanization – Take the Old Town, Jinjiaba, Wujiang, Suzhou as an Example W.Q. Fan, Z.Y. Chen and Y.Z. Huang	1577
The Use of the Investment Potential for Planning Sustainable Cities L.U. Stupishin and M. Maria	1582
Urban Bluebelt Construction – Control Countermeasure of Urban Blue Line (River Project) from Line to the Whole Y.Z. Huang and L. Lin	1586
Urban Contexts and the Shape of Urban Features G. Li	1591
Urban Form Conservation Strategies for Sustainable Development: An Urban Design Project of a Historic Town Y.P. Hu	1595
Integrated Civil Monitoring System Based on POSA H. Zhang, M. Liu and D.J. Hu	1599
Contradictions and Countermeasures of Affordable Housing Construction L. Yan, W.R. Zhou and J.F. Miao	1603
Study on Natural Ventilation Potential for Residential Buildings in Southern China Y. Liu	1610
The Fusion of Commercial Buildings and the City W.D. Tan and L. Zhu	1618
Study on the Selection Pipelines into the Comprehensive Pipeline Trench in Urban Rail Transit Construction Y. Bai, P.B. Cui, Q. Zhang and L. Wu	1622
Commercial Space Design Research – Take Jincheng as an Example N. Li and Y.P. Liu	1626
The Application of Mathematical Statistics in Urban Geography Research X.F. Ma	1630
Public Art and Contemporary Urban Culture – Research of Embodiment of Core Value of Urban Public Art in the Construction of Urban Culture Z.G. Li and J. Sun	1634

Chapter 17: Landscape Planning and Design

A Study on Sustainable Green Ecological Landscape Design Y.J. Liu	1641
Analysis on Historic Landscape Space Configurations and Evolutions of Qijiang Ancient Town Y. Li	1645
Discussing of Creating a Nostalgic Atmosphere in Landscape Planning and Design Y.T. Zhou and H.M. Liu	1649

Landscape Design of Residential Environment in City H.M. Cui	1655
NDVI Changes of the Nansi Lake in Shandong Province of China C.L. Liang	1659
On the Change of Expression Concept of Chinese Characters in Landscape Design Z.L. Dong	1663
A Study on the Effect of Wind Fences in Reducing Wind Velocity at Fruit Farms J.Y. You, K.P. You, S.Y. Paek and Y.M. Kim	1667

Chapter 18: Architectural Environment, Eco-Building and Green Building

Numerical Study of Thermal Comfort with the Effects of Canopy Transparency C.W. Kwon and S.W. Shin	1677
The Reflection and Expectation on Green Architecture L. Pan, Y.H. Liao and B. Wang	1681
A Research on the Design Strategy Suitable for Local Green Building Design in China – A Comparative and Empirical Study on GBES and LEED-NC2009 H. Zhang	1685
Ecological Housing Design Strategies for Hot-Humid Climate in Sichuan Basin K.C. Nie	1690
Let the Historic District Shine Again J.D. Jia and B. Wang	1693

Chapter 19: Building Energy Saving Technology

A Study on the Energy Consumption of Zhejiang New Rural Residential Buildings Based on LCA Theory G.X. Wang, K.Y. Xu, J.H. Zhang, J.H. Yao and H.F. Shen	1699
Energy Efficiency Renovation Study of a University Library Building in Ningbo S. Cang	1703
Measurements of the Initial Ground Temperature in GSHP System Y.S. Zhou, W.L. Ju and Z. Liu	1707
Principal Component Analysis in Building Energy Efficiency Rating System for Apartment Housings H.G. Jung, M.C. Park and S.W. Shin	1716
Rainwater Collection and Purification Heating Roof System S.L. Gu	1721
Research Progress of Composite Thermal Insulation Wall in Hot Summer and Cold Winter Zone of China H.M. Liu, C.Q. Wu, Y.B. Xu and A.D. Zhu	1725
The Analysis of Adjustment Modes of District Heating System S.L. Wang, X.L. Yang and J.J. Chen	1730
The Economic Performance of Ground-Source Heat Pumps P. Gong and J. Tang	1735
The Energy-Saving Management System Design of Major Projects in Implementation W. Li, M.Y. Ma and H.T. Zhang	1739
The Numerical Simulation and Research and Application of Energy-Saving Effect of Hot Air Curtain Jet Velocity of the Dining Room K.R. Ma and X. Wang	1744

Chapter 20: Construction Materials Research

Comparison and Selection of the Durability Evaluating Parameters of Concrete in Saline Soil Region L. Zhang and X.P. Su	1751
---	------

Constitutive Relations of Masonry under Compression — A State-of-the-Art Review X.Y. Xiong, S. Zhang, L.J. Wang and R.J. Xue	1755
Corrosion-Induced Concrete Cracking, Steel-Concrete Bond Loss, and Mechanical Degradation of Steel Bars F.J. Tang, G.D. Chen and W.J. Yi	1760
Durable Carbon for Structure Applications, H₂-Energy Carbon Building Materials (HECBM) W.C.J. Wei and J.W. Halloran	1771
Effect of Mineral Admixture on Mechanical Property of PHC Pile Concrete L.L. Xue and Y. Shen	1775
Effects of Different Lithium Admixtures on Ordinary Portland Cement Paste Properties Y.H. Deng, C.Q. Zhang, H.Q. Shao, H. Wu and N.Q. Xie	1780
Experiment on the Mechanical Performance of Fiber Lightweight Aggregate Concrete after Freeze-Thaw and Elevated Temperature B. Cheng, J. Huang, W.T. Jiang and J.M. Wang	1790
Experimental Investigation of Stiffened Square CFST Columns under Axial Load X.Z. Zheng and X.H. Zheng	1794
Experimental Research on Compressive Strength of Pumice Concrete and Volcanic Concrete Wall L.J. Dou, M. Zhang and M.Y. Xu	1801
Experimental Study on Performance of Steel and Composite Plate Combined Column F. Wu, X.Y. Zheng and J.W. Ding	1805
Experimental Study on Seismic Behavior of Double-Wall Precast Concrete Shear Wall Q.D. Xiao and Z.X. Guo	1812
Influence of Laboratory Accelerated Carbonation on the Properties of Recycled Concrete Aggregates Z.F. Zhao, P.F. Jin and Q.Q. Zhao	1817
Meso-Structure and Transport Performance of Near-Surface Concrete L.P. Wu and J.B. Yang	1821
Preparation of C80~C100 High Performance Concrete and the Ultrahigh Pumping Technology L.B. Xu, N.Q. Feng, I. Zakaria and B.X. Wu	1830
Process Technology Silica Sand into Microsilica and Nanosilica for Construction Material A.R.I. Tjahjani, Jonbi, R. Mastra and E. Mulyani	1836
Research on the Comprehensive Utilization of CPFL in Concrete Moisture Curing J.F. Chen, S.P. Li, L. Wang and H. Dong	1839
Study on Chloride Ion Permeability Resistance Variation of C40 Concrete Z.D. Huang	1845
Study on the Durability of Normal Strength Concrete under the Action of Salt Corrosion and Dry-Wet Cycles X.P. Su and J.H. Guo	1849
The Analysis of Punching Shear Strength for Concrete Slabs Based on the Unified Strength Theory J.H. Han and D.B. Wang	1853
The Influence of GGBS on the Shrinkage Performance of Concrete Y. Liu and D.X. Ma	1860
The Research of GGBS' Influence on the Cracking Resistance of Concrete Y. Liu and D.X. Ma	1864
The Use of Infrared Thermography in the Analysis of Engineered Cementitious Composites R. do Bom Conselho Sales, S. Andere Pedra, M.T.P. Aguilar, F.A. Sales and P.R. Cetlin	1868
Intensity Errors and Origins of Catalyzed Concrete H.S. Yang, X.P. Wang, Y.L. Yang, Y.J. Pu, X.L. Peng, H. Fan and B.Y. Wang	1876
Crack Self-Healing Properties of Concrete with Adhesive Q.Y. Cao, T.Y. Hao and B. Su	1880
Creep Behavior of High-Performance Concrete X.Y. Xiong, L.J. Wang, R.J. Xue and S. Zhang	1885
Destructive and Nondestructive Testing on Silica Fume Concrete Y.E. Ibrahim, N. Al-Akhras and W. Al-Kutti	1890

Different Gradations Cement Improved Phyllite Test Analysis Y.Q. Chen, H.J. Zhang and T.Q. Wang	1894
Effect of Emulsified Waste Oil on Micro-Structure and Autogenous Shrinkage of the High Strength Concrete C.G. Han, M.C. Han, J.G. Huang and T.C. Kim	1899
Effect of Polypropylene Fiber on the Properties of Cement Mortar J. Pan, F. Li and X.W. Zhang	1903
Effect of Rubber Powder Dosage on Performance of Cement Concrete Y.C. Zhang, S.W. Liu and L.L. Gao	1908
Experimental Research on the Freeze-Thaw Resistance of Basalt Fiber Reinforced Concrete X.C. Fan, D. Wu and H. Chen	1912
Experimental Study on Proportion of Tensile Strength and Compressive Strength of the Crumb Rubber Concrete Modified by Latex W. Li, Z. Huang, X.C. Wang and Z.S. Zang	1916
Experimental Study on the Mechanical Properties of the Crumb Rubber Concrete Modified by Silane Coupling Agent W. Li, Z. Huang, X.C. Wang and Z.S. Zang	1920
Improving the Impact Resistance of Reinforced Concrete H. Abbas, T. Almusallam and Y. Al-Salloum	1924
Influence of PP Fibers on the Relative Residual Splitting Tensile Strength of HSC after Exposure to High Temperatures R.Z. Yan, W.H. Ge and H.X. Du	1930
Influences of Mineral Admixture on Properties of Porous Pervious Concrete Made of Recycled Aggregates P. Gong and Y. Zhou	1934
Nuclear Magnetic Resonance Analysis of Air Entraining Natural Pumice Concrete Freeze-Thaw Damage X.X. Wang, X.D. Shen, H.L. Wang and H.X. Zhao	1939
Orthogonal Experiment Studies on Mix Design of SFRHSC D.Q. He and J.G. Wang	1944
RCM Method Practicability Study of Concrete Chloride Ion Permeability Resistance Z.D. Huang	1948
Research on Reinforcing Methods of Continuous Steel-Concrete Composite Beams with Web Openings L.Q. Li, D.H. Zhou and W.Y. Liao	1952
Selection Research of Excitation Agent for Renewable Brick Powder Foam Concrete S.F. Dong, W.J. Long and X. Liu	1958
The Development and Application of Foam Concrete Y. Xia	1962
The Effect of Admixtures on Anti-Permeability of C30 Anchor Anti-Seepage Mass Concrete W.R. Huang and M. Tan	1967
The Impact of Steel Fiber on the Performance of Lytag Lightweight Aggregate Concrete M.Y. Hang, C.X. Sun and P.Y. Zhang	1974
Feasibility of Biomass Ash (Cattle Manure Ash) Replacing Some Cement in Concrete to Reduce Carbon Dioxide Emission X.Z. Tian and S.G. Zhou	1979
Experimental Study on Dynamic Mechanical Properties of HPP Hybrid Fibers Reinforced Lightweight Aggregate Concrete D. Wang, Z.K. Guo, F. Shao and W.X. Chen	1983
Mix Proportion and Mechanical Properties of Recycled PET-Brick Powder Mixture F.B. Meng, Y.Z. Hu and H.Y. Yue	1990
Preparation and Performance of Diatomite Latex Paint for Interior Wall L.Y. Wang, X.F. Xiao and G.Q. Gai	1994
Recent Research of Shape Memory Alloy in Seismic Resistance X.L. Song, C.W. Huang and D. Wang	1998
Research on the Performance of Silt Sintered Insulating Brick and Key Molding Equipment H.M. Liu, Y.B. Xu, C.Q. Wu, A.D. Zhu and J.Q. Zuo	2002

Limestone and Dolomite Tailings Properties and Bricks Development
J.M. Mao 2007

Chapter 21: Materials Science

- A New POM-Based Supramolecular Compound: Synthesis, Structure and Adsorptive Property of [Cu(phen)₂]₃[W₆O₁₉]**
Y.B. Liu, H.J. Wang and H.K. Zhao 2013
- Adsorption Mechanism of Rectorite Modified by Lithium**
Y.A. Ming, Y.R. Wang, Z. Liu and F.R. Zhou 2017
- Antioxidant Activity and Chemical Constituents of Microalgae Oil of *Schizochytrium aggregatum***
J.W. Lv, X.Q. Yang and L.H. Li 2022
- Collection of Submicron Particles by Polyethylene Composite Materials Collector**
J.C. Chang, A.P. Tao, M.F. Gao, C.Y. Xu and C.Y. Ma 2030
- Comprehensive Evaluation on Effects of Strengthened by Bonding Steel Plate or CFRP Based on Analytic Hierarchy Process**
D.J. Mao and F.C. Liu 2037
- Cracking in Brittle Material at Presence of a Dislocation**
H. Hamli Benzahar and M. Chabaat 2043
- Current Research and Development of Silica Aerogel Drying Method**
M.Y. Xu, D.J. Tan, Y. Wang, P.Q. Wang, L. He and J. Yang 2048
- Effect of Tb³⁺-Coped Concentration on Properties of Li₂SrSiO₄:Tb³⁺ Phosphor**
P. You 2052
- Experimental Analysis of Minimum Ignition Temperature of Dust Cloud Obtained from Thermally Modified Spruce Wood**
J. Zigo, P. Rantuch and K. Balog 2057
- Influence of Fiber Embedded Length on Properties of Single Fiber Pull-Out Test**
Y.F. Zhang, P.R. Chen, H. Liu and Q.H. Wu 2061
- Investigation on Basic Properties of Rice Husk Ash – Blast Furnace Slag Composite Binder**
J. Zha, J.H. Li, Y.P. Jiao and S.H. Zhou 2071
- Materials Properties and Material Applications in a New Wood Flute back Combination Design and Research**
Y. Liu and Z.J. Li 2076
- Preparation and Characterization of Hyperbranched Polymer**
D.J. Zhou and N.F. Han 2080
- Preparation of Eu(BA)₃phen/PVP Fluorescent Nanofibers by Electrospinning**
L.Y. Wang, G.Q. Gai and X.T. Dong 2084
- Project for Improving Dark Color Fastness of Polyester or Spandex**
X.P. Zeng and J.F. Liu 2088
- Research on Polycarboxylic Superplasticizer with Slump Retaining**
G.S. Liao, T. Ai and Y. Xiao 2092
- Study on Vinyl Ester Based Structural Anchor Adhesive for Fast, Low Temperature Cures**
B.W. Zhu, A. Lin and F.X. Gan 2099
- Synthesize Biodiesel through SO₄²⁻/ZrO₂ for Use as Solid Super Acid Catalyst in Biodiesel Production**
Y.H. Gao 2105
- Ultrasonic Synthesis of Ag₂Se Nanocrystal in Perrhenate Solution**
W.J. Shan, Q. Yan, D. Li, D.W. Fang and S.L. Zang 2109

Chapter 22: Data and Signal Processing

- A Keyword Query Method Based on Digital Type Properties**
J. Zhao and H.Y. Xiong 2115
- A Method of Drawing Contour Basing on Membrane Analogy Method**
G. Min and H.K. Chen 2119

Design of Micro Inertial Navigation Computer and Data Real-Time Displaying System Based on FPGA	
N. Chen	2123
Modeling and Simulation of Ship Motion for Dynamic Positioning Vessel	
P.W. Yu and H. Chen	2127
The Initial Retrieval Based on Image Segmentation	
Q.H. Zhan	2131
The Teaching Practice of Consolidation Experiment Based on the Data Acquisition System	
Y.L. Zhao	2135

Chapter 23: Environmental Engineering and Wastewater Treatment

Intensifying the Processes of Wastewater Purification from Phosphates and Organic Impurities	
O.A. Ruzhitskaya and E.S. Gogina	2141
Investigation of the Processes of Nitrification and Denitrification in Wastewater Treatment	
E.S. Gogina, O.A. Ruzhitskaya and O.V. Yantsen	2145
Microwave-Ferrous Sulfate Modified Activated Carbon Adsorption Study on Phosphorus Removal	
Y.F. Li and C.F. Wei	2149
Removal of Phosphates from Wastewater and Intensify the Biological Wastewater Treatment Process from Organic Pollution	
O.A. Ruzhitskaya and E.S. Gogina	2153
The Influence Factors of Phenol Wastewater by Complex Three-Dimensional Electrode Polarity Treatment	
Y.F. Li, Y. Gao and J.J. Liu	2157
Research on the Eco-Cluster and Low-Carbon Technology Innovation of Biomedicine Industry in China	
S.R. Yan	2161
Hydrothermal Synthesis and Characterization of POM-Based Photocatalyst for Degradation of Pollutant Organic Dyes	
Y.B. Liu, H.J. Wang and H.K. Zhao	2166
Study on Dynamics of Eco-Tourism System	
Y.M. Liu, Y.D. Dong and J. Wu	2170
Study on Soil Microbial Characteristics of <i>Elsholtzia harchowensis</i> in Copper Mine	
S.Y. Xiong, J.K. Huangfu, S.W. Wang and M.Q. Qiu	2174
Three Vertical Flow Constructed Wetlands Filled with Different Packing Materials for Piggery Wastewater Treatment	
S.Y. Xiong, J.N. Ge, S.W. Wang and M.Q. Qiu	2178

Chapter 24: Engineering Education

Application of Progressive Teaching Model in Engineering Hydrology and Hydrologic Calculation	
X. Meng, W.Q. Cheng and X.B. Wu	2185
System Analysis of the Distance Education Examination System	
H. He, H.C. Han and H. Li	2189
Teaching Innovation and Exploration of Principles and Applications of Transducer Course Based on CDIO Idea	
R.Q. Chen	2193

CHAPTER 1:
Structural Engineering

A nonlinear model for Beam-Column Joint Based on OpenSees

Yanzhong JU^{1, a}, Yu MU^{1, b} and Dehong Wang^{1, c}

¹ Department of Civil Engineering, Northeast Dianli University, Jilin, China

^ajuyanzhong@126.com, ^bmuyu003@gmail.com, ^chitwdh@126.com

Keywords: Beam-column Joint, OpenSees, Constitutive Model, Hysteretic Curve

Abstract. The beam-column joint is the key component of a RC structure and also the hub of stress transferring between beam and column. It is the major part for ensuring enough stiffness, ductility and good energy dissipation capacity of the RC frame. In order to simulate the beam-column joints under cyclic loading, a model based on OpenSees was studied. OpenSees has advantages over other nonlinear analysis software in the improvement of algorithms. Comparison of simulated and observed hysteretic curve indicates that the proposed model is appropriate.

Deformation and failure of beam-column joint

Fig. 1 shows an idealized force distribution at the surrounding of a typical joint under earthquake loading of the building frames. Beam and column moments are assumed to transfer into the joint through tension force resultants carried by the frame-member longitudinal reinforcing steel (white arrows in Fig. 1) and compression force resultants carried by frame-member concrete (dark grey arrows in Fig. 1). Shear forces are assumed to transfer into the joint through concrete in the vicinity of the frame-member flexural compression zones (hatched arrows in Fig. 1). Fig. 2 shows an idealization of the loads acting on the joint core. Compression and shear forces are assumed to act directly on the perimeter of the joint core (dark grey and hatched arrows in Fig. 2), while tension forces carried in frame-member reinforcing steel are assumed to transfer into the joint core through distributed bond forces (light grey arrows in Fig.2). [1]

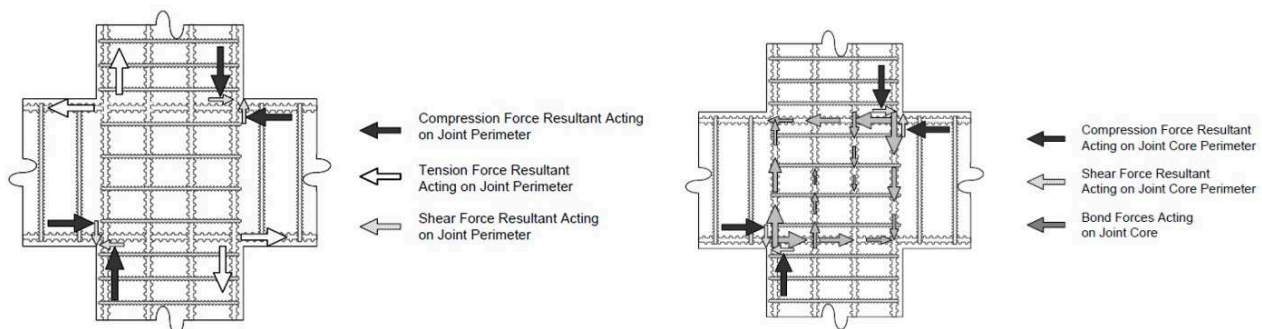


Fig. 1 Load Distribution at the Perimeter of the Joint **Fig. 2** Loading of the Joint Core

BeamColumnJoint Model and Constitutive Model

OpenSees is widely used nonlinear analysis software based on C++ program, upon which statistics analysis, pull-over analysis and dynamic analysis can be achieved. It is sponsored by the National Science Foundation (NSF), under the leading of Pacific Earthquake Engineering Research Center (PEER), developed by UC Berkely and other American Universities.

A super BeamColumnJoint was proposed by Laura N. Lowes [2], by reducing the degrees of freedom of the interface between joint core and beam or column parts. Due to accuracy and efficiency, it has been adopted by the OpenSees Element Labrary.

OpenSees Super BeamColumnJoint Model

As shown in Fig. 3, the BeamColumnJoint is a super joint model based on OpenSees,

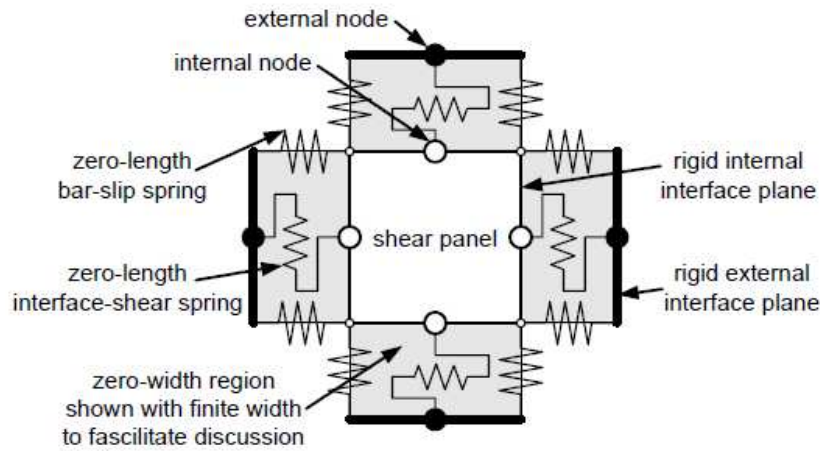


Fig. 3 Components of the Beam-Column Joint

It is a continuous transition element which has 8 nodes included 4 external nodes and 4 internal nodes. Every external node and internal node are in the same rigid interface for ensuring the compatibility of beam and column element. There are two springs between internal rigid interface and external rigid interface, parallelogram is formed on the endpoints of the internal rigid interface to be the link of beam element and column element.

This element performs the 3 failure mechanisms explicitly: the Bar-slip Component are formed by 8 axial springs which are between two rigid interfaces, is to simulate the degradation of stiffness and strength due to bonding deterioration. Four internal rigid interfaces formed parallelogram is to simulate the degradation caused by shear failure named Shear panel Component. Four shear spring which are between internal and external rigid interface is to act the degradation of shear failure under huge earthquake energy. As the equilibrium and deformation are satisfied, we can use these three components to simulate the nonlinear performance of a beam-column joint under seismic action.

Constitutive Model of Concrete

As concrete section is a fiber section, so a constitutive model for cover concrete and core concrete is needed. The modified Kent-Park model was proposed for this element. The restoring force model of Concrete 01 is shown as Fig 4. The constitutive equations and related parameters are as follows,

$$\text{Compression curve equation } \sigma_c = K f'_c \left[\frac{2\varepsilon_c}{\varepsilon_0} - \left(\frac{\varepsilon_c}{\varepsilon_0} \right)^2 \right] (\varepsilon_c \leq \varepsilon_0)$$

$$\text{Linear softening equation } \sigma_c = K f'_c [1 - Z_m(\varepsilon_c - \varepsilon_0)] \geq 0.2K f'_c (\varepsilon_c > \varepsilon_0)$$

$$\text{Where } \varepsilon_0 = 0.002K$$

$$K = 1 + \frac{\rho_s f_y h}{f'_c}$$

$$\text{Descending slope of compression } Z_m = \frac{0.5}{\frac{3+0.29f'_c}{145f'_c-1000} + \frac{3}{4}\rho_s \sqrt{\frac{h''}{s_h}} - 0.002K}$$

Constitutive Model of Steel

OpenSees applies two constitutive models, Steel 01 and Steel 02, to perform the degradation of steel. Among which, Steel 01 is a linear strengthening elastic-plastic reinforcement constitutive model, which is formed by two linear curves. Steel 02 is used to construct a uniaxial Giuffre-Menegotto-Pinto steel material object with isotropic strain hardening. [3] As shown in Fig 5 Steel 02 is used in this study.

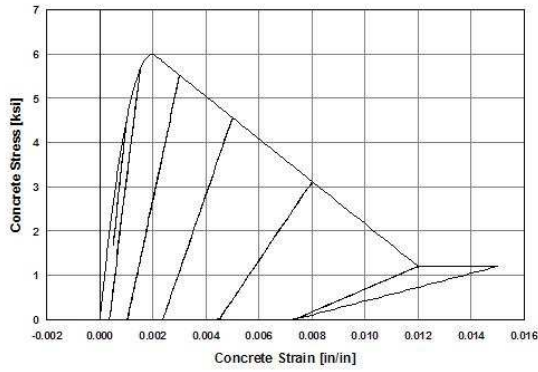


Fig. 4 Constitutive Model of Concrete 01

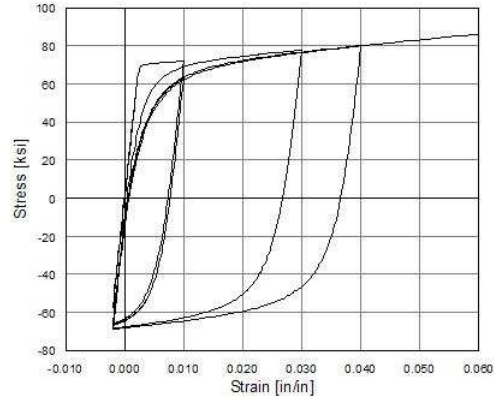


Fig. 5 Constitutive Model of Steel 02

Model Evaluation and Verification

The suggested model is evaluated through comparison of simulated and observed response for beam-column building sub-assemblages tested in the laboratory under virtual earthquake loading. Comparison of these data for series of building beam-column joints investigated by Fumio Kusuhara [4] indicates that the proposed model represents the observed failure mechanisms and fundamental response characteristics of these reinforced-concrete building beam-column joints.

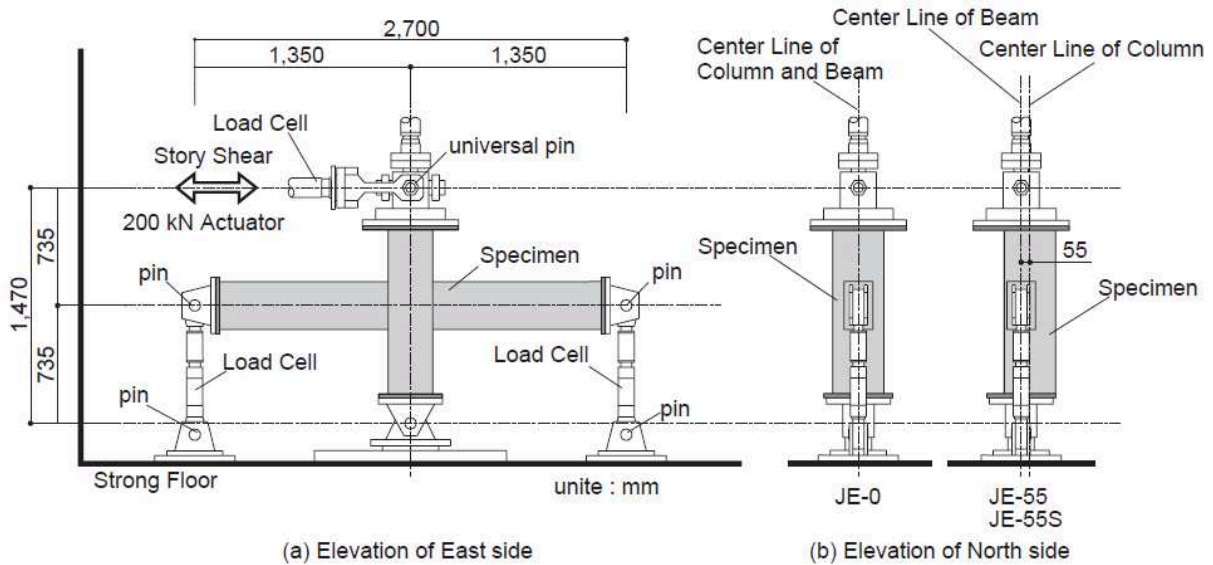


Fig. 6 Loading System

The loading set up is shown in Fig. 6. The specimens were supported in vertical position. Statically cyclic lateral load was applied at the top of the column. The load history is chose by drift angle. After the cycles of 0.125% story drift and 0.25% story drift, two cycles of the same amplitude in story drift were repeated before each displacement amplitude was increased from story drift of 0.5% to 6.0%.

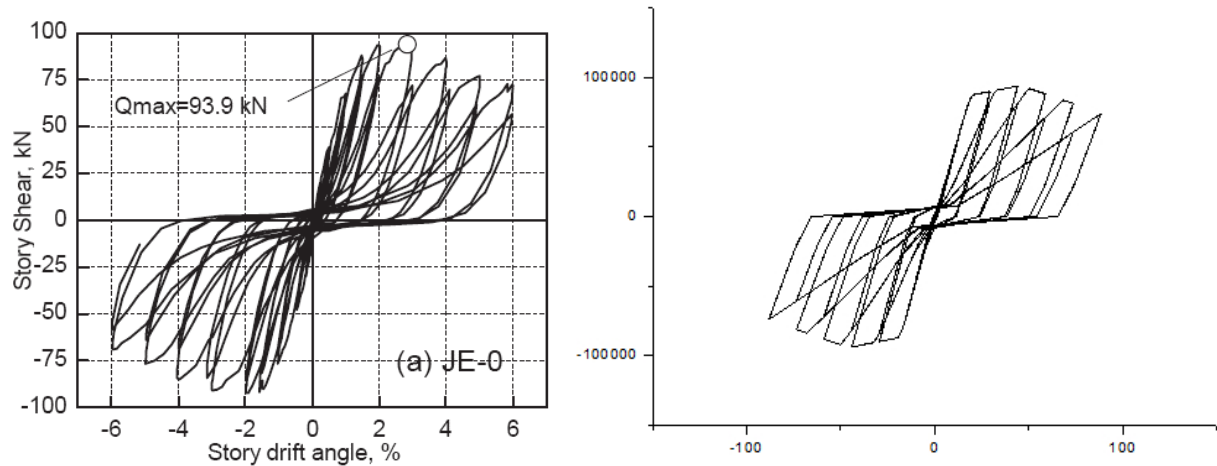


Fig. 7 Observed and Simulated Response of Specimen JE0

Table 1 Observed and Simulated Response Characteristics

	Observed Curve	Simulated Curve	Ratio of Observed to Simulated	Ductility Demand at which Strength Loss is Observed	Pinching of Hysteresis loops
UNIT 1	93.9KN	89.2KN	1.05	No substantial loss at $\mu=4$	Significant

Comparison of simulated and observed response for sub-assemblages tested in the laboratory is shown in Fig. 7 and Table 1. The result indicates that the proposed model is appropriate for use in simulating the earthquake response of building joints with moderate earthquake loads demands.

Conclusion

A descriptive model for beam-column joint has been studied based on OpenSees. OpenSees has advantages over other nonlinear softwares in using new algorithms and the improvement of constitutive model. The results showed that it is proper to use this model to simulate sub-assemblage under earthquake response.

References

- [1] L.N. Lowes, A. Altoontash: Modeling Reinforced-Concrete Beam-Column Joints Subjected to Cyclic Loading. *J. Struct. Eng.*, 129(12), 1686–1697.
- [2] N. Mitra, L.N. Lowes: Evaluation, Calibration, and Verification of a Reinforced Concrete Beam-Column Joint Model. *Journal of Structural Engineering*, Vol. 133, No. 1, January 2007, pp. 105-120
- [3] Filippou, F. C., Popov, E. P., Bertero, V. V. (1983). "Effects of Bond Deterioration on Hysteretic Behavior of Reinforced Concrete Joints". Report EERC 83-19, Earthquake Engineering Research Center, University of California, Berkeley.
- [4] F. Kusuhara, K. Azukawa, H. Shiohara and S. Otami. Test of Reinforced Concrete Interior Beam-Column Joint Subassemblage with Eccentric Beams [R]. 13th World Conference on Earthquake Engineering, Vancouver, B.C., Canada, 2004, Paper No. 185.

A study on the effect of a dyke reinforced by geotextile-encased sand columns

Fang OuYang^{1,a}, Junwei Bi^{1,b}, Jianwei Han^{1,c} and Weiming Liao^{1,d}

¹ School of Civil Engineering, Southwest Jiaotong University, Chengdu, Sichuan, 610031, China

^a245879165@qq.com, ^b1186054378@qq.com, ^c477925591@qq.com, ^d464039003@qq.com

Keywords: Geotextile-encased sand columns; Settlement; Average settlement rate

Abstract. A dyke construction was dealt with geotextile-encased sand columns. The dyke was used to enclose a polder in Hamburg-Finkenwerder, Germany. With the help of geotextile, the columns can be used in very soft soils, even undrained shear strength $c_u < 15$ kN/m², without excessive bulging. After the system is installed, the dike can be filled immediately. To analysis observed data of the long-term settlements in the dyke, three stages can be gotten i.e. "Primary settlements" - "Secondary settlements" - "Creep settlements". Most settlements occurred during the primary filling, while, only little settlements appeared after that construction was accomplished. The settlement rate decreases from the first settlement stage to the last one. No jump takes place when unloading soft soil. Furthermore, the method shorten time and saved a lot of money.

Introduction

Geotextile-Encased sand or stone Columns is made from stone or sand column wrapped with geotextile. The geotextile can be made into shapes of sleeve or bag. First application of encased columns for widening an about 5 m high railroad embankment took place in Hamburg, Germany in 1996. Since then, the new method is used widely for soil improvement in Germany, Sweden and the Netherlands. A lot of researches have been made to expose the performance of this new type[1, 2,3], and many useful results had been gotten, however, few reports on settlement characteristics after construction. This paper based on observed data of a long-term settlements, making an analysis into the effect and the settlements developed characteristics of foundation reinforced by geotextile-encased sand columns. The data are from a land reclamation project for the airplane dockyard (EADS) at the Elbe River in Hamburg, Germany.

Introduction to Engineering[4]

The area-extension project of a airplane dockyard (EADS) in Hamburg-Finkenwerder is located in the 'Mühlenberger Loch'. The project is carried out by enclosing the polder with a 2.4 km long dike.

The thickness of the soft soil layer in this area (here especially contaminated sludge) is between 8 to 14 m. The undrained shear strength c_u in the soft soil is between 0.4 and 10.0 kN/m², as shown in Table 1. Besides, the reclamation site is located in mud flats with low and high tides twice a day.

Table 1 Typical engineering geological conditions

number	soil layer	r [kN/m]	r' [kN/m]	thickness [m]	c' [kN/m ²]	friction angle[°]	W [%]	E_{oed} [kN/m ²]
1	sludge	13	3	4.3	0	20	58-233	500
2	clay	14	4	1.8	0	20	77-192	450
3	peat	11	1	3.7	0	20	75-453	550
4	clay	16	6	1.4	5	20	31-171	1500
5	sand	18	10	-	0	35	-	-

Dealing with GEOTEXTILE ENCASED SAND COLUMN

Geotextile encased sand column is chosen in this project, for it has the benefits of vertical drainage just like stone columns, and with the capabilities of being installed in very soft weak soils without excessive bulging and resultant settlement with help from geotextile.

Geotextile encased sand columns were sunk to the bearing layers, with a diameter of 80 cm, length between 4 and 14 m below the base of the dike footing. The distance between the columns is normally between 1.7 and 2.4 m. The columns under the base of the dike are installed by the vibro displacement method (Figure 1).

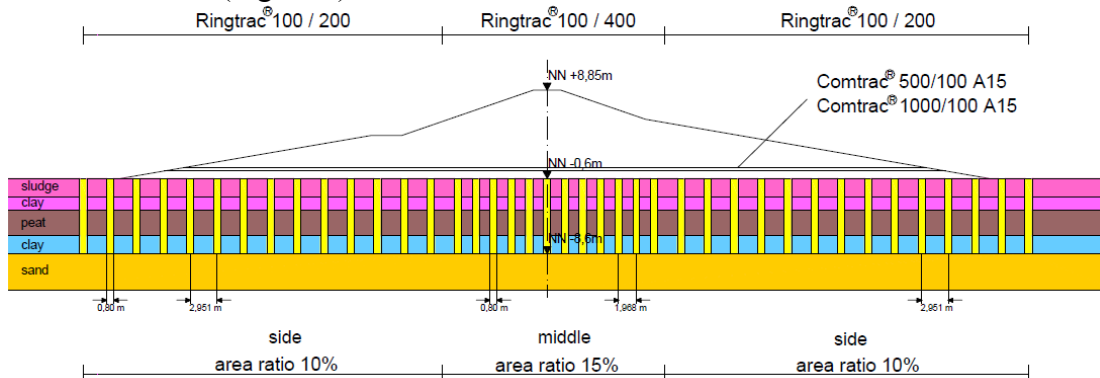


Fig. 1 Cross section of the value engineering concept [Error! Bookmark not defined.]

Development Characteristics of Settlement

Fig. 2 shows the long-time measurements of the dike foundation. From it, settlements increase when the load is added in the process of embankment filling. And the settlement increases slowly instead of jumping obviously during unload soft soil.

The curve can be divided into three stages: The first stage is primary settlement, which the inflection point took place when the fill height is about 7.5m. The settlements subsided are belong to the second stage, which the inflection point took place at about 9.6m fill height. And the last one is creep settlement. The settlement rate in the second stage decreases 81% compared to the first stage. And the settlement rate decreases 83% against the second stage. Rate tends to zero in the last stage. As shown in Table 2.

According to the settlement rate curves, the treatment effect of composite foundation reinforced by geotextile encased sand columns is good. In this kind of foundation reinforced by geotextile encased sand columns, not only the most settlement took place in the first stage, but also does the settlement rate keep convergent state since the beginning of construction. So the purpose of reinforcing dikes and dams can be gained.

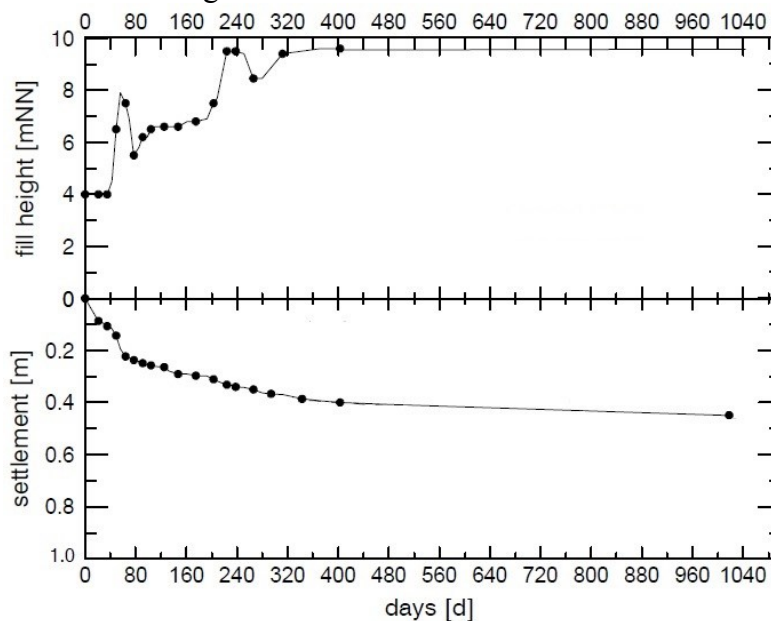


Fig. 2 Results from long-time measurements of the dike foundation [5]

Table 2 The settlements of each stage

stages	duration[d]	settlements[m]	Average velocity[mm/d]	settlements/(total settlements)
primary settlements	70	0.22	3.14	0.490
secondary settlements	270	0.16	0.59	0.355
creep settlements	680	0.07	0.10	0.155

The advantages of geogrid encased stone columns

Stone columns depend on the strength of surrounding soils. And this disadvantage is conquered by geotextile encased sand columns which can be available to reinforce soft soil with low shearing strength, even undrained shear strength c_u is less than 15 kN/m². Besides, geotextile encased sand column is cheap and well-draining just like sand stone, and drain better with the help of geotextile. And in this practical engineering, geotextile encased sand column has good effect.

1 Compared with the rear-anchored raking pile method previously, The solution saves a lot of money. 1) eliminated 35000 tons of steel, since a sheet wall was not necessary ; 2) saved 150000 m² of tidal mud flat reclamation; 3) used 1100000 m³ less sand to fill up the dike , for steeper slope(1:6 against 1:20), and large settlement reductions.

2 Cut down the time. The construction can proceed almost immediately after the installation of the columns. Furthermore, the filtering effect of geotextile can keep draining fluently. With the geotextile encased sand column solution, it was possible to do the foundation work and bring the dike up to the floodproof height of 7 meters above sea level within only eight months, while the original solution need 3 years.

3 The elimination of bulging of the rock column controls the rock quantity, reducing the amount of sand, and making construction costs more predictable.

4 Produced very little noise pollution (12 vibro displacement machines reached a noise level of 50 dba at a distance of 1000 m).

5 Effected a dramatic settlement reduction and a high settlement acceleration similiar to that of vertical drains.

Conclusion

1 Reinforcing cofferdam dyke by geotextile encased sand column method can get better effect. The most settlement took place at the beginning of filling. And after construction is completed, the settlement is very small. The settlement rate decreases gradually, and gets close to zero nearly in the creep settlements. In the period of unload, the rate of settlement keeps almost constant.

2 Due to the effect of geogrid, the soft soil with low strength can be reinforced by geotextile encased sand column effectively. And the bulge of pile decreases greatly.

3 Geotextile encased sand column solution is less expensive and saves more time than the rear-anchored raking pile solution previously.

References

- [1]S.K. Dash and M.C Bora. Influence of geosynthetic encasement on the performance of stone columns floating in soft clay. *Canadian Geotechnical Journal*, 2013, 50(7), 754-765.
- [2] Murugesan S, Rajagopal K. Studies on the behavior of single and group of geosynthetic encased stone columns[J]. *Journal of Geotechnical and Geoenvironmental Engineering*, 2009, 136(1): 129-139.
- [3] Wu C S, Hong Y S. Laboratory tests on geosynthetic-encapsulated sand columns[J]. *Geotextiles and Geomembranes*, 2009, 27(2): 107-120.
- [4] Kempfert H G, Raithel M. Experiences on Dike Foundations and Land Fills on Very Soft Soils[C]//*International Symposium on Soft Soils Foundation Engineering*, Mexico. 2002.
- [5] Raithel M, Kirchner A. Calculation Techniques and Dimensioning of Encased Columns—Design and State of the Art[M]//*Geosynthetics in Civil and Environmental Engineering*. Springer Berlin Heidelberg, 2009: 718-723.

Analysis of a transmission tower structure with dynamic elastic-plastic time history method

Zhonggen Xu^{1, a}, Kang Qin^{2, b} and Changgen Deng^{3, c}

¹Department of Civil Engineering, Guangzhou University, Guangzhou 510006, China;

²Department of Civil Engineering, Guangzhou University, Guangzhou 510006, China;

³Department of Civil Engineering, Tongji University, Shanghai 200092, China

^axuzhonggen@263.net, ^bqinxiaokang_123@163.com, ^ccdengcg@tongji.edu.cn

Keywords: Analysis of Dynamic elastic-plastic time history, Transmission tower, P-DETA effect, Time history curve

Abstract: The idea, procedures and equation of dynamic of analysis of an actual power transmission tower system by dynamic elastic-plastic time history were introduced. Considering P-DETA effect, the base shear forces and curves of top displacement time history were obtained. P-DETA effects on seismic performance of the transmission tower were calculated. The paper can be reference for the analysis of static elastic-plastic.

Introduction

In order to fully grasp the whole process of a structure from elasticity to plasticity, that is, some of its components to be yielded, then cracking to be produced and developed, at last the whole structure to be collapsed, in order to study further and control the conditions of the structure or component damage, and to take active measures to prevent structure to be collapsed, structural elastic-plastic seismic responses analysis to ensure the safety of the structure is needed. In dynamic elastic-plastic time history analysis method, ground motion is input at the basement of a structure. By using elastic-plastic restoring force characteristic of the structure or its components, basic dynamic equations of the whole structure were formed and structural elastic-plastic time history responses were obtained. It not only can calculate vibration amplitudes and frequencies, but also get the influences of the reactions of structure components.

Analysis of dynamic elastic-plastic time history method

Analysis by dynamic elastic-plastic time history method is mainly composed of: to select some appropriate seismic waves, to create a structural model, to create corresponding dynamic calculation equations, to create the restoring force model of the structure or components fitting for actual situation, and to solve dynamic differential equations.

Elastic-plastic movement differential equations of the structure can be written as:

$$[M]\{\ddot{u}(t)\} + [C]\{\dot{u}(t)\} + \{f(u(t))\} = -[M]\{1\}\ddot{u}(t) \quad (2-1)$$

According to soil conditions of the building, several typical earthquake acceleration time history curves with different characteristics were selected as seismic waves for design. Dynamic elastic-plastic analysis of a structure generally can be divided into following steps:

- (1) According to the mechanics characteristics of a structure system, establish a reasonable structural vibration model;
- (2) According to the material properties, structure type and loading condition, choose proper structural restoring force model, and determine restoring force characteristic parameters of feature points and the restoring force characteristic curves of each line segment stiffness value corresponding to cracking, yielding and ultimate displacement
- (3) Establish vibration differential equations of the structure under dynamic loads;
- (4) By step-by-step integration method, solve the vibration equations and get the responses of displacement, velocity and acceleration, and the whole process of structural seismic;
- (5) Draft angles are calculated and checked if they are less than allowable values.

Dynamic elastic-plastic time history analysis of a transmission tower

3.1 An engineering example

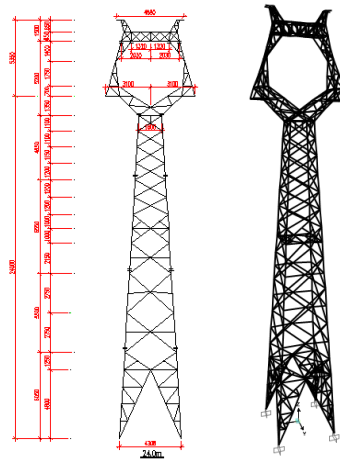


Fig.1. A transmission tower

A transmission tower is shown in Fig.1. Its design seismic intensity is 8 degrees. Its design seismic group is in the second group. Its soil belongs to grade 2. Its basic design seismic acceleration is 0.20g. Its characterized soil period is 0.4s. The transmission tower is a self-supporting cat-head tower ZM1 for 220kV transmission line, with its total height 29.35m, mark-height 24m. According to the specification requirements, two strong earthquake records, EI-Centro wave (NS, 1940) and Tangshan wave, an artificial wave were chosen, and seismic analysis was carried. Time history analysis were carried by Program SAP2000. Adjustment coefficients: 2.049, 10.616 and 6.621 were used to consider different seismic intensities. This type of tower is the most commonly used in our country, because it has a good shape with less wind pressure coefficients than those of other shapes. Even when the number of wires is odd, cat-head tower can also be used.

3.2 Results and analysis

- (1) The maximum base shears and top displacements by nonlinear time history analysis of 8 degrees frequently occurred seismic loads were shown in Table 1.

Table.1 The maximum base shears and top displacements under the 8 degree frequently occurred earthquake

Waveform	Direction	Base shear (kN)	Time (s)	Vertex displacement (mm)	Time (s)
Wave of Elcentro	X	5.22	5.3	3.347	1.1
	Y	8.708	4.5	0.4035	1.4
Wave of Guangzhou	X	5.150	2.9	1.31	8.5
	Y	3.297	8.8	0.1152	5.5
Wave of Tangshan	X	7.739	8.3	6.195	8.3
	Y	13.15	9.8	0.8596	8.3

(2)Base shears and vertex displacements time history curves under three kinds of seismic actions were shown in figure 3-2 to figure 3-13.

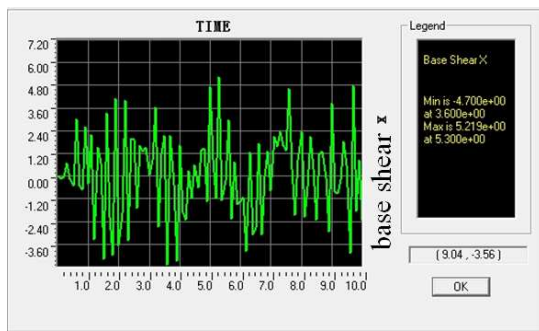


Fig.3-2 Base shear curve under X directional Elcentro wave

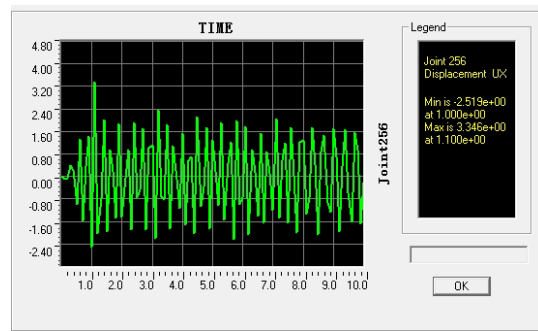


Fig.3-3 Vertex displacement-time curve under X directional Elcentro wave

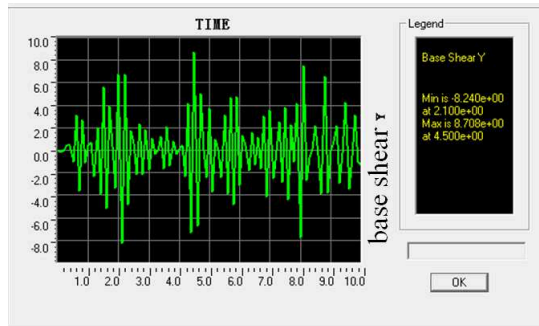


Fig.3-4 Y directional base shear curve under Elcentro wave

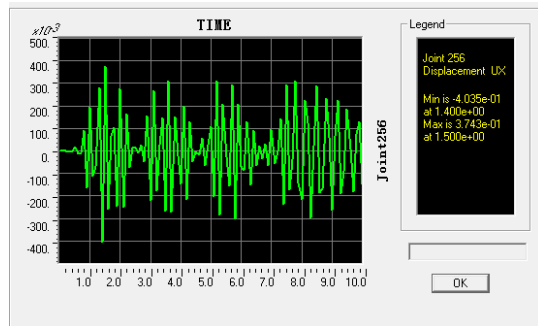


Fig.3-5 Y directional Vertex displacement time curve under Elcentro wave

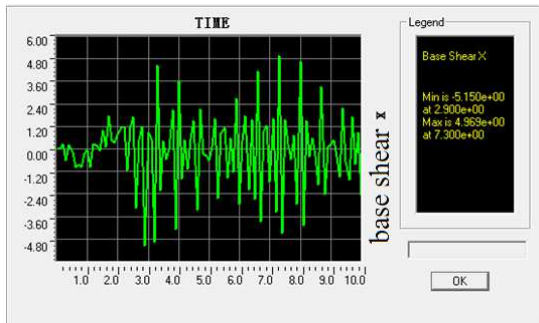


Fig.3-6 X-direction base shear under Guangzhou wave

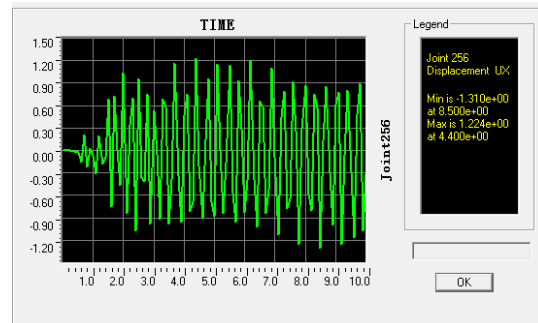


Fig.3-7 X-direction Vertex displacement-time curve under Guangzhou wave

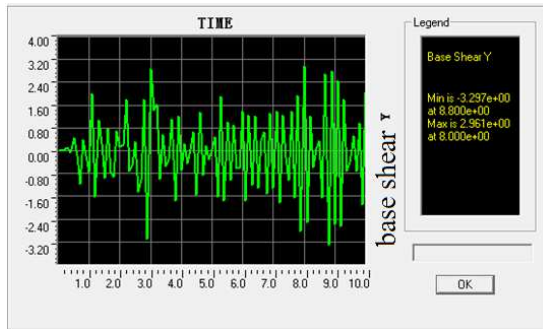


Fig.3-8 Y-direction base shear under Guangzhou wave

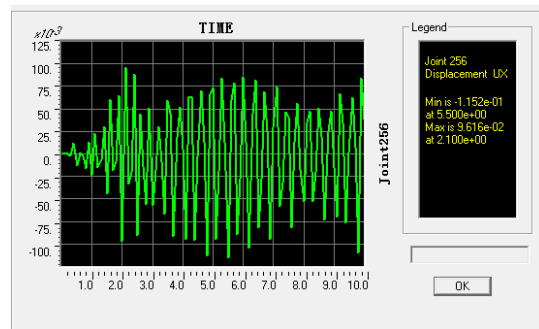


Fig.3-9 Y-direction Vertex displacement-time curve under Guangzhou wave

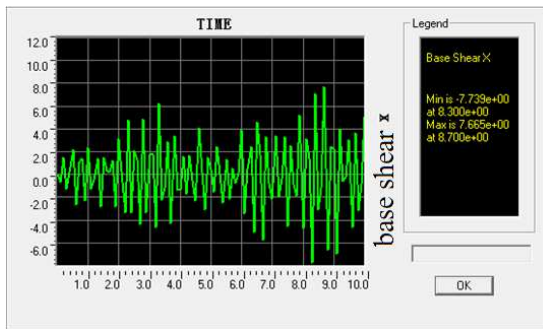


Fig.3-10 X-direction base shear under Tangshan wave

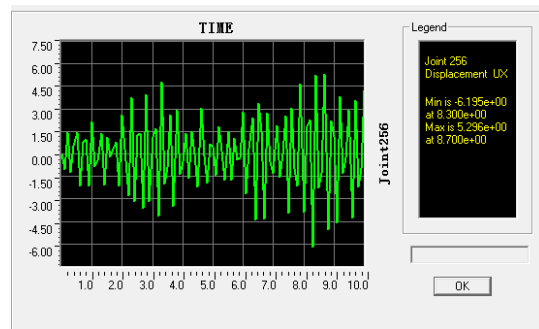


Fig.3-11 X-direction Vertex displacement-time curve under Tangshan wave

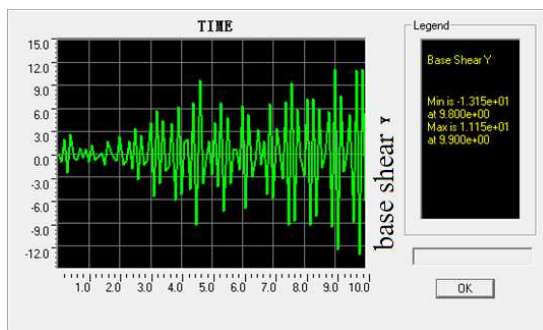


Fig.3-12 Y-direction base shear under Tangshan wave

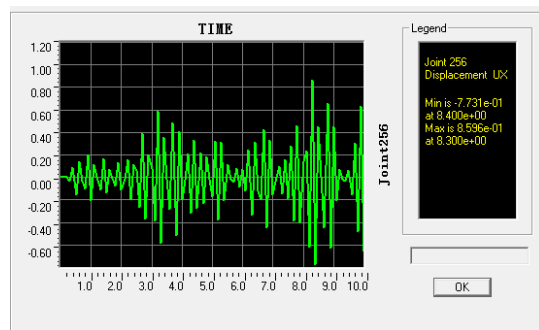


Fig.3-13 Y-direction Vertex displacement-time curve under Tangshan wave

From these tables and time history curves, we can see: under ground motion of Tangshan wave in Y-direction, base shear of the transmission tower gets the maximum 13.15 kN; and under ground motion of Tangshan wave in X-direction, its top displacement along x-direction gets the maximum 6.195 mm.

(3) Under action of 8 degrees of seismic by dynamic elastic-plastic time history analysis, considering P-DETA effect, the maximum base shears and displacements of the vertices were calculated and shown in table 3-2.

Table 3-2 The maximum base shears and top displacements under 8 degree frequently occurred earthquake (considering P-DETA effects)

Waveform	direction	Base shear (kN)	Time (s)	Vertex displacement (mm)	Time (s)
Wave of Elcentro	X	5.219	5.3	3.346	1.1
	Y	8.708	4.5	0.4035	1.4
Wave of	X	5.15	2.9	1.31	8.5

Guangzhou	Y	3.297	8.8	0.1151	5.5
Wave of Tangshan	X	7.739	8.3	6.195	8.3
	Y	13.15	9.8	0.859	8.3

From these tables and time history curves, we see: under the action of Tangshan wave, Y-direction base shear of transmission towers gets the maximum value 13.15 kN; under the wave of Tangshan along X-direction, its top displacement gets the maximum value 6.195 mm. Comparing analysis results of a transmission tower with P-DETA effect and without P-DETA effect, we find that the results of these two cases are very close, so the P-DETA effect can be neglected.

Conclusions

Structural analysis by dynamic elastic-plastic time history method is a very complicated work. From simplifying of the calculation model, determination of restoring force model, selection of seismic waves, results analyzing and post-processing need a lot of work. There are many calculation data and its computation duration is very long. But, it is currently the most ideal method for structural seismic analysis with unique advantage.

References:

- [1] Wang Wei. Response spectrum method and time history analysis in high-level earthquake analysis [D]. In the calculation of the south China university of technology, 2012.(in Chinese)
- [2]. Seismic elastic-plastic time history analysis and reliability study of quayside container crane [J]. Earthquake Science, 2010, 03: 265-274.
- [3] Zhao Boming Wang Ting. High-rise building structure seismic wave input of time history analysis [J]. Journal of Shenyang architectural university (natural science edition), 2010 and practices: 1111-1118. (in Chinese)
- [4] Yang Pu Li Yingmin, Lai Ming. The choice of structure seismic time history analysis method input control index [J]. Journal of civil engineering, 2000, and practices: 33 to 37.(in Chinese)
- [5] Lou Yu, Wenling etc., Based on the flame elastic-plastic time history analysis of structural seismic design [J]. Journal of building structures, 2011, 05:1-8.(in Chinese)

Analysis of Composite Beam with Different Web Openings

Wenyuan Liao^{1, a}, Donghua Zhou^{1, b}, Longqi Li^{1, c}

¹Faculty of civil Engineering, Kunming University of Science and Technology, Kunming 650224, China

^alwy065@126.com, ^b2807505863@qq.com, ^clilongqiqingdao@sina.com

Keywords: Composite Beam, Web Opening, FEM, Non-linear

Abstract: In order to investigate the bearing behavior of composite beam with different web openings. Six composite beams were analyzed by using the finite element program ANSYS and the shape of openings was different. The results show that the shape of opening has a significant influence on the bearing capacity and deformation capacity of composite beams with web openings. Because stress concentration is relatively small, the force performance of circular web opening is more reasonable and has the largest bearing capacity and deformation capacity.

Introduction

Web opening allows the utilities to pass through composite beams in order to save the space beneath the beams, so the total height of the building can be reduced, which results in a substantial reduction in construction cost. The finite element model is established by ANSYS to predict the mechanical properties of them. Because of the processing convenience, rectangular openings are widely used in the practical engineering [1]. The four corners of the rectangular opening is prone to stress concentration, thus strength of section and bearing capacity are significantly decreased [2, 3]. Based on the theory of elasticity, stress concentration in the opening local area can be effectively relieved by changing the shape of opening [4]. The paper analyses the influence of different shapes of opening on the bearing behavior of composite beams under the circumstance of the same area of opening.

Shape of opening

Combined with the engineering practice and consideration of the construction convenience, the design shape of opening includes: square, diamond, rectangle, hexagon and circular. (see Fig.1). All openings have the same area, $A=40000\text{mm}^2$. Six composite beams with different shapes of openings are designed to comparative analysis. Sizes of the specimens are shown in Fig.2.

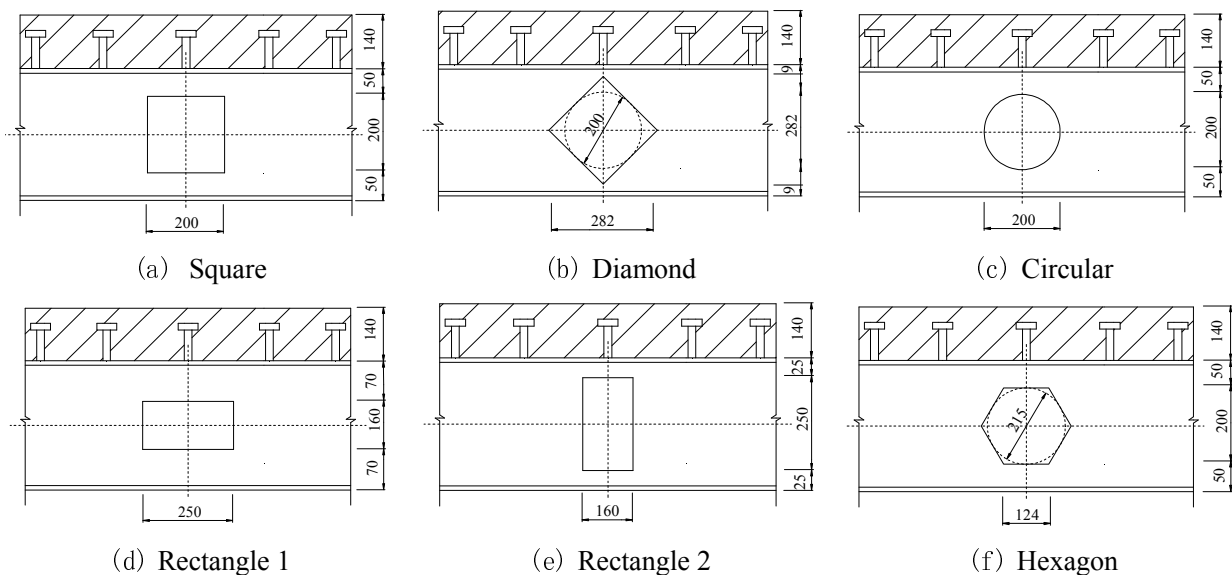


Fig.1 Opening Shape

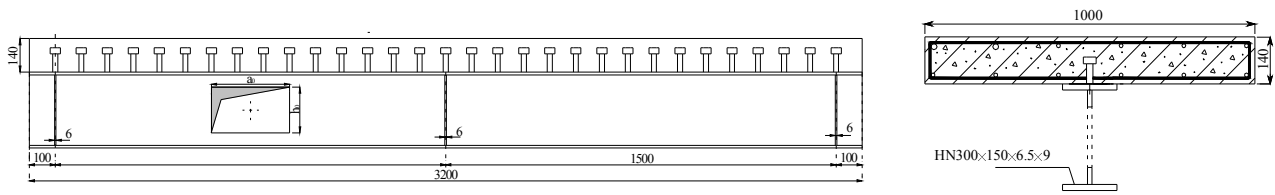


Fig.2 Specimen size

Finite Element Modeling

Element types and material properties. Element types are shown in Fig.3. Solid45 is used for flanges, Plane42 for web, Shell43 for stiffeners, Solid65 for concrete slab, Link8 for steel bar, Beam44 for stud and Combin39 is used to simulate slip deformation. Bilinear isotropic hardening rule is used for steel material together with the Von-Mises yield criteria and the constitutive relation uses the ideal elastoplastic mode (see Fig.4), $f_y = 235\text{MPa}$; $E_s = 2.06 \times 10^5\text{MPa}$; Poisson's ratio is 0.3. Multiple linear isotropic hardening rule is used for concrete together with the Willan-Warneke five-parameter failure criterion and the constitutive relation uses the Hognestad stress - strain curves(see Fig.5), $f_c = 19.1\text{MPa}$; $E_c = 3.25 \times 10^4\text{MPa}$; Poisson's ratio is 0.2; $\epsilon_0 = 0.002$, $\epsilon_u = 0.0038$. Stress - strain curves of stud are shown in Fig.6.

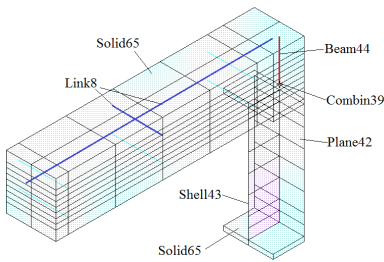


Fig.3 Element types

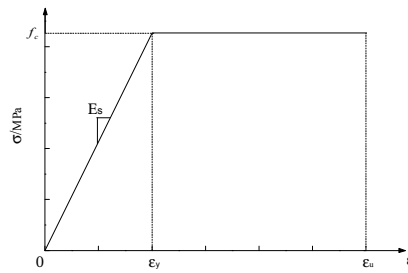


Fig.4 Stress-strain model of steel

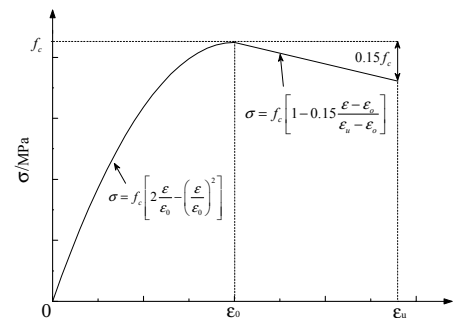


Fig.5 Stress-strain model of concrete

Due to the structural symmetry, it is more effective to model specimen by 1/2 model structure. Elements mesh refining near the opening can improve the accuracy of calculation. Finite element model is shown in Fig.7.

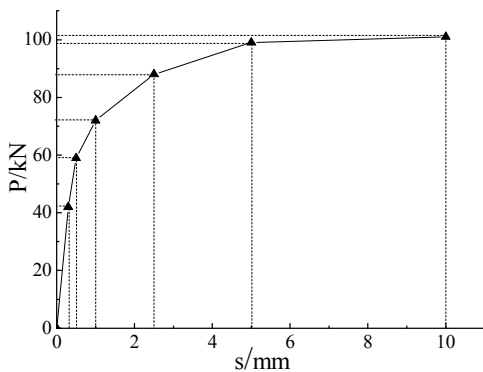


Fig.6 Load-slip model of stud

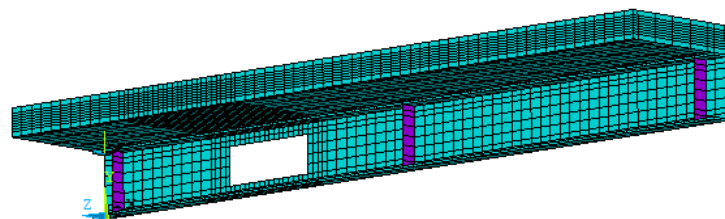


Fig.7 Finite element model

Analysis of calculation results

Bearing capacity and deformation capacity. The load-deflection curves are shown in Fig.8, the ultimate load values and the corresponding deflection values are shown in Table 1.

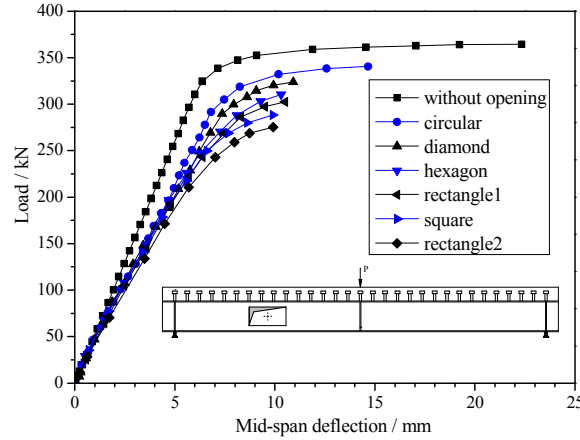


Fig.8 Load-deflection curves of specimens

Table.1 Load values and deflection values

number	stiffener	P_u^i / kN	P_u^i / P_u^1	y_i / mm	y_i / y_1
1	—	364	1.00	22.34	1.00
2	Square	288	1.03	9.88	0.44
3	Diamond	323	1.12	10.92	0.48
4	Circular	340	1.14	14.66	0.65
5	Rectangle 1	302	1.21	10.5	0.47
6	Rectangle 2	275	1.20	9.91	0.44
7	Hexagon	310	1.24	10.3	0.46

P_u^i is ultimate load; y_i is maximum displacement;

Shapes of openings have significant influence on the bearing capacity and deformation capacity of composite beam under the circumstance of the same area of opening. Bearing capacity of specimen with circular opening, diamond opening or hexagon opening (88%~93%) is larger than rectangle or square opening (75%~83%). Among them, specimen with circular opening has the largest bearing capacity (93%), because the circular shape can effectively relieve the stress concentration in the opening. Bearing capacity of rectangle opening, in which long axis is parallel to the beam axis is larger than that of rectangle opening, in which long axis is vertical to the beam axis, for rectangle opening, in which long axis parallel to the beam axis can also relieve the stress concentration. Specimen with circular opening has preferable deformability (66%). Deformation capacity of the other opening shapes are significantly decreased (44%~49%).

Bearing capacity and deformation capacity. The shear values of opening section are shown in Table 2.

Table.2 Shear values of opening section

Opening	V_b	V_t	V_c	V_g	V_c / V_g	V_t / V_g	V_b / V_g
—	—	123.58	39.42	163	0.24	0.76	0.00
Square	32.92	31.13	79.95	144	0.56	0.22	0.23
Diamond	43.13	44.46	74.41	162	0.46	0.27	0.27
Circular	45.17	49.49	75.35	170	0.44	0.29	0.27
Rectangle 1	38.68	36.21	76.11	151	0.5	0.24	0.26
Rectangle 2	28.39	28.96	79.65	137	0.58	0.21	0.21
Hexagon	38.64	40.81	75.55	155	0.49	0.26	0.25

V_b is shear value below opening section; V_t is shear value above opening section;

V_c is shear value of concrete slab; V_g is total shear value;

It can be seen from Table4, shear force of all specimens with different opening shape is mainly undertaken by section above the opening (77%~79%) and concrete slab bears the largest shear force (44%~58%). Concrete slab makes a great contribution to shear strength.

Conclusions

Shape of opening has a significant influence on the bearing capacity and deformation capacity of composite beams with web openings. The force performance of circular web opening is more reasonable and has the largest bearing capacity and deformation capacity. Stress concentration is a main factor on the mechanical performance of different opening shapes. Concrete slab above the opening makes a great contribution to shear strength.

References

- [1] AISC-LRFD, Load and resistance factor design specification for steel structural buildings [S].Chicago: American Institute of Steel Construction Inc, 1999.
- [2] Park J W, Kim C H, Yang S C.Ultimate strength of ribbed slab composite beams with web opening [J].Journal of Structural Engineering, ASCE, 2003, 129(6):810-817.
- [3] Chung K F, Lawson R M.Simplified design of composite beams with large web openings to Eurocode4 [J].Journal of Constructional Steel Research, 2001, 114(3):135-163
- [4] European Committee for Standardization, Eurocode4: Design of composite steel and concrete structures [S]. Brussels: Belgium, 1994.

Analysis of Reconstruction and Reinforcement Design for a Thermal Power Plant Boiler Frame

Jiangling Wu^{1,a}, Pingzhou Cao^{1,b} and Cheng Liu^{1,c}

¹College of Civil and Transportation Engineering, Hohai University, Nanjing, Jiangsu, 210098, China

^awujl0139@163.com, ^bpzcao@hhu.edu.cn, ^cliucheng3009@163.com

Keywords: Boiler frame, Vertical bracing, Reconstruction and reinforcement, Horizontal stiffness, Horizontal bearing capacity

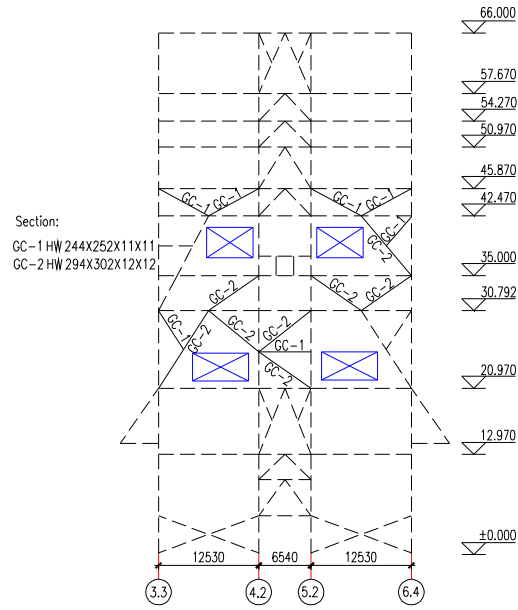
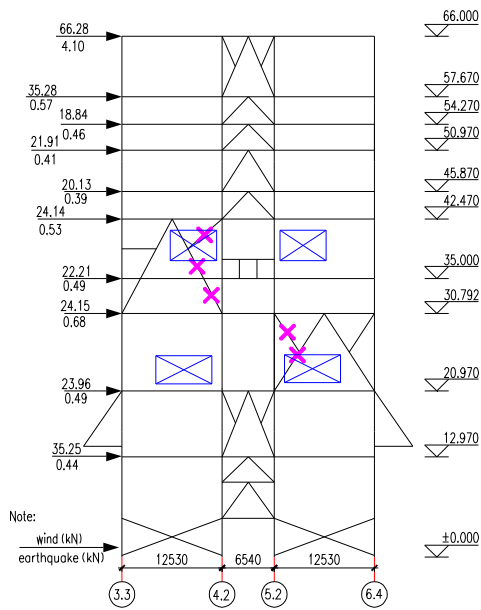
Abstract. It's imperative for thermal power plant to add denitrification system. Denitrification facility is usually arranged between economizer and air pre-heater, which may unavoidably collide with vertical bracings of boiler frame. Based on the denitrification project of a power plant in north China, this paper puts forward a simplified analysis method and a practical reinforcement scheme for boiler frame which needs to remove some bracings. The method is on the basis of effects of vertical bracings on boiler frame. Three models including original structure, demolished one and reinforced one are conducted to study structural behaviour under horizontal loads in SAP2000 software. Considering that bracings between the columns bear horizontal loads mainly and increase the horizontal stiffness of frame, reinforcement design is based on the principle of equal rigidity that the horizontal floor displacement and the proportion of horizontal loads boiler columns bear are approximately same as original.

Introduction

According to current norms of environmental protection in China, the unit with capacity over 300MW in thermal power plant should be equipped with the denitrification system to reduce nitrogen oxide emissions. Denitrification facility is usually arranged between economizer and air pre-heater at present, which results in the change of flow direction of flue gas [1]. So new flue ducts should be installed to connect denitrification system with previous boiler facilities, and new flue ducts have to pass through boiler steel frame to meet the technological requirements. The braced frame system is widely applied in boiler steel frame for its lower cost and more superior working behavior, some vertical bracings between boiler columns need to be dismantled so as to allow new flue ducts to pass through boiler frame. According to relevant codes, the effects of vertical bracing on boiler frame are as follows [2]: bearing and transferring the horizontal loads; improving the lateral stability of boiler column; it can help to form spatial force system that bracings work together with frame columns and beams and strengthen the integral rigidity of boiler frame. If the dismantlement of vertical bracings has great influence on the structural behavior of boiler frame, it should take reinforcement measures to ensure the safety. Based on the denitrification project of a thermal power plant in north China, this paper discusses the simplified analysis method for reinforcement of boiler frame which needs to remove some vertical bracings, and practical reinforcement scheme meeting the arrangement of flue ducts and the limited construction space is researched in this paper, which provides technical references to similar projects.

General engineering situation

The thermal power plant was designed by foreign design institute in the 1990s and boiler steel frame adopts the braced frame system in this project. The boiler frame is located in the zone with a seismic design intensity of 6 degree, its construction site is defined as class I and basic wind pressure is 0.35kN/m^2 . According to the technical layout, four vertical bracings between boiler columns need to be dismantled so as to allow new flue ducts to pass through boiler frame. (see Fig.1). New flue ducts are marked with “” and four vertical bracings are marked with “X” in the figure. The floor elevation is measured in meter.



Analysis method for reinforcement of boiler frame

Criteria of reinforcement design. The boiler has been used for about twenty years, and its working load data can't be obtained now. So it can't be achieved that analyzing the structural behavior of the integrated structure under different original loading conditions and checking members of boiler frame after reconstruction and reinforcement. However, it can be approximately ignored that the impact of vertical bracings on internal force of steel frame under vertical loads [3]. It is considered that vertical bearing capacity of boiler frame changes very little after removing a small part of vertical bracings from it and it does not endanger the safety of structure [4]. Due to the fact that four bracings need to be dismantled and the affected area is small compared to the integrated structure, it could be simplified as a single frame model. Considering that bracings between the columns bear horizontal loads mainly and increase the horizontal stiffness of boiler frame, reinforcement design could be based on the principle of equal rigidity that the horizontal stiffness and bearing capacity of boiler frame after reinforcement are same as original.

Requirements of reinforcement design. The internal force of frame beam and column are related to the deformation of boiler frame, and bracing between the columns helps to improve the performance of frame structure under horizontal loads. There is no change in section size of frame members and original working load in this project, so it is considered that the internal force of boiler frame changes little as long as the horizontal displacement does not increase. The dismantled bracings are located in some floors of boiler frame, which affects mainly structural behavior of the floors where they are located. Therefore new bracings should be built in neighboring floors, and the requirements to realize the criteria of reinforcement design are that the horizontal storey displacement of reinforced structure is not less than the original, the proportion of horizontal loads boiler columns bear and the horizontal component of bracings' stability bearing capacity are same as boiler frame before the reinforcement.

Research on reinforcement scheme of boiler frame

Analysis model. It can be obtained from original design drawings that geometrical sizes of the boiler frame, section size of members, material and boundary restraints. Horizontal loads, including wind and earthquake loads, could be calculated and simplified as joint loads according to present load codes, the joint loads are applied to the lateral nodes of boiler steel frame (see Fig.1). Based on original design data and horizontal loads calculated by load codes, single frame model could be built in SAP2000 software. Three models including original structure, demolished one and reinforced one are conducted to study structural behaviour under horizontal loads.

Reinforcement scheme of boiler frame. It should be made first that comparative analysis of the horizontal stiffness and bearing capacity between boiler frame which has been removed four bracings and original frame. Then it should be decided whether to reinforce boiler frame on the basis of the comparative results.

Fig.3 shows the horizontal storey displacement of boiler frame before and after the dismantlement of four bracings under horizontal loads. The figure shows that the displacements of some floors are about 10 times than original frame. The proportion of horizontal loads boiler columns bear is shown in Fig.4, and it shows the maximum increase of proportion is approximately 40% after the dismantlement of four bracings. Fig.3 and Fig.4 indicate that removing four bracings from boiler frame has great influence on its horizontal stiffness and bearing capacity. In order to maintain the structural safety of boiler frame, it should take some measures to reinforce it, and making the reinforcement scheme should consider the limited construction space.

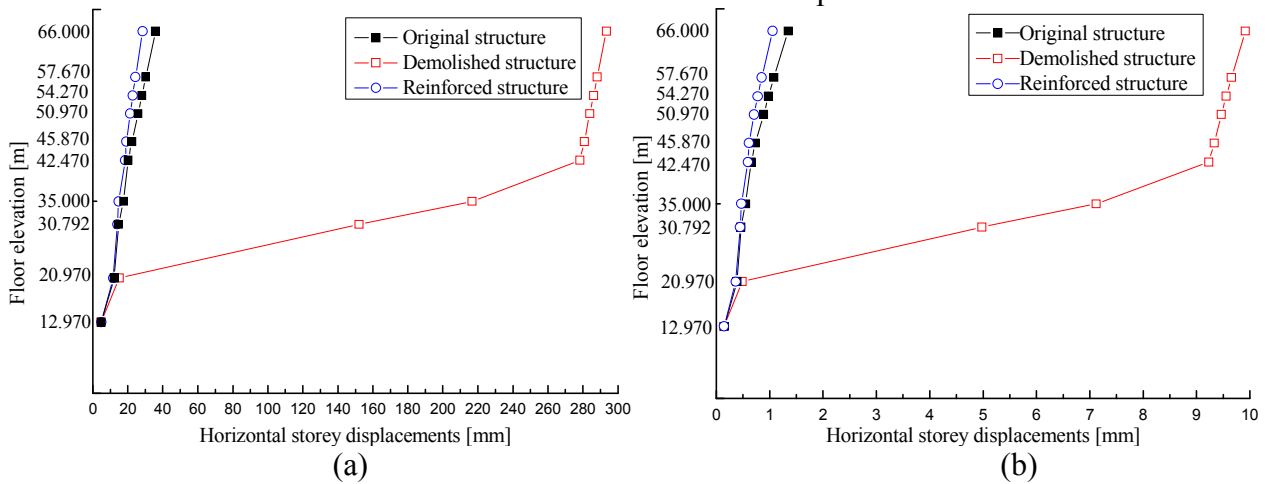


Fig.3 Horizontal storey displacements of original structure, demolished one and reinforced one (a) under wind load (b) under earthquake action.

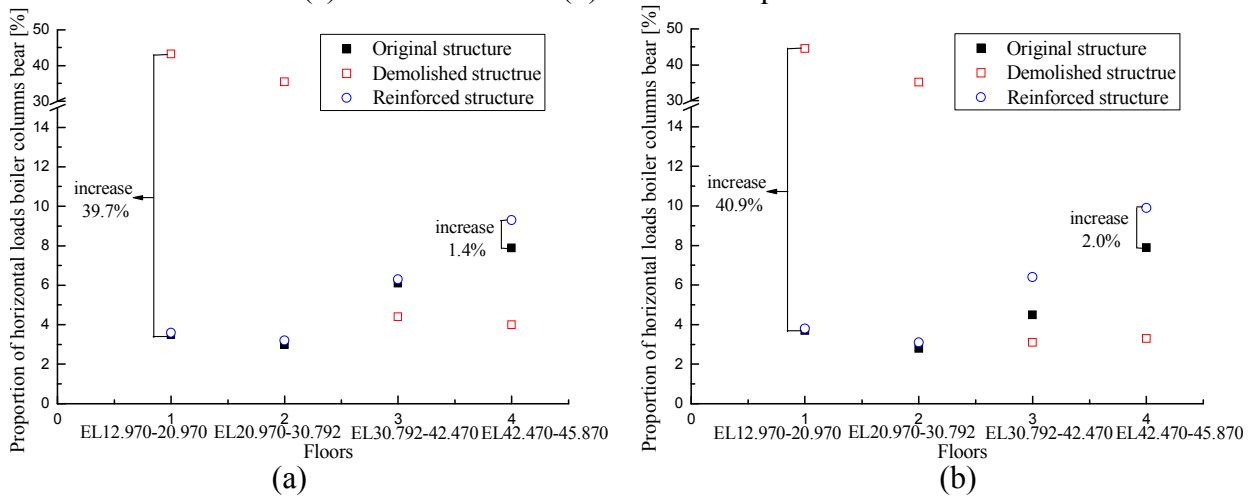


Fig.4 Proportion of horizontal loads boiler columns bear of original structure, demolished one and reinforced one (a) under wind load (b) under earthquake action.

According to the arrangement of flue ducts and the limited construction space, it is practical and economic that building new bracings in neighboring floors to reinforce boiler frame. The newly-built bracings select H-shaped steel in accordance with the existing bracings. The layout and section of new bracings are shown as Fig.2.

Comparison of the horizontal storey displacement. It is shown in Fig.3 that the horizontal displacement of boiler frame after reconstruction and reinforcement under wind and earthquake loads. It shows that the displacement of the reinforced is less than the original. So it meets the requirement of reinforcement design that the horizontal stiffness of the reinforced boiler frame should be same as the original.

Comparison of the proportion of horizontal loads boiler columns bear. The horizontal loads are transformed to the shear force of boiler columns and the horizontal component of bracings' axis force, and the proportion of horizontal loads of reinforced boiler frame bear is shown in Fig.4. It shows that the proportion of horizontal loads boiler columns bear after reinforcement is slightly bigger than the original with a maximum difference of 2%, but the maximum increase of shear stress of boiler column is 0.15 MPa, which occupies about 1‰ of shear strength. So it meets the requirement of reinforcement design that the proportion of horizontal loads boiler columns bear should be same as the original.

Analysis of the horizontal component of bracing' stability bearing capacity. According to Code for Design of Steel Structures [5], it can be calculated in total by the expression given below that the horizontal component of stability bearing capacity of bracings with hinged-hinged end in each floor, and the results are shown in Table 1.

$$N = \sum N_i = \sum \varphi_i A_i f \cdot \cos \beta_i . \quad (1)$$

Where φ_i —stability factor of the i-th bracing;

A_i —gross sectional area of the i-th bracing;

f —design value of steel strength;

β_i —the angle between the i-th bracing and horizontal direction.

Table.1 The horizontal component of bracings' stability bearing capacity

Floor		EL20.970-EL30.792	EL30.792-EL42.470
Horizontal component [kN]	Removed bracings	752.1	580.6
	Newly-built bracings	1823.3	855.8

The table shows that horizontal component of bracings' stability bearing capacity after reinforcement is larger than the original. So it meets the requirement of reinforcement design that the horizontal component of bracings' stability bearing capacity should be same as the original.

Conclusions

Based on the denitrification project of a power plant in north China, this paper puts forward an effective and simplified method for the reinforcement of boiler frame which needs to remove some bracings. This method is on the basis the effects of vertical bracings on boiler frame. Considering that bracings between the columns bear horizontal loads mainly and increase the horizontal stiffness of boiler frame, reinforcement design could be based on the principle of equal rigidity that the horizontal stiffness and bearing capacity of reinforced structure is same as original. Whether the reinforcement scheme meets the design requirements can be judged by the comparative analysis of the horizontal storey displacement and the proportion of horizontal loads boiler columns bear.

References

- [1] Guoqiang Kuang, Dangqi Xu: Thermal Power Generation. Vol. 35 (2006), p.35 (In Chinese)
- [2] GB/T 22395-2008, Specification for design of boiler steel structures, China, 2009.
- [3] Guoqiang Li: *Steel Structures Design for Multistory and Tall Buildings* (China Architecture & Building Press, China 2004). (In Chinese)
- [4] Fusheng Chen, Guohua Qiu and Zhong Fan: *Steel Structures Design for Multistory and Tall Buildings* (China Architecture & Building Press, China 2004). (In Chinese)
- [5] GB 50017-2003, Code for design of steel structures, China, 2003.

Axial Strains in FRP-Confined Normal- and High-Strength Concrete: An Examination of Strain Measurement Methods

Thomas Vincent^{1,a} and Togay Ozbakkaloglu^{1,b}

¹School of Civil, Environmental and Mining Engineering, The University of Adelaide, Adelaide, South Australia, Australia 5005

^atvincent@civeng.adelaide.edu.au, ^btogay.ozbakkaloglu@adelaide.edu.au

Keywords: Concrete; High-strength concrete (HSC); Fiber reinforced polymer (FRP); Confinement; Concrete-filled FRP tubes; Axial strain; Measurement method.

Abstract. This paper presents an experimental investigation into the axial strain measurement method of fiber reinforced polymer (FRP)-confined normal- and high-strength concrete (NSC and HSC). A total of 15 FRP-confined concrete specimens with circular cross-sections were tested under monotonic axial compression. Axial strain recordings were compared on specimens instrumented with three different measurement methods: axial strain gauges and full- and mid-height linear variable displacement transformers (LVDTs). The ultimate conditions are tabulated for each measurement method and key experimental outcomes discussed. The results indicate that axial strains of FRP-confined HSC are highly sensitive to the instrumentation arrangement and significant differences occur in the results obtained from different measurement methods.

Introduction

It is now well-understood that the confinement of concrete with fiber-reinforced polymer (FRP) composites can lead to significant improvements in both compressive strength and ductility for normal- (e.g., [1-5]) and high-strength (e.g., [6-18]) concrete (NSC and HSC) columns. A large number of experimental studies into the axial compressive behavior have been performed over the last two decades producing over 3000 test results, as discussed and assessed in the recent comprehensive review studies Ozbakkaloglu et al. [19] and Ozbakkaloglu and Lim [20]. The results from these studies indicate that although numerous measurements of axial behavior are reported, no single axial strain measurement method is commonly accepted as standard practice.

The aforementioned review studies revealed three main measurement methods for determining axial strain of FRP-confined concrete. The first method determines axial strains from linear variable displacement transformers (LVDTs) mounted along the full specimen height. The second method also uses LVDTs; however, in this arrangement LVDTs are mounted on the specimen surface to measure specimen deformation within a gauge length along the height of the specimen. The final method uses strain gauges attached to the specimen surface aligned in the axial direction. This paper presents the results on an experimental study that was designed to closely examine the influence of these three axial strain measurement methods on FRP-confined specimens. Initially a summary of the test program is provided, which is followed by a comparison of the test specimen ultimate conditions. This is followed by a discussion on the influence of the strain measurement methods on the ultimate axial strains.

Test Program

Test Specimens and Materials. A total of 15 aramid FRP (AFRP) confined cylindrical normal- and high-strength concrete (NSC and HSC) specimens were prepared and tested under axial compression. All specimens were 152 mm in diameter (D) and 305 mm in height (H) and were prepared as FRP-wrapped specimens using a manual wet lay-up technique. Half of the 6 NSC specimens were tested with 150-mm diameter precision cut steel discs that were placed between the loading platens of the testing machine and each specimen end. The applied axial load was transferred directly to the internal concrete core through these discs, thereby avoiding the loading of

the FRP shell in axial compression. In addition to the 6 NSC specimens, 9 HSC specimens with concrete strengths (f'_{co}) ranging from 86 to 121 MPa were tested. All 9 HSC specimens were tested with 150-mm diameter steel discs to transfer the load directly to the concrete core. The details of the test specimens are given in Table 1.

Table 1. Properties of test specimens

Concrete type	Total nominal fiber thickness (mm)	Loading arrangement	Average f'_{co} (MPa)	Number of specimens
NSC	0.6	Concrete only	49	3
		Concrete and FRP jacket		3
HSC	1.2	Concrete only	86	3
		Concrete only	113	3
		Concrete only	121	3
			Total	15

Both the NSC and HSC were batched and mixed in the laboratory and consisted of crushed limestone as the coarse aggregate, with a 10 mm nominal maximum diameter. The properties of the fibers used in the manufacture of the AFRP jackets are shown in Table 2, where type 1 and type 2 fibers were used for the NSC and HSC specimens, respectively. The specimens were prepared using a manual wet lay-up process that involved wrapping epoxy resin impregnated fiber sheets around the cured concrete cylinders in the hoop direction. A thin layer of epoxy resin was applied to the concrete surface prior to wrapping the aramid fiber sheets. NSC specimens were manufactured with a single length of FRP wrapped continuously in the hoop direction, creating 3 layers and a single overlap of 150 mm. Whereas, HSC specimens were confined with 6 layers of AFRP, which were applied through two aramid fiber sheets which terminated at the same overlap region of 150 mm length.

Table 2. Properties of AFRP fibers

Type	Nominal thickness t_f (mm/ply)	Tensile strength f_{fu} (MPa)	Ultimate Tensile Strain ϵ_{fu} (%)	Elastic Modulus E_f (GPa)
Aramid type 1	0.2	2900	2.5	116.0
Aramid type 2	0.2	2600	2.2	118.2

Instrumentation and Testing Procedures. Axial deformations of the specimens were measured using three different methods: (i) four linear variable displacement transformers (LVDTs) mounted at each corner of the steel loading platens with a gauge length of 305 mm; (ii) four LVDTs placed at the mid-height at a gauge length of 170 mm at 90 degree spacing along the circumference of specimens; (iii) three axial strain gauges with a gauge length of 20 mm placed at the mid-height at 120 degree spacing along the circumference of specimens. The strain gauge measurements were used to validate LVDT measurements at the early stages of loading, where discrepancies may exist due to the closure of gaps.

The specimens were tested under monotonic axial compression using a 5000 kN capacity universal testing machine. The loading was applied with load control at approximately 4 kN per second, whereas displacement control was used at approximately 0.005 mm per second beyond the initial softening until specimen failure. Prior to testing, all specimens were capped or ground flat to ensure uniform distribution of the applied pressure. An example of specimen instrumentation and loading arrangement can be seen in Fig. 1.

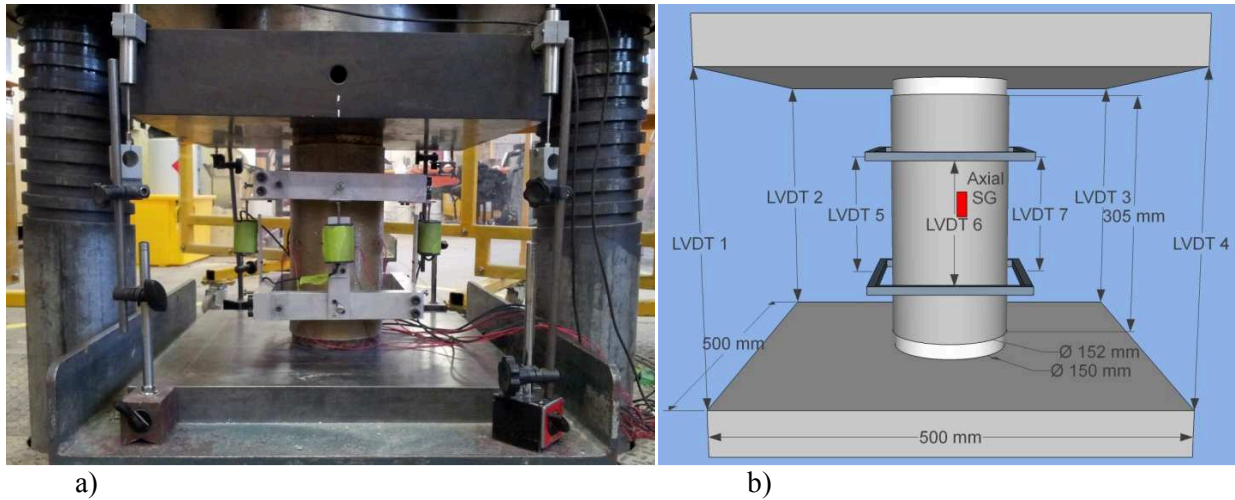


Fig. 1. Instrumentation of specimens: a) specimen before testing; b) technical illustration

Test Results and Discussion

Observed Failure Modes. The observed failure mode of the specimens was rupture of the FRP tube accompanied by an instantaneous loss of applied load. The observed FRP rupture for both NSC and HSC specimens was localized rupture at mid-height. Typical specimen failures are shown in Fig. 2.



Fig. 2. Typical failure of specimens: a) NSC specimens; b) HSC specimens

Specimen Designation. The specimens in Table 1 were labeled as follows: letters N or H were used to represent normal- or high-strength concrete, followed by f'_{co} given in MPa. Specimen end condition details are then given with the letter E corresponding to specimens with end-plates present during loading. Finally a number was provided to identify between nominally identical specimens.

Ultimate Condition. The ultimate condition, which consists of the ultimate axial strength (f'_{cc}) recorded at failure of the specimen and the corresponding axial strain (ϵ_{cc}) of each specimen is reported in Table 3. The ultimate axial strain (ϵ_{cc}) is reported for each measurement method where AFL, AML and ASG correspond to average ultimate strains measured from full-height LVDTs, mid-height LVDTs and mid-height strain gauges, respectively. In this table the strength and strain enhancement ratios (f'_{cc}/f'_{co} and $\epsilon_{cc}/\epsilon_{co}$) are presented where AFL values were used to determine strain enhancement ratio ($\epsilon_{cc}/\epsilon_{co}$). A comparison of the NSC strength and strain enhancement ratios reveals that loading of the FRP jacket during testing does not influence the ultimate condition noticeably.

Table 3. Ultimate condition of test specimens

Concrete type	Specimen	f'_{cc} (MPa)	f'_{cc}/f'_{co}	ϵ_{cc} (%)			$\epsilon_{cc}/\epsilon_{co}$	Average ϵ_{cc} (%)			Differences	
				AFL	AML	ASG		AFL	AML	ASG	AML/AFL	ASG/AFL
NSC	N49-E-1	109.0		3.73	3.64	2.70						
	N49-E-2	103.4	2.14	3.40	3.67	2.25	14.79	3.50	3.52	2.35	1.00	0.67
	N49-E-3	105.3		3.37	3.24	2.10						
	N49-1	107.7		3.41	3.55	2.63						
	N49-2	104.0	2.17	3.22	3.32	1.68	14.24	3.37	3.49	2.01	1.04	0.60
	N49-3	110.1		3.48	3.60	1.72						
HSC	H86-E-1	166.2		2.02	1.23	0.98						
	H86-E-2	168.0	1.94	2.18	1.18	1.01	8.56	2.10	1.19	1.02	0.57	0.49
	H86-E-3	165.2		2.09	1.16	1.07						
	H112-E-1	165.5		1.97	0.97	0.95						
	H112-E-2	168.4	1.47	1.74	0.82	0.78	6.97	1.86	0.97	0.86	0.52	0.46
	H112-E-3	163.1		1.87	1.12	0.85						
	H121-E-1	167.1		1.77	0.74	0.67						
	H121-E-2	172.1	1.40	1.76	0.82	0.55	6.72	1.77	0.80	0.61	0.45	0.35
	H121-E-3	168.4		1.78	0.85	0.62						

Influence of Axial Strain Measurement Method. Table 3 presents the ultimate axial strains (ϵ_{cc}) recorded using the three different measurement methods. A comparison of the average ultimate strain recorded by full- and mid-height LVDTs (AFL and AML) for NSC specimens reveals no significant difference with a reported AML/AFL ratio of approximately 1 for all specimens. A similar comparison is presented for strains obtained from axial strain gauges (ASG), with an ASG/AFL ratio of much lower than 1 obtained for all NSC specimens. This observation indicates that for NSC specimens, LVDTs mounted along the entire height of the specimen record similar axial strains to those by LVDTs mounted at the specimen mid-height. However, axial strains determined from strain gauges are significantly lower than strains determined by their LVDT counterparts, suggesting that the axial strain gauges are incapable of accurately capturing the full specimen deformation.

A comparison of the results for HSC specimens in Table 3 reveals that the difference in axial strains measured using different methods, defined by the ratios of AML/AFL and ASG/AFL, become more significant with an increase in concrete strength (f'_{co}). This outcome can be attributed to the increase in concrete brittleness associated with an increase in concrete strength, which alters the concrete crack patterns from heterogenic microcracks to localised macrocracks. This finding is in agreement with those previously reported in Ozbakkaloglu and Lim [16] based on an investigation of an extensive test database. These observations indicate that the axial strain measurements of FRP-confined HSC are highly sensitive to the instrumentation arrangement and significant differences occur in the results obtained from different measurement methods. It is recommended, therefore, in the interpretation of the results of FRP-confined HSC specimens, due consideration be given to the influence of instrumentation methods.

Conclusions

This paper has presented the results of an experimental study into the influence of axial strain measurement method on FRP-confined NSC and HSC specimens. Based on the results and discussion presented in this paper, the following conclusions can be drawn:

1. In NSC specimens, axial strains obtained from LVDTs mounted along the entire height of the specimen and LVDTs mounted at specimen mid-height are similar. However, axial strains determined from strain gauges do not accurately capture the full specimen deformation.
2. Axial strains of FRP-confined HSC specimens are highly sensitive to the instrumentation arrangement used in the measurement of these strains. The differences in axial strains obtained from different measurement methods become more significant with an increase in concrete strength (f'_{co}).

References

- [1] Karabinis, A., and Rousakis, T.C. (2002) "Concrete confined by FRP material: a plasticity approach". *Engineering Structures* 24(7): 923-32
- [2] Jiang, T., and Teng, J.G. (2007) "Analysis-oriented stress–strain models for FRP-confined concrete". *Engineering Structures*, 29(11): 2968–86
- [3] Saatcioglu, M., Ozbakkaloglu, T., and Elnabelsy, G. (2008) "Seismic behavior and design of reinforced concrete columns confined with FRP stay-in-place formwork". *ACI Special Publication*, SP-257, p. 145-165.
- [4] Ozbakkaloglu, T. (2013). "Compressive behavior of concrete-filled FRP tube columns: Assessment of critical column parameters". *Engineering Structures*, 51, 151-161.
- [5] Ozbakkaloglu, T. (2013). "Concrete-filled FRP tubes: Manufacture and testing of new forms designed for improved performance". *ASCE Journal of Composites for Construction*, 17(2), 280-291.
- [6] Ozbakkaloglu, T., and Saatcioglu, M. (2006). "Seismic behavior of high-strength concrete Columns confined by fiber reinforced polymer tubes." *ASCE Journal of Composites for Construction*, 10(6): 538-549.
- [7] Ozbakkaloglu, T., and Saatcioglu, M. (2007). "Seismic performance of square high-strength concrete columns in FRP stay-in-place formwork." *ASCE Journal of Structural Engineering*, 133(1): 44-56.
- [8] Ozbakkaloglu, T., and Akin, E. (2012). "Behavior of FRP-Confined Normal- and High-Strength Concrete under Cyclic Axial Compression". *ASCE Journal of Composites for Construction*, 16(4): 451-463.
- [9] Idris, Y. and Ozbakkaloglu, T. (2013). "Seismic behavior of high-strength concrete-filled FRP tube columns". *ASCE, Journal of Composites for Construction.*, 17(6), 04013013.
- [10] Lim, J. C., and Ozbakkaloglu, T. (2013). "Confinement model for FRP-confined high-strength concrete". *ASCE Journal of Composites for Construction*, ASCE. 10.1061/(ASCE)CC.1943-5614.0000376.
- [11] Louk Fanggi, B.A., and Ozbakkaloglu, T. (2013). "Compressive behavior of aramid FRP-HSC-steel double-skin tubular columns". *Construction and Building Materials*. 48: 554-565.
- [12] Ozbakkaloglu, T. (2013). "Axial compressive behavior of square and rectangular high-strength concrete-filled FRP tubes". *ASCE Journal of Composites for Construction*, 17(1), 151-161.
- [13] Ozbakkaloglu, T. (2013). "Behavior of Square and Rectangular Ultra High-Strength Concrete-Filled FRP Tubes under Axial Compression". *Composites Part B: Engineering*, 54, 97-111.
- [14] Ozbakkaloglu, T. and Louk Fanggi, B.A. (2013). "FRP-HSC-steel composite columns: Behavior under monotonic and cyclic axial compression". *Materials and Structures*, DOI 10.1617/s11527-013-0216-0
- [15] Ozbakkaloglu, T., and Vincent, T. (2013). "Axial compressive behavior of circular high-strength concrete-filled FRP tubes". *ASCE Journal of Composites for Construction*, 10.1061/(ASCE)CC.1943-5614.0000410
- [16] Vincent, T., and Ozbakkaloglu, T. (2013). "Influence of concrete strength and confinement method on axial compressive behavior of FRP-confined high- and ultra high-strength concrete". *Composites Part B: Engineering*, 50: 413-428.
- [17] Vincent, T., and Ozbakkaloglu, T. (2013). "Influence of fiber orientation and specimen end condition on axial compressive behavior of FRP-confined concrete". *Construction and Building Materials*. 47: 814-826.

- [18] Ozbakkaloglu, T. and Louk Fanggi, B.A. (2014). "Axial Compressive Behavior of FRP-Concrete-Steel Double-Skin Tubular Columns Made of Normal- and High-Strength Concrete." *ASCE Journal of Composites for Construction*, 18(1), 04013027.
- [19] Ozbakkaloglu, T., Lim, J.C., and Vincent, T. (2013). "FRP-confined concrete in circular sections: Review and assessment of the stress-strain models". *Engineering Structures*, 49: 1068-1088.
- [20] Ozbakkaloglu, T., and Lim, J. C. (2013). "Axial compressive behavior of FRP-confined concrete: Experimental test database and a new design-oriented model". *Composites Part B: Engineering*, 55: 607-634

Comparison of Stress-Strain Relationships of FRP and Actively Confined High-Strength Concrete: Experimental Observations

Jian Chin Lim^{1, a} and Togay Ozbakkaloglu^{1, b}

¹School of Civil, Environmental and Mining Engineering, University of Adelaide, Adelaide, Australia

^ajlim@civeng.adelaide.edu.au, ^btogay.ozbakkaloglu@adelaide.edu.au

Keywords: High-strength concrete (HSC); Fiber reinforced polymer (FRP); Active; Triaxial; Compression; Confinement mechanism; Lateral strain; Axial strain; Stress-strain.

Abstract. It is well established that lateral confinement of concrete enhances its axial strength and deformability. It is often assumed that, at a same level of confining pressure, the axial compressive stress and strain of fiber reinforced polymer (FRP)-confined concrete at a given lateral strain are the same as those in concrete actively confined concrete. To assess the validity of this assumption, an experimental program relating both types of confinement systems was conducted. 25 FRP-confined and actively confined high-strength concrete (HSC) specimens cast from a same batch of concrete were tested under axial compression. The axial stress-strain and lateral strain-axial strain curves obtained from the two different confinement systems were assessed. The results indicate that, at a given axial strain, lateral strains of actively confined and FRP-confined concretes correspond, when they are subjected to the same lateral confining pressure. However, it is observed that, at these points of intersections on axial strain-lateral strain curves, FRP-confined concrete exhibits a lower axial stress than the actively confined concrete, indicating that the aforementioned assumption is not accurate. The test results indicate that the difference in the axial stresses of FRP-confined and actively confined HSC becomes more significant with an increase in the level of confining pressure.

Introduction

Since 1920s [1], a significant research effort has been dedicated to understanding the behavior of concrete under lateral confinement. More recently, research attention has turned to the potential applications of fiber reinforced polymer (FRP) composites as concrete confinement in retrofitting existing concrete columns [2-4] and in the construction of new high-performance composite columns [5-18]. A recent comprehensive review study [19] revealed that over 200 experimental studies have been conducted over the last two decades on the compressive behavior of FRP-confined concrete, resulting in the development of over 80 axial stress-strain models. Among these models, the analysis-oriented models were found to be particularly versatile as they are capable of establishing the complete axial stress-strain and lateral strain-axial strain curves of FRP-confined concrete on the basis of interaction mechanism between the external confining shell and internal concrete core. Such models (e.g., [20, 21]) are built on the assumption that the axial compressive stress and strain of FRP-confined concrete at a given lateral strain are the same as those of the concrete actively confined under a confining pressure equal to that supplied by the FRP shell. However, this assumption, known as the path independency assumption, is yet to be validated experimentally through investigation of companion FRP-confined and actively confined specimens.

In this study, compressive tests on FRP-confined and actively confined high-strength concrete (HSC) were conducted to study the influence of the path of applied confining pressure in the two different types of confinement systems, and hence to assess the validity of the path independency assumption. The challenge of this study lies on the preparation of companion specimens that had consistent test parameters, including specimen dimensions and material properties, except for the types of confinement systems. An extensive review of the literature has revealed that the study reported in this paper is the first of its kind [6, 13].

Experimental Program

Test Specimens and Materials. A total of 25 HSC specimens were prepared from a same batch of concrete. To attain a consistent homogeneity for the concrete specimens, the concrete was cast in a large block of $410 \times 410 \times 140$ mm in dimensions, from which cylindrical cores of 63 mm diameter were extracted. The cores were then ground to lengths of 126 mm using a surface grinding machine. The average 28-day compressive strength of the HSC specimens was 128 MPa.

Two confinement systems, with one producing constant hydrostatic confining pressure using triaxial Hoek cell and the other producing passively increasing confining pressure using FRP jackets, were used to confine the test specimens. Two of the specimens were unconfined, fourteen were actively confined and nine were FRP-confined concrete cylinders. A minimum of two nominally identical specimens were tested for each unique specimen configuration. The actively confined specimens were tested under triaxial compressions with hydraulic pressure of the Hoek cell of 2.5, 5, 7.5, 10, 15, 20, or 25 MPa. The FRP-confined specimens were tested under axial compression using the same machine. Out of the nine FRP-confined specimens, three were wrapped with Aramid FRP (AFRP) jackets, three with Carbon FRP (CFRP) jackets, and the remaining three with S-Glass FRP (GFRP) jackets. The specimens were wrapped with two layers of FRP using a manual wet lay-up process by wrapping epoxy resin impregnated fiber sheets onto the concrete cylinders in the hoop direction. All specimens were wrapped with one continuous sheet with a single 66-mm long overlap zone. The material properties of the unidirectional fiber sheets used to manufacture the FRP jackets are provided in Table 1. The table reports both the manufacturers supplied fiber properties and those obtained from FRP coupon tests.

Table 1. Material properties of fibers and FRP composites

Type	Nominal thickness t_f (mm/ply)	Provided by manufacturers			Obtained from coupon tests*		
		Tensile strength f_f (MPa)	Ultimate tensile strain ϵ_f (%)	Elastic modulus E_f (GPa)	Tensile strength f_{frp} (MPa)	Ultimate tensile strain ϵ_{frp} (%)	Elastic modulus E_{frp} (GPa)
Aramid	0.200	2600	2.20	118.2	2390	1.86	128.5
Carbon	0.111	4370	1.90	230.0	4152	1.76	236.0
S-Glass	0.200	3040	3.50	86.9	3055	3.21	95.3

* calculated based on nominal thickness of fibers

Instrumentation and Testing. The specimens were tested under axial compression using a 1000-kN capacity Instron testing machine that was connected to a computer for command signals and data acquisition. The axial load was applied with displacement control at a rate of 0.003 mm per second. For the actively confined specimens, a 30-MPa capacity Hoek cell was used to apply lateral pressure on specimens. A confining pressure intensifier was used to fill and pressurize the Hoek cell. Before the application of the axial load, the lateral pressure was applied at a load rate of 0.314 kN per second until the required active confining pressure was achieved. The pressure was then monitored and manually controlled using a pressure gauge and a hand pump.

The lateral strains of the actively confined specimens were measured using four 10-mm unidirectional strain gauges placed at the mid-height of specimens. The lateral strains of the FRP-confined specimens were using six 5-mm unidirectional strain gauges placed at the mid-height of specimens. The axial strains of the specimens were measured using two linear variable displacement transformers (LVDTs) mounted at the steel loading platens with a gauge length of 126 mm.

Test Results and Discussions

All the actively confined specimens failed by concrete crushing, whereas all of the FRP-confined specimens failed by the ruptures of FRP jackets triggered by expansion of concrete as a result of progressive crushing. Figs. 1 to 3 show the comparison of the axial stress-strain and lateral strain-axial strain curves of actively and FRP-confined specimens. As illustrated in the figures, the shapes of the axial stress-strain and lateral strain-axial strain curves are highly dependent on the paths of confining pressure applied onto the concretes.

Intersecting Points of Lateral Strain-Axial Strain Curves. As can be seen from Figs. 1(a) to 3(a), the lateral strain-to-axial strain curves of the FRP-confined specimens intersect the curves of the actively confined specimens sequentially in the order of increasing confining pressure. To study the influence of the applied confining pressure on the lateral and axial strains of concretes in the two different types of confinement systems, the confinement ratios of FRP-confined and actively confined specimens at the intersecting points of their lateral strain-axial strain curves, as marked in Figs. 1(b) to 3(b), were compared. Fig. 4(a) shows the comparison of the confinement ratios of FRP-confined specimens (f_l/f'_{co}) and actively confined specimens (f^*_l/f'_{co}) at the points of intersections. As can be seen from Fig. 4(a), the confinement ratios of the FRP-confined and actively confined specimens at the points of intersections are close to each other and they yield a strong correlation. This observation suggests that the lateral strain-to-axial strain relationships of both FRP-confined and actively confined concretes depend on the instantaneous confining pressure at the corresponding axial strain.

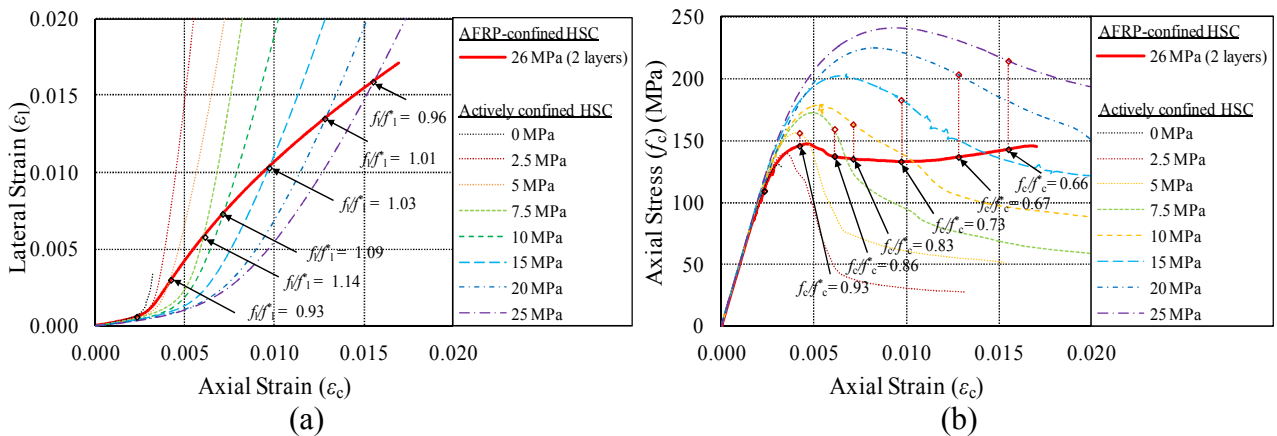


Fig. 1. Comparison of actively confined and AFRP-confined specimens: (a) lateral strain-axial strain curves; (b) axial stress-strain curves

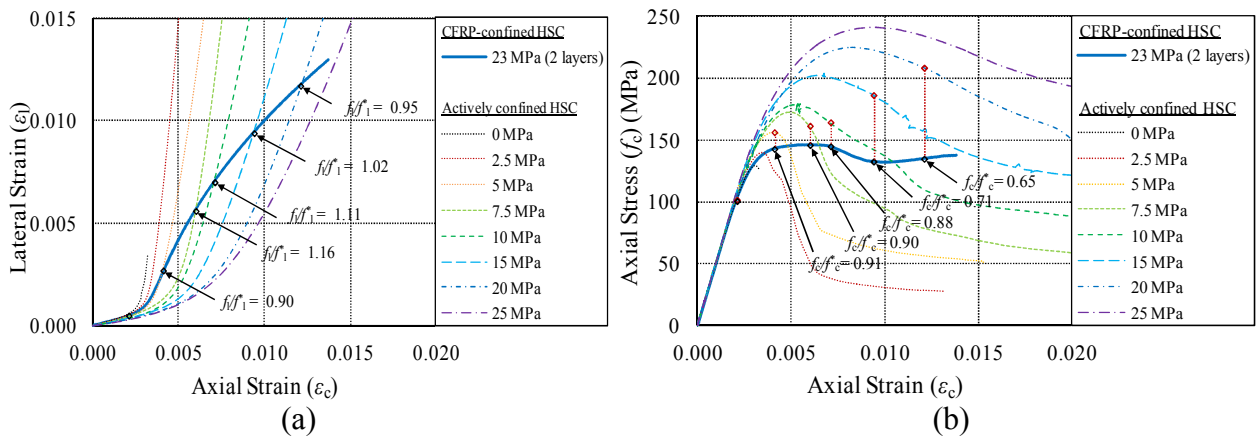


Fig. 2. Comparison of actively confined and CFRP-confined specimens: (a) lateral strain-axial strain curves; (b) axial stress-strain curves

Axial Stress Difference in Stress-Strain Curves of Active and FRP-Confined HSC. To compare the levels of axial stresses achieved in specimens confined by the two different systems, the coordinates of the axial stresses and axial strains corresponding to the points of intersections in Figs. 1(a) to 3(a) are marked in Figs. 1(b) to 3(b) for comparison. At these points of intersections, the levels of confining pressures of the FRP-confined and actively confined specimens are comparable, as illustrated in Fig. 4(a). However, as evident from Figs. 1(b) to 3(b), the axial stresses achieved in FRP-confined specimens are significantly lower than those achieved in actively confined specimens, at the given levels of confining pressure. This difference in the axial stresses is clear evidence that the axial stress-strain relationships of FRP-confined and actively confined HSC are dependent on the path of applied lateral confining pressure in the different confinement systems.

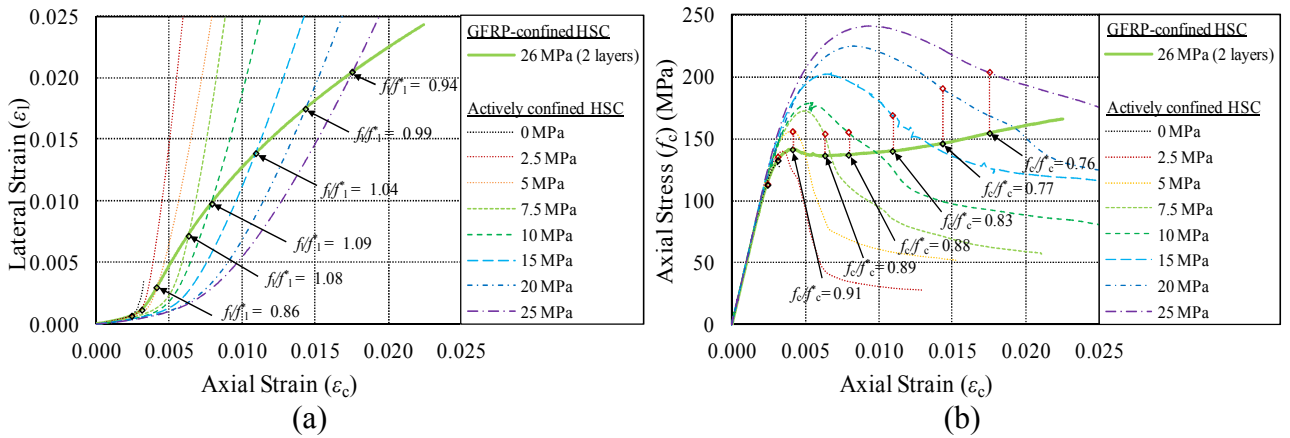


Fig. 3. Comparison of actively confined and GFRP-confined specimens: (a) lateral strain-axial strain curves; (b) axial stress-strain curves

The difference in the axial stresses in FRP-confined and actively confined HSC can be quantified in terms of an axial stress reduction factor (f_c/f_c^*). Fig. 4(b) shows the relationship of the stress reduction factor (f_c/f_c^*) with FRP confinement ratio (f_l/f_{co}). As evident in the Fig. 4(b), the axial stress reduction factor (f_c/f_c^*) reduces with an increase in an increase in the confinement ratio (f_l/f_{co}). However, currently available data are not yet sufficient for the quantification of the stress reduction factor (f_c/f_c^*). Additional experimental studies are currently underway at the University of Adelaide to further investigate the important parameters, which will enable accurate quantification of this important effect.

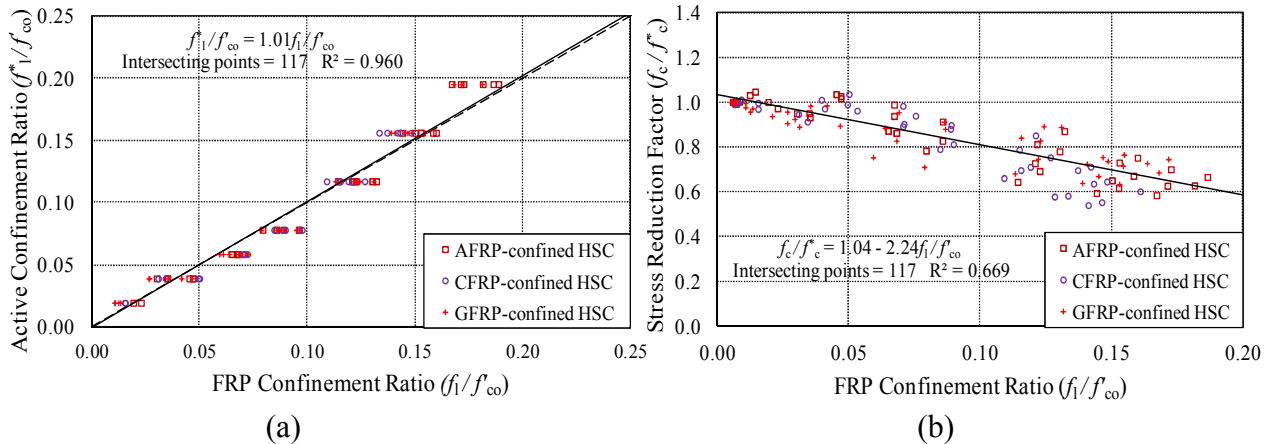


Fig. 4. Variations of: (a) confinement ratios of actively confined HSC (f_l^*/f_{co}^*) and FRP-confined HSC (f_l/f_{co}) at points of intersection on lateral strain-axial strain curves, and (b) axial stress reduction factor (f_c/f_c^*) with FRP confinement ratio (f_l/f_{co})

Conclusions

An experimental program was undertaken to identify the change in the axial stress-strain and lateral strain-axial strain behaviors of HSC under different confinement systems provided by triaxial Hoek cell and FRP jacketing. Based on the experimental observations the following conclusions can be drawn:

1. At a given axial strain, lateral strains of actively confined and FRP-confined concretes correspond, when they are subjected to the same lateral confining pressure. This finding suggests that the lateral strain-to-axial strain relationships of both actively confined and FRP-confined HSC depend on the instantaneous confining pressure at the corresponding axial strain.
2. On the other hand, at a given axial and lateral strain and confining pressure, FRP-confined HSC exhibits significantly lower axial stress compared to that of companion actively confined HSC. The difference in the axial stresses becomes more significant with an increase in the level of confining

pressure. This difference in the axial stresses is clear evidence that the axial stress-strain relationships of FRP-confined and actively confined HSC are dependent on the path of applied lateral confining pressure.

References

- [1] Richart, F.E., Brandtzaeg, A., and Brown, R.L., (1928). "A study of the failure of concrete under combined compressive stresses." *Bulletin No. 185*, University of Illinois, Champaign, Illinois.
- [2] Lam, L. and Teng, J.G., (2004). "Ultimate condition of fiber reinforced polymer-confined concrete." *J. Compos. Constr.*, 8(6), 539-548.
- [3] Ozbakkaloglu, T. and Akin, E., (2012). "Behavior of FRP-confined normal- and high-strength concrete under cyclic axial compression." *J. Compos. Constr.*, 16(4), 451-463.
- [4] Rousakis, T.C. and Karabinis, A.I., (2012). "Adequately FRP confined reinforced concrete columns under axial compressive monotonic or cyclic loading." *Mater. Struct.*, 45(7), 957-975.
- [5] Saatcioglu, M., Ozbakkaloglu, T., and Elnabesy, G. (2008). "Seismic Behavior and Design of Reinforced Concrete Columns Confined with FRP Stay-in-place Formwork." *ACI Special Publication SP-257*, 145-165.
- [6] Idris, Y. and Ozbakkaloglu, T., (2013). "Seismic behavior of high-strength concrete-filled FRP tube columns." *J. Compos. Constr.*, 17(6), 04013013.
- [7] Lim, J.C. and Ozbakkaloglu, T., (2013). "Confinement model for FRP-confined high-strength concrete." *J. Compos. Constr.*, 10.1061/(ASCE)CC.1943-5614.0000376.
- [8] Louk Fanggi, B.A. and Ozbakkaloglu, T., (2013). "Compressive behavior of aramid FRP-HSC-steel double-skin tubular columns." *Constr. Build. Mater.*, 48, 554-565.
- [9] Ozbakkaloglu, T., (2013). "Axial compressive behavior of square and rectangular high-strength concrete-filled FRP tubes." *J. Compos. Constr.*, 17(1), 151-161.
- [10] Ozbakkaloglu, T., (2013). "Behavior of square and rectangular ultra high-strength concrete-filled FRP tubes under axial compression." *Composites Part B: Engineering.*, 54, 97-111.
- [11] Ozbakkaloglu, T., (2013). "Concrete-filled FRP Tubes: Manufacture and testing of new forms designed for improved performance." *J. Compos. Constr.*, 17(2), 280-291.
- [12] Ozbakkaloglu, T., (2013). "Compressive behavior of concrete-filled FRP tube columns: Assessment of critical column parameters." *Eng. Struct.*, 51, 188-199.
- [13] Ozbakkaloglu, T. and Lim, J.C., (2013). "Axial compressive behavior of FRP-confined concrete: Experimental test database and a new design-oriented model." *Compos. Part B*, 55.
- [14] Ozbakkaloglu, T. and Louk Fanggi, B.A., (2013). "FRP-HSC-steel composite columns: Behavior under monotonic and cyclic axial compression." *Mater. Struct.*, 10.1617/s11527-013-0216-0.
- [15] Ozbakkaloglu, T. and Vincent, T., (2013). "Axial compressive behavior of circular high-strength concrete-filled FRP tubes." *J. Compos. Constr.*, 10.1061/(ASCE)CC.1943-5614.0000410.
- [16] Vincent, T., and Ozbakkaloglu, T. (2013). "Influence of concrete strength and confinement method on axial compressive behavior of FRP-confined high- and ultra high-strength concrete". *Compos. Part B*, 50, 413-428.
- [17] Vincent, T. and Ozbakkaloglu, T., (2013). "Influence of fiber orientation and specimen end condition on axial compressive behavior of FRP-confined concrete." *Constr. Build. Mater.*, 47, 814-826.

- [18] Ozbakkaloglu, T. and Louk Fanggi, B.A. (2014). "Axial Compressive Behavior of FRP-Concrete-Steel Double-Skin Tubular Columns Made of Normal- and High-Strength Concrete." *J. Compos. Constr.*, 18(1), 04013027.
- [19] Ozbakkaloglu, T., Lim, J.C., and Vincent, T., (2013). "FRP-confined concrete in circular sections: Review and assessment of stress–strain models." *Eng. Struct.*, 49, 1068–1088.
- [20] Binici, B., (2005). "An analytical model for stress-strain behavior of confined concrete." *Eng. Struct.*, 27(7), 1040-1051.
- [21] Jiang, T. and Teng, J.G., (2007). "Analysis-oriented stress-strain models for FRP-confined concrete." *Eng. Struct.*, 29(11), 2968-2986.

Construction Control of a Continuous Beam Arch Composite Bridge

ZHOU Chong-yang^{1,a}, YANG Jian-rong^{1,b}, ZHU Wei-min^{1,c} and SHI Jiao^{1,d}

¹ Kunming University of Science and Technology, Department of Civil Engineering, Yunnan
Kunming 650000, China

^a826331650@qq.com, ^bcarpenter_y@sina.com, ^czwm3129@163.com, ^d843941405@qq.com

Keywords: steel structure; continuous beam arch composite bridge; high-order hypostatic structure; landing gear control; temperature stress

Abstract. The geometric shape and internal forces were monitored during the construction of the hypostatic framework structure which is a composite system of steel beam and arch. The displace settlement was measured for the control of the geometric shape. And nine vibrating wire strain gauges were embedded on the key sections for the real time control of internal force. In order to cancel out the interference of the temperature variation effectively, displace settlement and internal forces were monitored around the clock at different time points. Then the measured values were compared with the theoretical values. Based on the measurement of temperature variation and strain, the settlement during the process of frame construction can be surely ascribed to thermal stress in the high redundancy structure. It should pay close attention to the changes in the future similar steel Beam Arch Composite Bridge construction and monitoring system.

Introduction

Beam Arch Composite Bridge combined the arch ribs which mainly withstand the axial force and the beam which sustain the moment and live loads ^[1]. This new bridge design theory has matured, while the design process did not consider the structural displacement effect on the structural internal forces. And for the larger arch span, additional moment generated by the displacement of the structure can not be ignored ^[2]. The landing gear control on the formation of arch linear space plays a key role. In engineering practice, it is found that the temperature variation plays a greater impact on the similar bridge structure. Moreover, it has certain unpredictability ^[3-5].

Project Overview

Mirage Bridge, located in Yuxi city where the diurnal temperature variation is large (the temperature difference between the deck is 21.2°C by situ measurement), across the Zhouda river, was the main north-south campus channel with the length as 92.5 meter. The deck standard width is 10 meter (shown in Fig. 1). The bridge was set three ribs, the middle of which is vertical plane rib, side ribs are the space curve linear tilting, with tilt angle as 36.03 °.

The Finite Element Model

Mirage Bridge model used lattice theory to establish a simplified model by Midas Civil 2012 software package ^[6,7], with steel deck equivalent to the beams, that is, only consider the lateral stiffness impact that the steel deck put on the beams.

Since the bridge was built as non-articulated arch bridge, the foot of the arch are fixed connection. The contact part of the both sides spans and bridge approach released translational degrees of freedom at X axis (vertical bridge) and rotational degrees of freedom around the Y axis (the bridge landscape).

Full-bridge structure weight was added by the results calculated by the member unit cross-sectional area, length, density and gravitational acceleration.

On-site Monitoring

Since displacement settlement observation is the most direct indicator reflects the situation of overall deformation (flexing) of the bridge, the most important indicator to determine whether the bridge is designed in an allowed error range and bearing system is changed. It was essential during the observation of construction. Before and after the bridge landing gear, 14 shift measuring points were arranged (measuring points shown in Fig. 3-1), measured multiple points by water level at different temperatures and time points.

After the bridge landing gear, it must be a definite problem that whether the forces of each component meet the design requirements during the landing gear monitoring. According to the existed engineering experience and experimental study, nine measuring points of stress monitoring were arranged in the corresponding rib^[8] (measuring point shown in Fig. 3-2).

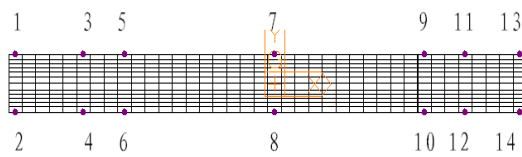


Fig. 1 Deflection Measuring Points

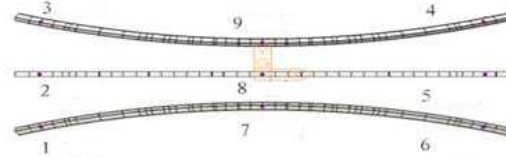


Fig. 2 Strain Measuring Points

Taking the temperature into account, the bridge settlement was observed four times after the landing gear. All the observations were happened in morning, noon and afternoon when the temperature changed greatly. Four settlement observations shown in Table 1 below (corresponding measuring point situation shown in Fig. 3-1):

Table 1 Comparison between Measured Values and Theoretical Value of Each Measuring Point

NO.	First (mm)	Second (mm)	Third (mm)	Fourth (mm)	Theoretical Value (mm)
1	-8	-14	-12	-12	0
2	-5	-7	-9	-9	0
3	-6	-10	-13	-13	-1.7
4	-6	-8	-10	-10	-1.7
5	-9	-10	-11	-11	-0.3
6	-7	-9	-10	-10	-0.3
7	-22	-21	-28	-29	-9.2
8	-35	-25	-29	-29	-9.2
9	-16	-9	-16	-18	-0.3
10	-16	-12	-18	-19	-0.3
11	-16	-12	-18	-16	-1.4
12	-14	-11	-19	-12	-1.4
13	-11	-12	-12	-14	0
14	13	16	12	15	0

In the table, the temperature of the bridge when first measured is 11°C, the second is 18 °C, the third is 23°C, the fourth is 21°C. Follows can be seen from the change of the measurement results in Table 1: (1)The change of four settlement observations are different. And there is a large difference between the first and the second settlement observation results and after the second (within the second) overall observation results stabilized. It is suggested that the bridge has basically entered into the steady state after the bridge landing gear while the former two significantly reduced settlement was largely resulted from the elongate of member caused by temperature change and the rib arch due to the fixed connection arch foot. (2) The largest settlement occurs at 7 and 8 measuring points (domes). The two measuring points have the largest observed values change (difference between the first and second settlement observation values). The biggest change reaches to 10mm, accounting for 40% of the total settlement. It indicates that for the higher statically indeterminate structure of steel girder and arch combination system, the settlement under temperature difference loads accounts for a large part. So it has been unavailable ignored that serious attention should be paid to the relevant structure in the future. (3) The 14th measuring point appeared an exception that beam bear separated and tilted from

abutments, timely treatment should be taken in order to ensure the safety and reasonable force of bridge structure.

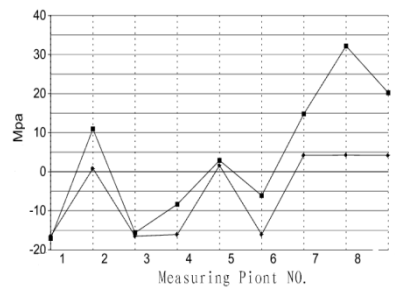
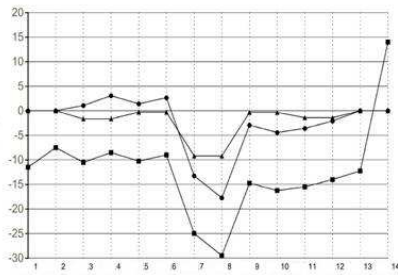


Fig. 3 Settlement Comparison between Theoretical and Measured Values **Fig. 4 Stress Comparison between Theoretical and Measured Values**

Fig. 3, the measured value of the four settlement observation average (used to offset the displacement caused by temperature stress settlement), remove the bearing sedimentation analysis model is assumed to remove restrictions bearing Z direction (the vertical direction) displacement error (intermediate points obtained using interpolation) . As can be seen from Fig. 3: (1) each point measured settlement values are larger than the theoretical value. The difference between the range of 10-15mm (except for abnormal tilt phenomenon measuring point 14) , the difference is relatively stable, indicating that the overall space linear bridge after settlement the basic design to achieve the desired goals, and fit and stability on the left side of the bridge is better than the right. (2) the settlement value of each measuring point was compared with the theoretical value adjustments, in addition to a larger displacement dome position difference, the other difference are within 5mm of further illustrate the displacement shown in Table 1 excessive sedimentation value change is caused by the change of the overall structure of the load by the temperature.

For stress testing, also to try to eliminate the influence of temperature changes, carried out a total of eight -day stress observation, eight stress observations and theoretical calculations in the following table (rib stress measuring point 2 cases shown in Fig. 2). Stress values observed in Table 2 are divided into eight time points, including day of sunshine different directions, all the data under different temperature conditions of stress arch.

Table 2 Weather Observations at Different Points of Stress Comparison with the Theoretical Value

NO	Observations at different times of stress (N/mm ²)								
	9:00	10:00	11:00	12:00	14:00	16:00	17:00	18:00	Theoretical
1	-13.56	-13.32	-14.04	-15.48	-18.93	-20.05	-22.78	-18.69	-16.5
2	28.07	26.07	24.3	14.2	4.65	-0.64	-5.45	-3.45	0.82
3	-12.67	-25.19	-15.08	-20.37	-18.85	-10.99	-11.55	-10.51	-16.5
4	-9.71	-10.35	-9.87	-9.79	-9.95	-5.86	-5.86	-5.53	-16.1
5	14.44	14.68	13.23	8.1	0.16	-7.38	-10.83	-9.46	1.6
6	-7.46	-6.9	-7.54	-4.97	-4.33	-6.1	-6.82	-4.97	-16.1
7	22.22	28.47	24.38	34.73	31.76	-6.26	-7.94	-8.98	4.19
8	26.55	35.61	29.84	47.89	50.13	22.46	23.98	21.02	4.26
9	22.54	25.51	23.5	29.28	27.91	11.95	11.47	9.46	4.19

From the measured stress values in Table 2 can be seen around the clock: (1) the distribution of stress at each measurement point rib larger changes before 16:00, in particular 12:00 to 16:00 between changes of considerable magnitude, the stress is relatively stable after the change, indicating that the bridge the main stress changes with temperature stress, when the temperature begins to rise and illumination direction changes, stress also will be dramatic changes, changes in the value reached its maximum 43.71MPa (position measuring point 7), far beyond its stress caused by the weight, so further explanation, such a steel girder arch higher temperature stress hyperstatic bridge can not be ignored. (2)Changes in Table 2 measurement points 1,3,4,6 (located on both sides of the arch of the foot arch rib) is relatively small, the basic state has been relatively constant, while the occurrence of

larger measuring point 2,5,7,8,9 changes. Where 2,5 is the arch of the foot arch rib two measuring points, the direct pressure from the state to the state of tension, indicating the direction under different conditions of sunlight, temperature difference on both sides of the bridge due to the presence of lateral generated bending of the phenomenon; three measuring points 7,8,9 measuring point location for the dome, which stresses the most obvious changes before 14:00 has been in a state of ever-increasing, then the temperature is reduced, but also drastically reduced, can Rib stress changes caused by temperature stress seen in the vault of the more obvious.

Fig. 2-2, the average value of the measured stress each measuring point eight measured stress values used to offset the effect of temperature changes on the bridge structural stress value change.

From the comparison graph of Fig. 2-2 with the theoretical value of the measured values can be seen: the measured value of the measuring points are consistent with the theoretical value, especially at the measuring point 1,3,5 (arch position) substantially the same as the theoretical value, indicating that the landing gear structure has basically enter the desired state, and measuring point 7, 8, 9 vault that position with the theoretical value larger difference in position by a factor of maximum Rib vault, the difference between the maximum of 27.9MPa, causing a large difference: on the one hand: the settlement measuring point 14 appears at the abutments and bearings from, inconsistent with the constraints of bridge structures and calculation models, to make a larger difference between the stress at the crown; partly because the theoretical model assumes that side sliding across its connection limit moves along the Z direction, thus limiting the development of the tensile stress Arch.

Conclusion

Based on the Mirage Bridge off the shelf space linear process bridge site with real-time monitoring of internal forces, and comparative analysis with the theoretical values obtained for Steel Beam Arch Composite Bridge this high statically indeterminate structure of the landing gear Some factors that play an important role in the process, as well as in the subsequent monitoring and construction should be noted that some of the issues: (1) For the steel girder and arch combination system of higher statically indeterminate structure, the displacement settlement arising under temperature stress and stress changes account for a large proportion (subsidence caused by temperature changes accounted for 40% of the total settlement, temperature stress reached 43.71MPa, 10 times its own stress), temperature stress value far exceeds the weight of stress itself has not be ignored. (2) Weather observations for monitoring values are the average sum process, can offset the displacement and stress settlement (settlement after treatment with the theoretical value of the temperature difference in the load caused by 5mm to some extent, the difference in stress 10MPa within), this method can be used in future monitoring. (3) During the construction process, the welding key parts of the bridge should be selected in the sunshine is not strong overall bridge when the temperature is relatively uniform, to prevent the bridge during the welding process due to uneven expansion and excessive bending stresses.

References

- [1] Jin Cheng-di: *Prestressed concrete beam arch combination bridge - Design Research and Practice*. Beijing: People's Communications Press, 2001.
- [2] Yu Shu-lan: Dalian University of Technology, 2003.
- [3] Rui Yong-sheng: *Construction*, 2009 (6): 490-491.
- [4] Sun Guo-chen, Guan Rong-cai, Jiang Ying-min, Mu Chun-lei, Huo Chun-yu, Xu Feng: *Engineering Mechanics*, 2006 (11): 122-127.
- [5] Peng Xing-cheng, Liu Xiao-jing, Guan Yi, Liu Wei-gang: *Highway Engineering*, 2008 (5): 40-44.
- [6] Dai Gong-lian, Li Jian-de. *Bridge structure spatial analysis and design and application*. Beijing: People's Communications Press, 2001.
- [7] Shi Ying: Zhejiang University of Technology, 2010 (10): 522-531.
- [8] Yi Yun Kun: *Bridge Construction*, 2008 (2): 34-37.

Construction Technique of Cast-in-situ RC Grillage Shear Wall Building Formed with Thermal Insulation Hollow Blocks

Weijing Zhang^{1, a}, Qian Zhang^{2, b}, Peiru Fu^{3, c}

^{1,2}College of Architecture and Civil Engineering, Beijing University of Technology, China, 100124

³ Beijing Daxing Hongguang Building Material Factory, China, 102600

^azhangweijing@bjut.edu.cn, ^bzhang_qian1989@sina.cn, ^cfushihongguang@vip.163.com

Keywords: lightweight insulation hollow block, grillage shear wall, construction technique

Abstract. The cast-in-situ reinforced concrete grillage shear wall system with non-dismantling formwork is a new type of structural system characterized by load-bearing and thermal insulation, and the research on the construction technique is crucial to its promotion and application. Combined with the pilot building, the key technology and construction measures are introduced in this paper, which can provide reference for the related projects in future.

Introduction

To meet the requirements of wall reform and building energy-saving, the cast-in-situ RC (reinforced concrete) grillage shear wall system (hereinafter referred to as ‘grillage shear wall system’) has been developed according to China's specifications and foreign cast-in-situ reinforced concrete wall systems with non-dismantling formwork. The grillage shear wall system integrates functions of structure, heat preservation, soundproofing and fireproofing, it is suitable for residential buildings in Chinese seismic and non-seismic areas.

The masonry block of grillage shear wall system is lightweight insulation hollow block which has good thermal insulation performance. The grillage shear wall system achieves the effect of heat insulation depends on the hollow blocks which has cavities. Reinforcing steel is placed in the cavities of the blocks and then concrete is poured into the cavities to form grid cast-in-situ RC shear wall (hereinafter referred to as ‘grillage shear wall’) as the core of grillage shear wall system, which is used for supporting vertical and horizontal force. The results of abundant experimental investigations indicate that the grillage shear wall has good seismic performance [1,2,3,4]. Shear or bending deformation of horizontal and vertical limbs consumes lots of seismic energy. The elastic-plastic deformation ability of grillage wall can meet the requirements of shear wall structure under strong earthquakes. The grillage wall can be applied to the residential buildings which are not greater than 24m.

As a key factor in application and promotion of the grillage shear wall system, construction technique is studied based on a single-story pilot building located in Beijing Daxing district. The building's plane shape is a rectangle with 5.16m in length and 5.06m in width. The building's story height is 2.8m and its floor area is 26.1m². The seismic precautionary intensity is 8 degree and the design working life is 50 years. Preparatory works, key points and attentions of construction are summarized from process of the construction in order to provide reference for the grillage shear wall system's promotion.

Lightweight Insulation Hollow Block

The lightweight insulation hollow block is made of expanded polystyrene granule cement light-weight concrete (hereinafter referred to as ‘EPS concrete’) which includes particle of polystyrene, cement, fly ash and adulterating agent. The principal properties are shown in table1. It has many good technical performances, including:

(1)The lightweight insulation hollow block has good thermal insulation performance and a certain degree of mechanical property. Density of the lightweight insulation hollow block is just 60%~70% of the density of small-sized concrete hollow block, so the weight of building can be reduced efficiently.

(2)The EPS concrete has good fire resistance, it belongs to grade A2 non-combustible material and meets the requirement of incombustible grade A building in terms of fire protection. To study the fire resistance performance, the grillage shear wall was fired at 2000°C for 2h at fire protection research laboratory of the ministry of public security in Tianjin, the result showed that there was no obvious damage on the surface and the blocks have good fire-resistance properties [5].

(3)As a kind of flexible material, the lightweight insulation hollow block can absorb some impact energy when it experiences plastic deformation. It plays an auxiliary role in seismic performance of grillage shear wall [6].

(4)The use of polystyrene can consume enormous amounts of industrial waste and save resources so as to reduce pollution. It is suitable for the policies of energy conservation and emission reduction.

Table 1 The principal properties of the lightweight insulation hollow block

No.	Term	Index value	No.	Term	Index value
1	density(kg/m ³)	≤380	5	heat storage coefficient [W/(m ² ·K)]	≥1.78
2	compressive strength(MPa)	≥0.5	6	natural water ratio (%)	≤5
3	flexural strength(MPa)	≥0.3	7	water absorption (%)	≤28
4	heat conductivity coefficient [W/(m ² ·K)]	≤0.083	8	softening coefficient	≥0.7

The lightweight insulation hollow block can be divided into interior wall block, exterior wall block and beam-column block following the 2M specifications. The block used for wall is hollow block with single hole and shallow groove, the size 395mm×195mm×(200mm+c) is for exterior wall and the size 395mm×195mm×280mm is for interior wall, c is the adjusted value which can change flexibly according to different heat preservation requirements in different regions. The size and photo of exterior wall block are shown in Figure 1. The beam-column block is single piece block without hollow and it can be cut from a whole EPS concrete board, its size can also change flexibly according to different design. Take two pieces of column blocks joint mutually perpendicular to form the framework of column. The sizes of beam-column blocks are shown in figure 2.

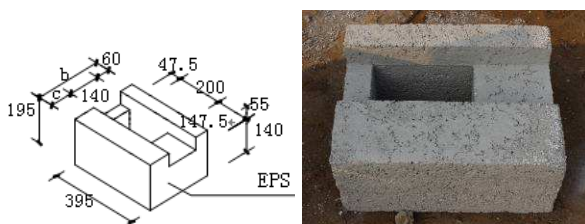


Fig.1 Size and photo of exterior wall block

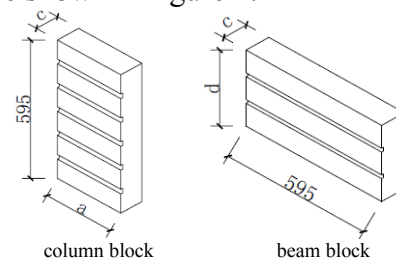


Fig.2 Sizes of beam-column blocks

Construction Preparation

To achieve the desired quality assurance, the construction phase has to be preceded by an elaborate and correct preparation stage.

(1) Hollow blocks should be transported into site with methodic order according to the schedule and they should not be dumped and thrown when they are loaded or unloaded. Ground for stacking hollow blocks should be tamped and easy to drain away water. The height of stockpile must not be more than 2m.

(2)The order of all blocks should be arranged according to the size and location of walls, openings, beams and volumes before construction.

(3)Vertical pre-embedded steel bar in foundation beams should be checked to make sure that the location of vertical steel bar is right and the length of vertical reinforcement above the top of foundation meets the related requirement.

(4)Surfaces of blocks should be cleaned and blocks which have breakage and distortion must not to be used.

Key Points of Construction

Foundation. Strip foundation is used for the pilot building. Process of the foundation's construction include: (1)cleaning and leveling the ground, (2)constructing and curing the concrete cushion layer, (3)layout, (4)colligating reinforcing steel of bottom plate and setting up formworks, (5)checking the qualities of reinforcing steel and formworks, (6)constructing and curing concrete of the foundation, (7) dismantling the formworks.

Vertical steel meshes in the grillage wall and longitudinal bars in the column are placed in the foundation beams prior to casting of the concrete. The length of vertical steel mesh above the top of foundation beam should meet the requirement for connecting. The longitudinal bars in column should be arranged in the whole range of the wall's height and the top must be extended into ring beam. For multi-storey grillage wall building, top of longitudinal bars in column must exceed the ring beam and the length over ring beam must meet the requirement.

Grillage Shear Wall. The construction of the grillage wall not only combines technology of traditional construction, but also has innovation.

(1)The upper surface of foundation beam must be cleaned before setting out with ink line according to the working drawing.

(2)The first row column blocks are constructed and it's necessary to make sure they are vertical. Then the first row wall blocks are constructed in line with reference line. The first row wall blocks have cleaned holes which used for cleaning the falling mortar and linking vertical steel mesh and embedded steel. The first row blocks with cleaned holes are shown in Figure 4(a). A piece of steel mesh is laid in layer of the horizontal groove, and then the second row blocks are constructed backward. The adjacent two rows blocks are built staggered through reverse hole aligning to make vertical cavities run through. The length between every two staggered joints is 100mm. Photo of the second row blocks' construction is shown in Figure 4(b).

(4)Non- integral blocks can be used at both ends of the wall, common size of them is 1/8 or 7/8 of whole block and they can be cut on site according to the requirement.

(5)Every two rows blocks are seen as a circulation. Every row blocks should be built orderly and it's necessary to ensure the wall's verticality by using the plumb line. Figure 4(c) shows the construction of several rows blocks.

(6)Blocks used for the uppermost row of the wall are upward in order to link the horizontal grooves and ring beams.

(7)The mortar filling degree is not less than 90%. 50mm wide mortar should be plastered on inside and outside edges of blocks; 60mm wide mortar should be plastered in vertical joints between two blocks. 4mm ~ 6mm is suitable for thickness of bed and vertical mortar joints. Mortar joints should be sufficient filling and compact in order to avoid leakage when the concrete is poured.

(8)The ring beam blocks are constructed above the uppermost row blocks of wall. Photo of blocks used for ring beam and the uppermost row of the wall is shown in Figure 4(d). The blocks used for ring beam have no hollow and they should be constructed at the outside, so it's necessary to build formworks at the inner side prior to placing.



(a)construct the first row blocks and lay the first piece of horizontal steel mesh



(b)construct the second row blocks



(c)construct upper row blocks



(d)construct the topside wall blocks and beam blocks

Fig.4 Construction of the grillage shear wall

Openings in the wall.

(1)The height of door openings should be the odd number times of the modulus M while the height of window opening should be the even number times of the modulus M .

(2)Straight troughs should be set at the opening in advance. Non-integral blocks whose sizes are $5/8$ and $7/8$ of the whole block are used for both sides of the opening, blocks which have frontal direction are used for bottom edge of the opening and blocks which have invert direction are used for top edge of the opening. Photos of door and window's openings are shown in Figure 5.

(3)Formworks of opening's upper side are built and it's necessary to make them straight and tight when blocks reach upper side of the opening.



(a)blocks used for door opening



(b)blocks used for window opening

Fig.5 Construction of the openings

Insert Steel Mesh into Vertical Cavities.

(1)Vertical steel meshes are inserted into vertical cavities after constructing every storey wall. Locations of vertical steel meshes should be in the middle of vertical cavities and parallel to the axes of walls. Photo of inserting vertical steel mesh is shown in Figure 6.

(2)The bottom of vertical steel meshes is combined with embedded reinforcement which placed in ground beam and the number of connective point should not be less than two. All vertical steel meshes should be tied with fine wire to ensure their verticality. Photo of fixing vertical steel meshes is shown in Figure 7.

(3)For single-story grillage wall building, top of vertical steel mesh should be intended into ring beam. For multi-story grillage wall building, top of vertical steel mesh should be taller than ring beam and the lapped length should meet the requirement.



Fig.6 Inset vertical steel mesh into cavity



Fig.7 Fix vertical steel meshes

Pour Concrete into Cavities. Some preparative works as follows should be completed before the concrete is poured into cavities.

(1) Little holes whose diameter is about 12mm~15mm are set up at one side of the wall in order to check the quality of concrete. One checked hole can be set every 2m².

(2) Mortar and sundries should be cleaned out from cleaned holes on the first row blocks, and then EPS concrete blocks are filled into the cleaned holes. Photo of EPS concrete blocks are filled into the cleaned holes is shown in Figure 8(a).

Concrete is poured into cavities to form grid cast-in-situ reinforced concrete shear wall which composed of vertical and horizontal limbs. Photo of pouring concrete is shown in Figure 8(b). The height of concrete once poured should not be more than 1m and the concrete should be vibrated in time. The result of acceptance for the exemplary building shows that the grillage shear walls filled with normal concrete have perfect quality. Self-compacting concrete which has better flow property can be used for pouring the grillage shear walls in order to save more labors.



(a) fill the cleaned holes



(b) pour concrete into cavities

Fig 8 Construction of pouring concrete

Roof or Floor Slab.

(1) 100mm thick hollow slab which prefabricated in factory is used for the pilot building. Waterproof layer is set after constructing 20 thick screed-coat.

(2) For single-story grillage shear wall building, either cast-in-situ or prefabricated concrete roof (floor) slab can be used. The cast-in-situ concrete roof (floor) slab should be poured along with ring beam in order to enhance the integrality of the structure [7].

Wall Plastering.

(1) Adhesion agent must be wiped onto walls uniformly before wall plastering.

(2) 6mm~8mm thick polymer mortar is plastered after plastering screed layer. 5mm~6mm thick polymer mortar is plastered first and then the alkali-resistant mesh fabric is tensed and pressed into mortar. The fabric should not be pressed too deep and it's advisable to see the outline of the fabric. 2mm~3mm thick polymer mortar is plastered secondly to use for calendaring and leveling.

(3) Door and window openings are wrapped by the 300mm wide polymer mortar paste glass fiber cloth. Polymer mortar is used for sticking the glass fiber cloth on the four corners of openings and the glass fiber cloth's specification is 100mm×400mm.

(4) 8mm~10mm thick hydrated lime putty is plastered on the inside surface of wall after leveling.

Construction Attentions.

There are some attentions of the construction as follows:

(1) Wall blocks should not be constructed until the mortar in column blocks masonry reaches the standard strength.

(2) The height of stacking hollow blocks is inappropriate to beyond 3.2m, and safety measures should be taken when the height is more than 3.2m.

(3) The reinforcing steel used for tied horizontal steel mesh should be wider than horizontal groove in order to avoid the horizontal steel mesh falling into groove. The end of horizontal steel mesh should be extended into column and connected with vertical steel in it, the number of the fastening buckles should not be less than 2.

(4) The observation holes should be plugged up before the concrete is poured in order to prevent splashing and spillage of concrete.

(5) Small-sized vibrating tube is used for vibrating concrete in some areas where reinforcing steel is intensive. The vibrating tube should be placed in right place first in order to prevent affecting the original locations of reinforcing steels.

(6) Before the ring beam is poured, sufficient time must be allowed between pours to let the underlying wall reach a minimum strength.

Conclusion

It is convenient and simple to construct the grillage shear wall system. As a kind of traditional construction technology, it does not need so many and large equipments; less formworks are used during the construction as the lightweight insulation hollow block act as formwork, and there is no need to set up the insulating layer as the lightweight insulation hollow block has good thermal insulation performance. All of the above characteristics result in less workstages and shorter construction period of the grillage shear wall system's construction.

Acknowledgements

Financial support from the National Key Technology Research and Development Program of the Ministry of Science and Technology of China through grant 2012BAJ03B04 is highly appreciated.

References

- [1] Jiaru Qian: Architecture Technology Vol.39-1 (2008) p.17, In Chinese
- [2] Yinan Du, Weijing Zhang and Baochun Feng: World Earthquake Engineering Vol.26-2 (2010) p.136, In Chinese
- [3] Weijing Zhang, Yinan Du and Hongzhen Kang: Journal of Building Structures Vol.32-5 (2011) p.116, In Chinese
- [4] Weijing Zhang, Yinan Du and Jiaru Qian: Advanced Materials Research Vol.446-449 (2012), p. 672
- [5] Lili Zhang, Jiayu Kan and Danlin Chen: Architecture Technology Vol.43-3 (2012) p.253, In Chinese
- [6] Baochun Feng: Architecture Technology Vol.39-1 (2008) p.8, In Chinese
- [7] CECS 338: 2013, China Planning Press, In Chinese

Damage Identification Based on Power Spectral Density Sensitivity Analysis of Structural Responses

W.H. Chen^{1, 2, a}, C.Y. Ding¹, B.Q. He¹, Z.R. Lu^{2, b}, and J.K. Liu²

¹Guangzhou Jishi Construction Group Co., Ltd., Guangzhou 510115, China

² Department of Applied Mechanics, Sun Yat-sen University, Guangzhou 510006, China

^achwh83@163.com, ^blvzhr@mail.sysu.edu.cn

Keywords: Damage identification, random vibration, pseudo excitation method, power spectral density, sensitivity analysis

Abstract. A new method is proposed to identify structural damages based on the power spectral density sensitivity analysis. The responses of the structure under stationary and random excitations are obtained using pseudo excitation method, and then the sensitivities of power spectral density with respect to the structural damage parameters are obtained similarly. Finite element model updating method is adopted to identify the structural damages. A numerical example of a shearing structure demonstrates the satisfactory results obtained from the present method.

Introduction

Structural damage detection using the dynamic characteristic parameters and dynamic responses has been a hot research topic in the past few decades. There are a lot of non-destructive methods in the literature for structural damage detection. Doebling et al. [1] provided a comprehensive review on the damage detection methods by examining changes in the dynamic properties of a structure.

Damage detection usually requires a mathematical model on the structure in conjunction with experimental modal parameters of the structure. The identification approaches are mainly based on the change in the natural frequencies [2], mode shapes [3] or measured modal flexibility [4].

There are also literatures on damage detection in time domain using structural dynamic response. Lu and Law [5] proposed a structural damage identification approach in time domain based on response sensitivity analysis.

In this paper, a new approach for structural damage identification based on the response power spectral density sensitivity analysis is proposed. The sensitivity of power spectral density with respect to the damage parameters and parameters of excitation are obtained under stationary, random excitation. Finite element model updating method is used in the identification. A numerical example of a shear structure demonstrates the satisfactory results obtained from the present method.

Pseudo-Excitation Method for Random Vibration Analysis

The pseudo-excitation method [6] is an efficient method for calculation dynamic responses of structures under random excitation forces. It is used extensively for vibration analysis of large civil engineering structure subjected to earthquakes and wind loads. In this paper, pseudo-excitation method is used to calculate the dynamic responses of structures under stationary random excitation force.

Structure Subjected to a Single-point Stationary Random Excitation

When a linear system is subjected to a single-point stationary random excitation $f(t)$ with auto-power spectrum $S_{ff}(\omega)$, the auto-power spectrum $S_{xx}(\omega)$ of the response is expressed as

$$S_{xx} = |H|^2 S_{ff} \quad (1)$$

where H is the frequency response function.

It is easy to see if the excitation $e^{i\omega t}$ is multiplied by a constant $\sqrt{S_{ff}}$ to construct a pseudo excitation, i.e. $\tilde{f}(t) = \sqrt{S_{ff}}e^{i\omega t}$, the response of the structure should be multiplied by the same constant

$$\tilde{x} = \sqrt{S_{ff}}He^{i\omega t} \quad (2)$$

From Eq (2), one has

$$\tilde{x}^* \tilde{x} = |\tilde{x}|^2 = |H|^2 S_{ff} = S_{xx} \quad (3)$$

where the superscript '*' denotes conjugation.

Structure Subjected to Multi-points Coherent Stationary Random Excitations

In the cases when structures are subjected to multi-points coherent stationary random excitation, such as earthquake excitation, random wind load, these can be regarded as the generalized problem of single-point excitation. It can be easily solved following the above method. In frequency domain, a traditional equation for calculating the stationary response of linear system is expressed as

$$S_{xx} = H^* S_{ff} H^T \quad (4)$$

where S_{ff} is the spectral matrix for known excitation force, H is the transfer function matrix, S_{xx} is the response spectral matrix to be solved, the superscripts '*' and 'T' denote conjugation and transpose of a matrix.

The spectral matrix S_{ff} can be decomposed as

$$S_{ff} = a^* a^T S_0 \quad (5)$$

Once the pseudo harmonic excitation is constructed as

$$\tilde{f} = a e^{i\omega t} \sqrt{S_0} \quad (6)$$

The harmonic response of the system can be expressed as

$$x = b e^{i\omega t} \quad (7)$$

where $b = Ha\sqrt{S_0}$. The response spectral matrix S_{xx} can be written as

$$S_{xx} = x^* x^T = b^* b^T \quad (8)$$

Damage Identification Based on Power Spectral Density Sensitivity Analysis

Equation of motion of forced vibration for multiple degree-of-freedom system is expressed

$$M\ddot{x} + C\dot{x} + Kx = F(t) \quad (9)$$

where M , K and C are system mass, stiffness and damping matrices, respectively. In this paper, Rayleigh damping is adopted, i.e.

$$C = a_1 M + a_2 K \quad (10)$$

where a_1 and a_2 are two constants, and they are determined from two different modal frequencies

$$\omega_i, \omega_j \text{ and modal damping ratios } \xi_i, \xi_j, \text{ i.e., } a_1 = \frac{2\omega_j\omega_i(\omega_j\xi_i - \omega_i\xi_j)}{\omega_j^2 - \omega_i^2}, a_2 = \frac{2(\omega_j\xi_j - \omega_i\xi_i)}{\omega_j^2 - \omega_i^2}.$$

Sensitivity of Power Spectral Density with Respect to Damage Parameters

It is assumed that the structure is subjected to a stationary random excitation and it can be decomposed as shown in Eq (5). Applying the pseudo excitation $\tilde{f} = a e^{i\omega t} \sqrt{S_0}$ onto the structure, Eq. (9) can be expressed as

$$M\ddot{x} + C\dot{x} + Kx = \tilde{f} \quad (11)$$

The displacement, velocity and acceleration responses of the structures are written as

$$x = H a e^{i\omega t} \sqrt{S_0} \quad (12)$$

$$\dot{x} = i\omega H a e^{i\omega t} \sqrt{S_0} \quad (13)$$

$$\ddot{x} = -\omega^2 H a e^{i\omega t} \sqrt{S_0} \quad (14)$$

Differentiating on both sides of Eq (11) with respect to the i th damage parameter α^i , we have:

$$M \frac{\partial \ddot{x}}{\partial \alpha^i} + C \frac{\partial \dot{x}}{\partial \alpha^i} + K \frac{\partial x}{\partial \alpha^i} = -\frac{\partial K}{\partial \alpha^i} x - a_2 \frac{\partial K}{\partial \alpha^i} \dot{x} \quad (15)$$

where $i=1,2,\dots,n$, n total element number in the finite element model, the damage parameter α^i can be taken as the Young's modulus of the i th element or other physical parameters associated with the elemental stiffness, $\frac{\partial x}{\partial \alpha^i}$, $\frac{\partial \dot{x}}{\partial \alpha^i}$, $\frac{\partial \ddot{x}}{\partial \alpha^i}$ are the displacement response sensitivity with respect to i th damage parameters, velocity response sensitivity with respect to i th damage parameters and acceleration response sensitivity with respect to i th damage parameters, respectively. Noted that the right hand side of Eq (15) can be expressed as the form of harmonic excitation

$$-\frac{\partial K}{\partial \alpha^i} x - a_2 \frac{\partial K}{\partial \alpha^i} \dot{x} = \left(\frac{\partial K}{\partial \alpha^i} - i\omega a_2 \frac{\partial K}{\partial \alpha^i} \right) H a \sqrt{S_0} e^{i\omega t} \quad (16)$$

The response sensitivities $\frac{\partial x}{\partial \alpha^i}$, $\frac{\partial \dot{x}}{\partial \alpha^i}$, $\frac{\partial \ddot{x}}{\partial \alpha^i}$ in Eq (15) can be calculated similar to the calculation of the dynamic response.

Eqs (12), (13) and (14) can be re-written as

$$x = (c + d)e^{i\omega t} \quad (17)$$

$$\dot{x} = i\omega(c + d)e^{i\omega t} \quad (18)$$

$$\ddot{x} = -\omega^2(c + d)e^{i\omega t} \quad (19)$$

The sensitivity of dynamic response with respect to the damage parameter can be expressed as

$$\frac{\partial x}{\partial \alpha^i} = \left(\frac{\partial c}{\partial \alpha^i} + \frac{\partial d}{\partial \alpha^i} \right) e^{i\omega t} \quad (20)$$

$$\frac{\partial \dot{x}}{\partial \alpha^i} = i\omega \left(\frac{\partial c}{\partial \alpha^i} + \frac{\partial d}{\partial \alpha^i} \right) e^{i\omega t} \quad (21)$$

$$\frac{\partial \ddot{x}}{\partial \alpha^i} = -\omega^2 \left(\frac{\partial c}{\partial \alpha^i} + \frac{\partial d}{\partial \alpha^i} \right) e^{i\omega t} \quad (22)$$

The power spectral density of the structural response can be written as

$$S_{xx} = x^* x^T = c^2 + d^2 \quad (23)$$

$$S_{\dot{x}\dot{x}} = \dot{x}^* \dot{x}^T = i\omega(c^2 + d^2) \quad (24)$$

$$S_{\ddot{x}\ddot{x}} = \ddot{x}^* \ddot{x}^T = -\omega^2(c^2 + d^2) \quad (25)$$

The sensitivity of power spectral density with respect to the damage parameter can be expressed as

$$\frac{\partial S_{xx}}{\partial \alpha^i} = \left(\frac{\partial c^2}{\partial \alpha^i} + \frac{\partial d^2}{\partial \alpha^i} \right) = 2 \left(\frac{c\partial c}{\partial \alpha^i} + \frac{d\partial d}{\partial \alpha^i} \right) \quad (26)$$

$$\frac{\partial S_{\dot{x}\dot{x}}}{\partial \alpha^i} = i\omega \left(\frac{\partial c^2}{\partial \alpha^i} + \frac{\partial d^2}{\partial \alpha^i} \right) = 2i\omega \left(\frac{c\partial c}{\partial \alpha^i} + \frac{d\partial d}{\partial \alpha^i} \right) \quad (27)$$

$$\frac{\partial S_{\ddot{x}\ddot{x}}}{\partial \alpha^i} = -\omega^2 \left(\frac{\partial c^2}{\partial \alpha^i} + \frac{\partial d^2}{\partial \alpha^i} \right) = -2\omega^2 \left(\frac{c\partial c}{\partial \alpha^i} + \frac{d\partial d}{\partial \alpha^i} \right) \quad (28)$$

Damage Identification

In the inverse problem, response power spectral density based finite element model updating method is used to identify the structural damages, The identification problem can be expressed as: to find the damage parameters α^i , such that the calculated power spectral density can best match the measured one, i.e.,

$$QR_{cal} = \hat{R} \quad (29)$$

where the selection matrix $[Q]$ is a matrix with elements of zeros or ones. R_{cal} is the calculated response power spectral density, and \hat{R} is the measured one. In this paper, the power spectral density of acceleration response is used in the damage detection.

The equation for damage identification can be expressed as

$$\delta \mathbf{R} = \mathbf{S}_\alpha \delta \boldsymbol{\alpha} \quad (30)$$

where, $\delta \mathbf{R} = \delta(\hat{\mathbf{R}} - \mathbf{R}_{cal})$ is the difference between the measured response power spectral density and the calculated one, \mathbf{S}_α is the sensitivity matrix of the response power spectral density, for a given frequency ω_i , it is written as:

$$\mathbf{S}_{\omega=\omega_i} = \begin{bmatrix} \frac{\partial S_{\ddot{x}\ddot{x}1}(\omega_i)}{\partial \alpha^1} & \frac{\partial S_{\ddot{x}\ddot{x}1}(\omega_i)}{\partial \alpha^2} & \dots & \frac{\partial S_{\ddot{x}\ddot{x}1}(\omega_i)}{\partial \alpha^i} & \dots & \frac{\partial S_{\ddot{x}\ddot{x}1}(\omega_i)}{\partial \alpha^n} \\ \frac{\partial S_{\ddot{x}\ddot{x}2}(\omega_i)}{\partial \alpha^1} & \frac{\partial S_{\ddot{x}\ddot{x}2}(\omega_i)}{\partial \alpha^2} & \dots & \frac{\partial S_{\ddot{x}\ddot{x}2}(\omega_i)}{\partial \alpha^i} & \dots & \frac{\partial S_{\ddot{x}\ddot{x}2}(\omega_i)}{\partial \alpha^n} \\ \vdots & \vdots & \dots & \vdots & \dots & \vdots \\ \frac{\partial S_{\ddot{x}\ddot{x}i}(\omega_i)}{\partial \alpha^1} & \frac{\partial S_{\ddot{x}\ddot{x}i}(\omega_i)}{\partial \alpha^2} & \dots & \frac{\partial S_{\ddot{x}\ddot{x}i}(\omega_i)}{\partial \alpha^i} & \dots & \frac{\partial S_{\ddot{x}\ddot{x}i}(\omega_i)}{\partial \alpha^n} \\ \vdots & \vdots & \dots & \vdots & \dots & \vdots \\ \frac{\partial S_{\ddot{x}\ddot{x}n}(\omega_i)}{\partial \alpha^1} & \frac{\partial S_{\ddot{x}\ddot{x}n}(\omega_i)}{\partial \alpha^2} & \dots & \frac{\partial S_{\ddot{x}\ddot{x}n}(\omega_i)}{\partial \alpha^i} & \dots & \frac{\partial S_{\ddot{x}\ddot{x}n}(\omega_i)}{\partial \alpha^n} \end{bmatrix} \quad (31)$$

The increment of damage parameter vector $\delta \boldsymbol{\alpha}$ can be obtained from least-squares method directly

$$\delta \boldsymbol{\alpha} = \mathbf{S}_\alpha^T \mathbf{S}_\alpha^{-1} \mathbf{S}_\alpha^T \delta \mathbf{R} \quad (32)$$

Like many other inverse problems, Eq (30) is an ill-conditioned problem. In order to provide bounds to the solution, the damped least-squares method (DLS) (Tikhonov1963) is used and singular-value decomposition is used in the pseudo-inverse calculation. Equation (30) can be written in the following form in the DLS method:

$$\delta \boldsymbol{\alpha} = (\mathbf{S}_\alpha^T \mathbf{S}_\alpha + \lambda \mathbf{I})^{-1} \mathbf{S}_\alpha^T \delta \mathbf{R} \quad (33)$$

where λ is the non-negative damping coefficient governing the participation of least-squares error in the solution. L-curve method (Hansen1992) is used in this paper to obtain the optimal regularization parameter λ .

The updated damage parameter vector is

$$\boldsymbol{\alpha} = \boldsymbol{\alpha}_0 + \delta \boldsymbol{\alpha} \quad (34)$$

where $\boldsymbol{\alpha}_0$ is the initial vector of damage parameter.

Algorithm for Damage Identification

The damage identification can be accomplished from following steps:

Step 1: the power spectral density of structural response can be obtained from Eq (25) for the intact structure, and the sensitivities of response power spectral density with respect to damage parameter are obtained from Eq (28), then the sensitivity matrix \mathbf{S}_α is constructed.

Step 2: The difference between the measured response power spectral density and the calculated one $\delta \mathbf{R}$ is obtained from Eq(29);

Step 3: The increment of damage parameter vector $\delta \boldsymbol{\alpha}$ is calculated from Eq(33), and the updated damage parameter $\boldsymbol{\alpha}$ is obtained from Eq(34);

Step 4: Repeated from Step 1 to Step 3, until when the criteria $\left\| \frac{\{\alpha_{k+1}\} - \{\alpha_k\}}{\{\alpha_{k+1}\}} \right\| \leq tolerance$ is met.

Numerical Simulation

A shearing structure model with 15 degrees-of-freedom is studied, the mass for each floor is $2 \times 10^4 \text{ kg}$, and the shearing rigidity is $3.23 \times 10^4 \text{ kN/m}$, the first two damping ratios is taken as 0.02. Local damage in the structure is modeled as the reduction in the shearing rigidities of some floors. The structure is subjected to stationary acceleration earthquake excitation from the ground, the excitation spectrum is assumed to be filtered spectrum of white noise, and the self-power spectrum is expressed

as $S_{\dot{x}_g} = \frac{\omega_g^4 + 4\zeta_g^2 \omega_g^2 \omega^2}{(\omega_g^2 - \omega^2)^2 + 4\zeta_g^2 \omega_g^2 \omega^2} S_0$. The parameters for the soil are taken as $\omega_g = 15.708s^{-1}$, $\zeta_g = 0.6$, $S_0 = 0.001574m^2s^{-3}$.

In this paper, we make use of the power spectral density of the acceleration responses at the 1st mass, 7th mass, and 15th mass to conduct damage identification. The frequencies below 5 Hz in the spectrum are used in the identification and the resolution for the frequencies is 0.02 Hz. Totally, there are 100 equations in the damage identification, the number of unknown is 15, so the identification equation is over-determined. The tolerance for converge is taken as 10^{-8} .

Identification of Single Damage

In the simulation, it is assumed that there is a 20% reduction in the stiffness of 10th element. The local damage has been identified successfully after 11 iterations as shown in Figure 2. The max identification error is 1.1% at 14th element. This study case shows that the proposed method is effective for single damage identification. The optimal regularization parameter is found to be 2.34×10^{-5} .

Identification of Multiple Damages

In this case, three local damages in elements 4, 10 and 11 with 10%, 20% and 15% reduction in each stiffness, respectively. Three local damages have been identified with good accuracy after 14 iterations as shown in Figure 3. The max identification error is 1.1% at 12th element. The optimal regularization parameter is found to be 7.39×10^{-5} .

Conclusions

In this paper, an algorithm is proposed for structural damage identification based on sensitivity analysis of power spectral density. Numerical simulation shows that the proposed method is effective for both single and multiple damage identification. The power spectral density of acceleration responses from few measurement points are needed in the identification. The measurement noise effect on the identification result should be further studied.

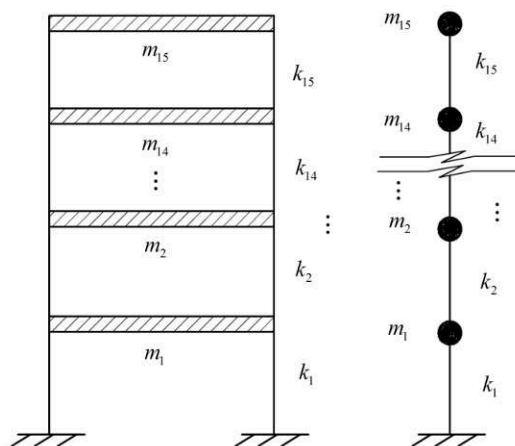


Fig. 1 A shearing structure model

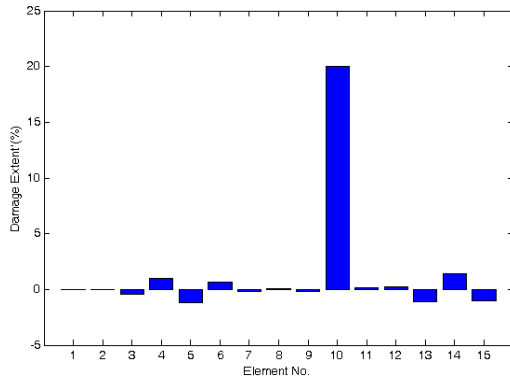


Fig. 2 Identification of a single damage

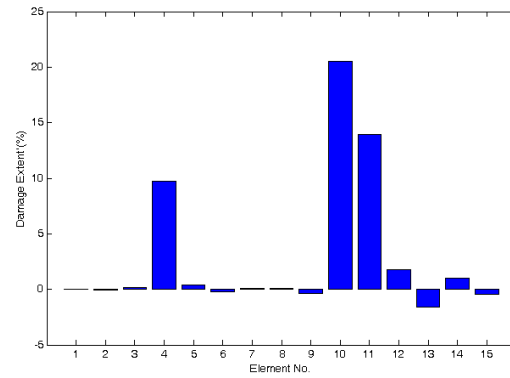


Fig. 3 Identification of multiple damages (noise free)

Acknowledgments

This work is supported by the National Natural Science Foundation of China (11272361, 11172333), Doctoral Program Foundation of Ministry of Education of China (20130171110039), the Guangdong Province Science and Technology Program (2012A030200011), the Fundamental Research Funds for the Central Universities (13lgzd06), the General Financial Grant from the China Postdoctoral Science Foundation (2013M531893), and the Yuexiu District Science and Technology Program (2013-GX-002). Such financial aids are gratefully acknowledged.

References

- [1] S.W. Deobling et al.: *Shock Vibration Digest*, Vol. 30 (1998), p 91.
- [2] P. Cawley and R.D. Adams: *Journal of Strain Analysis*, Vol. 14 (1979), p 49.
- [3] A. K. Pandey, M. Biswas and M. M. Samman: *Journal of Sound and Vibration*, Vol. 145 (1991), p 321.
- [4] A. K. Pandey and M. Biswas: *Journal of Sound and Vibration*, Vol. 169 (1994), p 3.
- [5] Z.R. Lu and S. S. Law: *Journal of Sound and Vibration*, Vol. 303 (2007), p 305.
- [6] J. H. Lin and, Y. H. Zhang: *Pseudo-excitation method for random vibration* (Science Press, Beijing 2002). (in Chinese)
- [7] A. M. Tikhonov: *Soviet Mathematics*, Vol. 4(1963), p 1035.
- [8] P. C. Hansen: *SIAM Review*, Vol. 34 (1992), p 561.

Damage location identification of truss structure based on strain modal method

Beidou Ding^{1, 2, a}, Ming Tan^{1, 2}, Yanan Shang^{1, 2}

¹ School of Architecture & Civil Engineering, China University of Mining and Technology

² Jiangsu Key Laboratory of Environmental Impact and structural safety in Engineering Jiangsu Xuzhou, China)

^adbdstar@163.com

Keywords: truss structure; strain modal; damage identification; sensitivity analysis;

Abstract: Due to the fatigue load and bad corrosion environment, truss structure in service will form the damage accumulation, damage detection of potentially damaged elements of truss structures is a challenging topic. According to the element stress characteristics of truss structure, structural element strain mode mainly based on the vibration displacement is derived, the change of elemental strain modal is proposed as the dynamic indicator for damage location identification of truss structure. Based on the numerical simulation study of the actual truss structure indicates that, the low-order elemental strain modal method is not only sensitive to damage identification of chord element and web element of truss structure, but also is effective to locate the damage of different position, and is suitable for damage alarming of truss structure in service.

Introduction

Truss structures are widely used in industrial and civil building such as long-span truss bridge, stadiums, the roof of gas station, gymnasiums and exhibition halls. Truss structures continually accumulate damage during their service life such as winds, earthquakes, corrosion, and also accidental damage sources including impacts, explosions and fire disaster. To ensure their healthy operational condition and safe status, early damage detection and location are crucial to avoid the possible occurrence of a catastrophic structural failure.

Since the accumulative damage may cause damage in changes in the physical properties of the structure will, in turn, alter the dynamic characteristics of the structure, such as natural frequency, modal damping, and mode shape. [1–2] Hence, changes in these parameters or in their combinations may be considered for localization and quantification, which are important components of damage detection [3–5].

According to the member element mechanical characteristics of truss structure, the member element strain can be acquired by the node displacements of the member, a damage identification method for truss structure based on change of the low-order strain modal is proposed. A damage index obtained by solving the perturbation equation is used for damage location. Numerical analysis of a truss structure including damage location for different single-member and multi-member damage cases to verify the effectiveness of proposed damage location identification method. At the same time, the recognition performance robustness was investigated, which is based on strain modal method under different noise levels. [6–9]

Damage location identification method based on element strain modal method

According to the relationship between node displacement and element strain, each element strain distribution has corresponding displacement mode, which is called strain mode [7]. If the structure is damaged, the element strain in damaged location emerges obvious peak due to the structural rigidity reduction. Therefore, it is possible to determine the potential damage location by comparing with absolute value of the element strain modal difference between undamaged structure and damaged structure of the truss structure, in which the peak of strain modal difference is evident.

The derivation of basic theory of structural damage location identification based on element strain modal difference is followed. In general, the relation of strain response of structure and strain mode can be written as:

$$\varepsilon = \sum_{r=1}^m q_r \psi_r^{\varepsilon} \quad (1)$$

Where, q_r is the r th modal coordinate, denotes that r th displacement modal contribution to the displacement response, ψ_r^{ε} is the r th strain modal, m is the number of mode shapes identified;

The low order modal displacement has more contribution to the total displacement response than high order displacement modal, in fact, the first order vertical displacement modal has a large proportion contribution to the whole displacement response.

While the r th element strain modal of grid structure can be calculated from the modal displacement of each member node, its expression is as follows:

$$\psi_r^{\varepsilon} = \left[(u_j - u_i)(x_j - x_i) + (v_j - v_i)(y_j - y_i) + (w_j - w_i)(z_j - z_i) \right] / L^2 \quad (2)$$

Where, $u_i, v_i, w_i, u_j, v_j, w_j$ is the r th modal displacement of number i node and number j node of element ij and $x_i, y_i, z_i, x_j, y_j, z_j$ is the node displacement of number i node and number j node of element ij in global coordinate system respectively;

Therefore, the structural damage strain mode difference between undamaged structure and damaged structure can be expressed as:

$$\Delta \varepsilon = \varepsilon_d - \varepsilon_u = \sum_{r=1}^m q_r \psi_r^{\varepsilon d} - \sum_{r=1}^m q_r \psi_r^{\varepsilon u} \quad (3)$$

In Eq.3, $\varepsilon_d, \varepsilon_u$ is the strain response of damaged and undamaged structure respectively. Considered that it is difficult to obtain the r th modal coordinate, and the different order strain modes are orthogonal, and relative to the strain response are more available, therefore, the use of one order strain mode difference can identify structural damage, and the damage indicator is defined as:

$$\Delta \psi_r^{\varepsilon} = \left| \psi_r^{\varepsilon d} - \psi_r^{\varepsilon u} \right| \quad (4)$$

$$\Delta \psi_r^{\varepsilon}(k) = \left| \psi_r^{\varepsilon d}(k) - \psi_r^{\varepsilon u}(k) \right| \quad (k = 1, 2, \dots, N) \quad (5)$$

In Eq.4, the indicator $\Delta \psi_r^{\varepsilon}$ is r th strain modal difference matrix; $\psi_r^{\varepsilon d}, \psi_r^{\varepsilon u}$ is r th strain modal matrix of damaged structure and undamaged structure, respectively; $\psi_r^{\varepsilon d}(k), \psi_r^{\varepsilon u}(k)$ is the r th strain modal value before and after k element damaged, respectively, N is the total number of members of truss structure. From Eq.5, it is concluded that, if a single-member is damaged, the most possible damaged member element is located in the region in which the value of the r th strain modal $\Delta \psi_r^{\varepsilon}(k)$ is max, if several member are damaged at the same time, then there must be several relatively significant changes of the $\Delta \psi_r^{\varepsilon}(k)$ values in which the local damage locations are.

Numerical studies on damage location identification in truss structures

To verify the foregoing damage method, a 5×5 bay truss structure that consists of 200 steel tubular members with a square side length of 2.5 m and a height of 0.5 m was numerically analyzed. This structure is shown in Fig. 1. The members were assumed to be axial tension-compression members that were pin-ended and pin-braced against the supports in the ground, and all the members had similar tube cross-sections measuring 48 mm \times 3.25 mm. The material properties of the steel tubular members include elastic modulus $E = 210$ GPa, poisson's ratio $\nu = 0.3$, mass density $\rho = 7850$ kg/m³, and yield strength = 235 MPa. Loading was applied to the intermediate point of the top chord. The design parameters of the test truss structure are listed in Table 1.

Table 1 Design parameters of a test truss structure

Plane Size	2.5 m × 2.5 m	Number of bay	5 × 5
Height	0.5 m	Support type	pinned
member dimension	48 mm × 3.25 mm	Bolt ball diameter	100

The ANSYS finite element analysis software is used to numerical modeling and structural analysis, the truss member are simulated with two node linear LINK8 element which are assumed to be axial tension-compression members. In the modal analysis of truss structure, the lumped mass method is adopted to construct the mass matrix, damping effect is neglected, and it is assumed that structural mass damage is not changed due to member damage.

For convenience, the nodes and member numbers of numerical model, which are generated by using the parameter programming language (APDL) technology of ANSYS procedure are shown in Fig.1, in which webs are marked with pale yellow and chords are black.

Damage cases of truss structure

The damage cases of truss structure are stimulated by member elastic modulus reduction, which would change the stiffness of the structure to realize the simulation of damage scenarios. The member damage severity can be expressed as:

$$\alpha = \frac{(E_u - E_d)}{E_u} \quad (6)$$

Where, α denotes the member damage severity, E_u is the elastic modulus of undamaged member, E_d is the elastic modulus of damaged member,

It is possible to be damaged members for all members of truss structure, including the top, bottom chord and web member damage scenarios in which single-member or multi-member are stimulated to be damaged.

In actual stimulation, 11 damage cases are simulated by use of the selected five members, which include the two top chord member (No. 39, 45), two bottom chord member (No. 13, 21) and an web member (No. 112), as shown in Fig. 1 to execute the damage location identification and the damage extent identification of truss structure. The element damage cases of truss structure is shown in Table 1 and Table 2. The stimulation of C damage severity of full member damage case in Table 3 is stimulated to remove the corresponding number member in the finite element simulation.

Damage detection in truss structures based on element strain modal method

Firstly, 8 kinds of damage cases of truss structure are stimulated through the finite element modal analysis technology, then each absolute value of the element strain modal difference are compared between damage cases and undamaged structure, respectively. The results are plotted in the same graph to visually determine the damage location of damaged element, the damage location identification graphs are shown in Fig. 2.

The results show that the damaged location of those members can be accurately identified, which absolute value peak of first-order element strain modal difference are prominent, that is, the top chord of member 39 in case 1, the bottom chord of member 13 in case 2 and the top chord of member 39 and bottom chord of member 13 in case 5. While there are several undamaged members in case 3,4,6,7 and 8, which absolute value peak of first-order element strain modal difference are prominent, then the range of possible damage identification will be expanded.

So, the possible damage range can be defined based on first order element strain mode difference method, but, the accurate damaged members need to be further examined. Considering the possibilities of wrong damage location identification based on first-order element strain difference method, some scholars put forward to increase the low order such as two order element strain modal difference method for further damage identification.

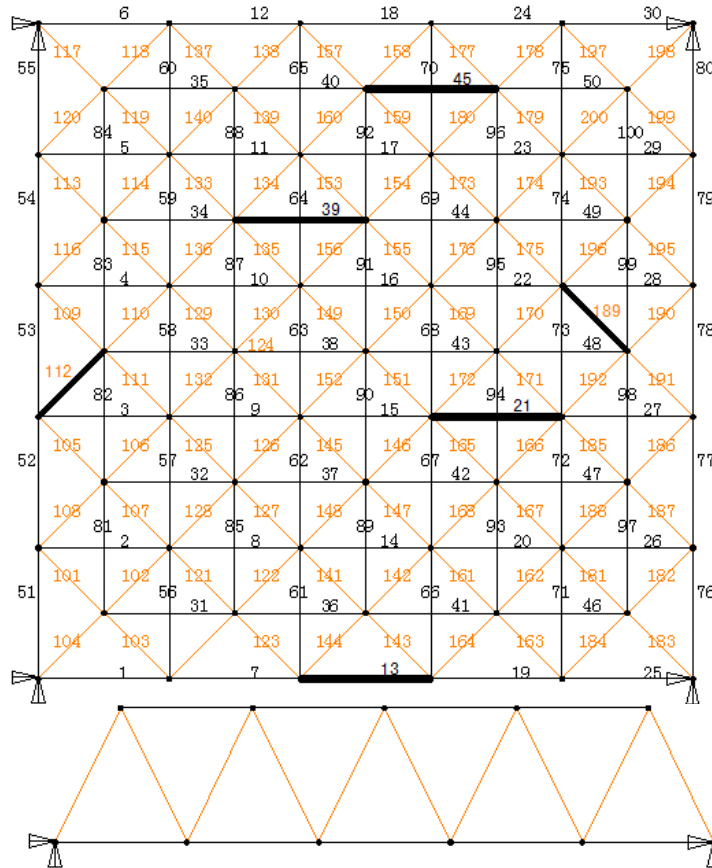


Fig.1 Mark Of the stimulated damaged element number of the truss structure

Table 2 Cases of damage element location of truss structure

Case Number	Member type	Member Number	Damage severity	Damage type
1	Top member	39	1/3	Single damage
2	Bottom member	13	1/3	Single damage
3	web	112	1/3	Single damage
4	web	112	1/3	Double damage
5	Top member	39	1/3	Double damage
6	Bottom member	13	1/3	Double damage
7	Top member	39	1/3	Double damage
	Top member	45	1/3	Double damage
8	Bottom member	13	1/3	Double damage
	Bottom member	21	1/3	Double damage

Table 3 Cases of the element damage severity of truss structure

Case Number	Member type	Member Number	Damage severity			Damage type
			A	B	C	
9	Top member	39	1/3	2/3	3/3	Single damage
10	Bottom member	13	1/3	2/3	3/3	Single damage
11	Top member	39	1/3	2/3	3/3	Double damage
	Bottom member	13	1/3	2/3	3/3	

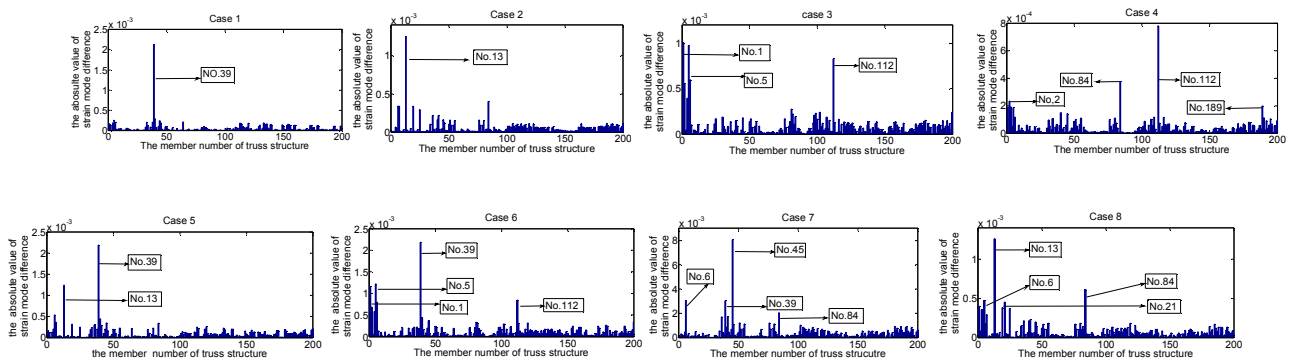


Fig.2 Absolute difference of the 1st strain mode before and after the multi-element damage of the truss structure

In order to study the relation of sensitivity analysis between the member damage degree and changes of absolute value of modal strain difference, the absolute results of 200 member element strain modal difference in A, B, C damage degree situation from case 9 to case 11, are shown in Fig. 3-5, respectively. From Fig. 3, it can be found that the absolute strain modal value of top chord member 39 has outstanding peak in A, B, C damage severity situation, the absolute values of first order strain mode difference are significantly higher than the corresponding values of undamaged members in truss structure, so the potential damaged member locations can be identified accurately. With the increase of the member damage severity, strain modal difference magnitude has changed, it can be found that when the member damage proportion from 1/3 to 2/3, the strain modal difference magnitude of 10⁻³ level do not change obviously, however, when the member damage proportion exceeding than 2/3, the strain modal difference magnitude level is changed from the 10⁻³ to 10⁻² level. It can be concluded that the first order strain mode has higher sensitivity in the member single damage identification cases. Other single-member and multi-member damage identification results are shown in Fig. 4, 5, it can be concluded that those stimulated damaged members have the similar corresponding results compared with the top chord 39. In particular, from the absolute results of element strain modal difference of bottom chord member 13 and top chord member 39 which are damaged at the same time in A, B, C damage degree situation in case 11, shown in Figure 5, it can be concluded that the multi-member damage sensitivities of the several members have the same damage sensitivity when those damaged members are damaged respectively in single-member damage cases.

In summary, there are a consistent relationship between the distribution of absolute value of element strain modal difference and member damage location in truss structure, such principle can be used to accurately identify the single-member or multi-member failure damage location. Because the absolute value of element strain modal difference changed with the different damage severity of the member in the same place.

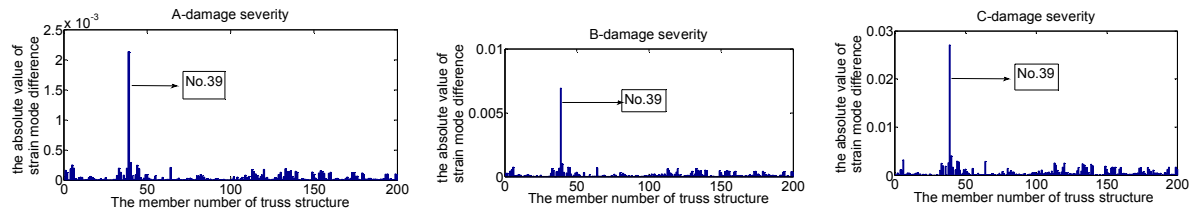


Fig.3 Absolute difference of the grid first-order strain mode under case 9

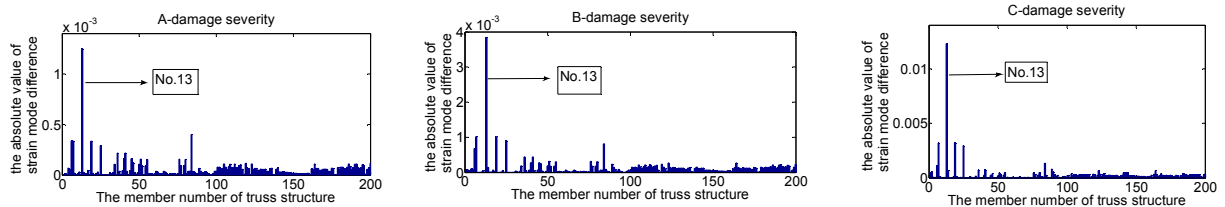


Fig.4 Absolute difference of the grid first-order strain mode under case 10

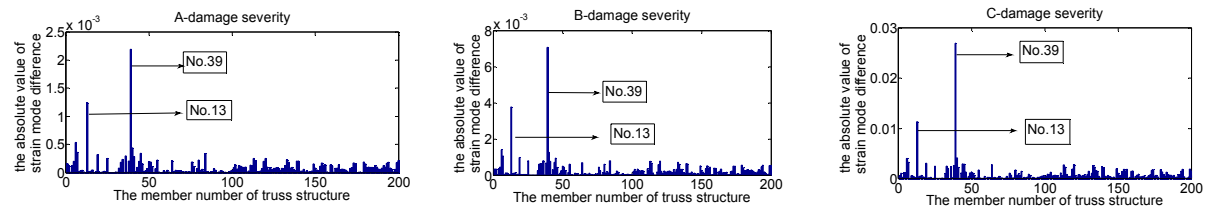


Fig.5 Absolute difference of the grid first-order strain mode under case 11

Conclusions

A method for damage location of truss structure based on element strain modal difference is proposed, in which the corresponding element strain mode from the mode displacement is calculated according to the mechanical characteristics of truss structure and the absolute value of the element strain modal difference are defined as damage location indicator. Research on the numerical simulation of a typical truss structure, verify the validity of the damage location method, the main conclusions drawn are as follows:

(1) The strain mode are sensitive to member damage of the truss structure, but there are still a possibility of miscarriage of justice, in general, the first order strain mode can identify the damage position of member, could define the scope of possible damage members.

(2) With the increase of the degree of damage severity, the absolute value of the first order element strain mode difference emerges peak gradient and the recognition effect is well. It was shown that the absolute value of first order strain mode difference is more sensitive to the damage extent of truss structure.

(3) Because the absolute value of element strain modal difference changes with the different damage severity of the member in the same place, the member damage severity can be calculated according to the relative chagement of absolute value of element strain modal difference to quantify damage severity.

Acknowledgements

This research was supported by the National Natural Science Foundation of Jiangsu Province (BK2011221), and the open fund project of Jiangsu Key Laboratory of Environmental Impact and structural safety in Engineering (JSKL2012YB09), which the writers gratefully acknowledge.

References

- [1] Salawu O .S. Detection of Structural Damage through Changes in Frequency [J]. *A Review Engineering Structures*, 1997, Vol.19 (9):718-723
- [2] Fabricio Vesvroni, Davila CaPe chi. Damage Detection in Structures Based on Frequently Measurements [J]. *Journal of Engineering Mechanics. ASCE*, 2000, Vo1.126 (7): 761-768.
- [3] Doebling S.W, Farrar C.R, Prime M.B, Shevitz D.W. A summary review of damage identification methods that examine changes in dynamic properties. *Shock and Vibration Digest*, 1998, 30(2):91–105.
- [4] Maia N M M. Location of damage using curvature of the frequency response functions. *Proceedings of 15th IMAC, Florida*, 1997:942-946.
- [5] Alvandi, C. Cremona. Assessment of vibration-based damage identification techniques [J], *Journal of Sound and Vibration*, 2006, 292:179–202.
- [6] Peiying Gu, Houqun Chen, Tongchun Li, Chang Deng. Direct index method of damage location detection based on difference theory of strain modal shapes [J]. *Journal of vibration and shock*. 2006, 25(4):13-17. (In Chinese)
- [7] Yongmei Li, Xiangyu Gao, Yangshen Shi, Xiyuan Zhou. Damage diagnosis of space truss based on change of elemental strain modal [J]. *Journal of Building Structures*, 2009, (3):152-159. (In Chinese)
- [8] Manoj Kumar, R.A. Shenoi, S.J. Cox. Experimental validation of modal strain energies based damage identification method for a composite sandwich beam [J]. *Composites Science and Technology*. 2009, 69(10): 1635-1643.
- [9] Zhaodong Xu, Keyi Wu. Damage Detection for Space Truss Structures Based on Strain Mode under Ambient Excitation [J]. *Journal of Engineering Mechanics*. 2012, 138(10):1215-1223. (In Chinese)

Design analysis of steel frame for denitrification through existing structure

Cheng Liu^{1,a}, Pingzhou Cao^{1,b}

¹College of Civil and Transportation Engineering, Hohai University, Nanjing, Jiangsu, 210098, China

^aliucheng3009@163.com, ^bpzcao@hhu.edu.cn

Keywords: Frame for denitrification, Existing structure, Structural arrangement, Section optimization, Effective-length factor

Abstract. Construction of denitrification system is an important environmental engineering in power industry now. Denitrification system is always set over the blower bracket, frame for denitrification needs to pass through existing structure if blower bracket works together with boiler frame. Based on the denitrification project of a power plant in north China, this paper puts forward reasonable structural arrangement of steel frame through existing structure, which is that frame for denitrification works alone and the column affected by existing structure selects solid-web column with openings. The beam supporting SCR reactor could be simplified as a beam under dead load only. Optimal design of its section in simplified model can improve design efficiency and economize the cost. The critical load of special column with bracings can be obtained by the linear elastic buckling analysis and effective-length factor can be calculated according to Euler Formula.

Introduction

With the increase of environmental pressure and promotion of national policies, construction of denitrification system has been put on the agenda gradually among thermal power plants in China, which helps to control nitrogen oxide emissions. Flue gas denitrification projects are mainly reconstruction of old generation units at present, and there is no enough space for the generation units built earlier to install denitrification system. Due to the limited space, previous flue ducts and devices, denitrification system is always set over the blower bracket located between boiler and precipitator.

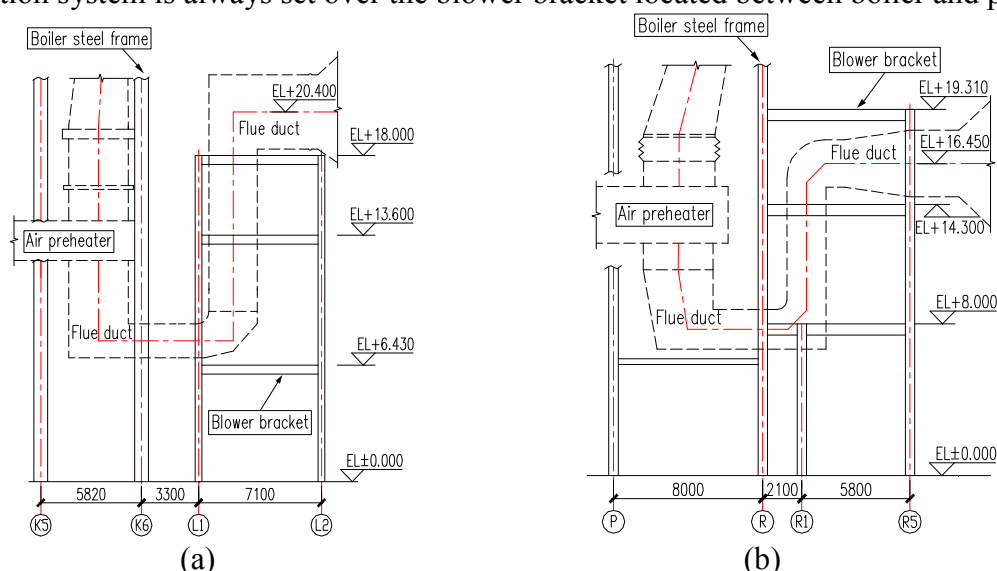


Fig.1 Blower bracket in actual engineering (a) individual loading pattern (b) combined loadings pattern

Selective Catalytic Reduction (SCR) denitrification reactor is supported by Steel frame. Compared to conventional steel bracket, steel frame for denitrification has such features as large span, tall height, heavy loads and its structural arrangement is easily affected by existing building [1]. The structure force system of blower bracket in actual engineering can be divided into two categories: individual loading pattern and combined loadings pattern (see Fig.1). There is some distance between blower bracket working alone and boiler steel frame (see Fig.1a), the structural arrangement of steel

frame for denitrification is flexible and this area could be used for building its foundations. Fig.1b shows that blower bracket works together with boiler steel frame, the space between the two is so narrow that newly-built columns may collide with existing horizontal members easily, and building foundations near boiler becomes more difficult. Based on the denitrification project of a power plant in north China, this paper discusses reasonable structural arrangement of steel frame for denitrification through existing structure and analyzes difficult problems encountered in design, providing technical references to similar projects.

Analysis of reasonable structural arrangement

General engineering situation. The coal-fired unit of a power plant designed by foreign design institute in the 1980s needs to install SCR denitrification system now. According to technological requirements of SCR denitrification and restriction of site conditions, the technological layout of denitrification system is shown in Fig.2. Due to the fact that blower bracket works together with boiler steel frame, newly-built steel frame needs to pass through existing structure so as to support denitrification facility. The design working life of steel frame for denitrification is 30 years and its seismic fortification category is class C.

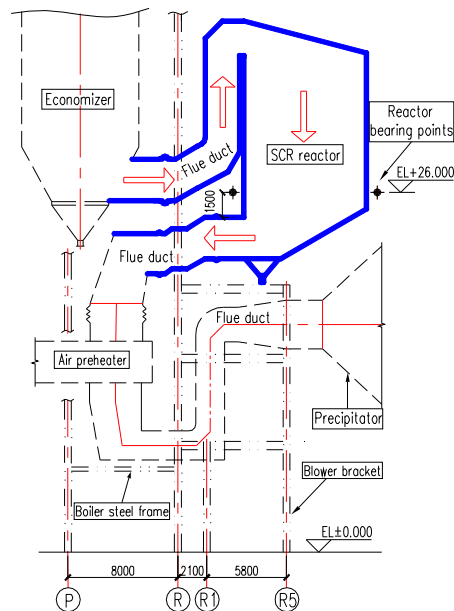


Fig.2 Technological layout of denitrification system

Comparison of different structural schemes. Based on field examination and reconnaissance, four structural schemes are put forward to satisfy technological requirements. The comparative analysis among them are as follows.

Scheme 1: As same as blower bracket, steel frame for denitrification works together with boiler steel frame, some new beams of which are connected to boiler axis-R steel columns. Only a row of columns are newly-built and the arrangement of columns is shown in Fig.3a. The implementation of this scheme can help to reduce foundation construction task and shorten construction period. In addition, the structural arrangement of new steel frame is very flexible. But this scheme has the following problems: checking the bearing capacity of existing members is difficult and checking results are unreliable for that the boiler's working load data can't be obtained; Boiler has been used for a long time, considering the settlement and earthquake resistance of buildings, it is not advisable that steel frame for denitrification works together with boiler frame [2]; connection between new and old member is complex and reinforcement task of boiler steel frame is huge.

Scheme 2: Steel frame for denitrification works alone and all columns are newly built. Columns in axis-A and boiler steel columns in axis-R share foundations with the distance of 1500 millimeters between the two. Beams in axis-2 of the blower bracket are located on three floors (EL+8.000, EL+14.300 and EL+19.310), which are supported at columns in axis-R on one end. If new column is

built at the intersection of axis-A and axis-2, it will collide with the three. So the two affected columns can be arranged in axis-2' to avoid the existing structure (see Fig.3b). The structure force system of steel frame for denitrification is completely independent in this scheme, which does not affect the mechanical behavior of boiler steel frame. Bearing capacity of original foundations under newly-increased loads may not meet the design requirements, and taking such reinforcement measures as extending foundation platform and adding piles is better than building new foundations in the limited area. However, the layout of two SCR reactors is asymmetric and flue gas flow fields in two reactors are different. Therefore model test of flue gas flowing in each reactor needs to be done separately, increasing the construction cost.

Scheme 3: The column built at the intersection of axis-A and axis-2 selects lattice column (see Fig.3c), three existing beams could pass through the gap between the two branches of lattice column. The rest is same as scheme 2. The layout of two SCR reactors is symmetrical and model test of flue gas flowing in SCR reactor needs to be done only once. But there are following problems in this scheme: difficulties in installing lattice column within the limited space, complex joint design and large amount of field welding work.

Scheme 4: The column built at the intersection of axis-A and axis-2 selects solid-web column with openings (see Fig.3c), and others are same as scheme 3. Three existing beams can pass through the openings of solid-web column. The column with openings is divided into four segments (see Fig.4). Considering the deviation of site construction and the settlement of existing building, size of opening should be bigger than section dimension of the beam through it so as to reserve the operation space for field welding. Compared to scheme 3, it only needs to reinforce the column with openings, beam-column joint design is simple and field welding work is less.

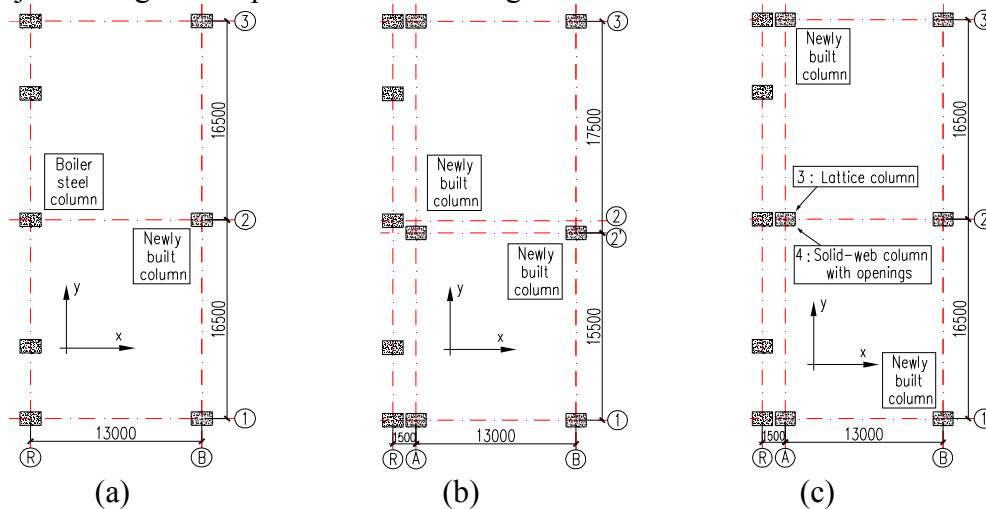


Fig.3 Arrangement of columns (a) scheme 1 (b) scheme 2 (c) scheme 3 and 4

According to the comparative analysis about safe reliability, construction cost and period, scheme 4 is selected as the structural arrangement of steel frame for denitrification.

Design analysis of steel frame

Analysis model. One generation unit should be equipped with two SCR reactors, each weight is approximately 580 tons, which are supported by two beams (EL+26.000) of steel frame for denitrification in the form of concentrated load. Using the truss is more economic and reasonable than beam for a large-span member under heavy loads. According to the technological layout, the maximum section height of left members supporting the SCR reactor should be less than 1500 millimeters (see Fig.2), so box-section beam could be selected to support the SCR reactor.

Beams can't be arranged in axis-A below EL+20.500 and axis-B between EL+16.000 and EL+26.000 due to the limitation of flue ducts. The columns located in the area are very long and slenderness ratio is not easy to meet the requirements. The effective length of member is related to the two-end constraint conditions and whether to add the intermediate support within it [3]. It is not economic that increasing section size of the columns and the beams connected with them to reduce

the slenderness ratio. Setting bracings between the columns could reduce the slenderness ratio effectively and the arrangement of bracings is shown in Fig.5.

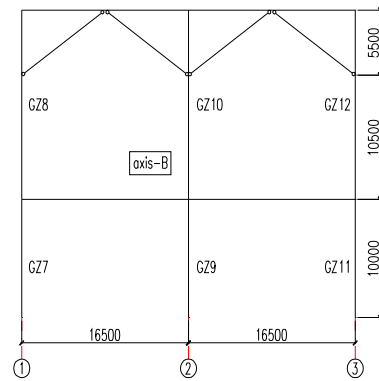
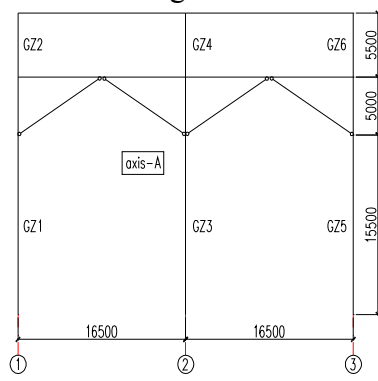
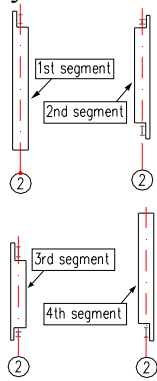


Fig.4 Column with openings

Fig.5 Arrangement of bracings between columns

Design of the beams supporting SCR reactor. The beam supporting SCR reactor occupies a large proportion of steel consumption of frame for denitrification, so optimal design of box beam section should be made to economize the cost. Considering that dead load the box beam supports is larger than live load, it can be simplified as a simply supported beam under dead load only (see Fig.6). The internal force of box beam is different in between integrated structural analysis model and simplified model, therefore $\sigma \leq 0.8f$ can be selected as the checking standard for bending strength of the beam in simplified model.

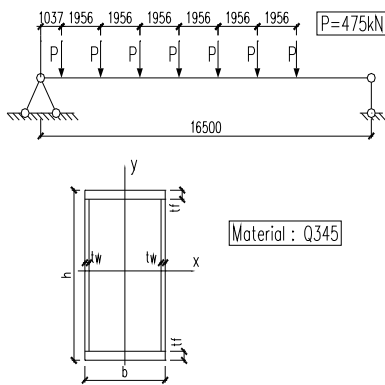


Fig.6 Simplified model for section optimization

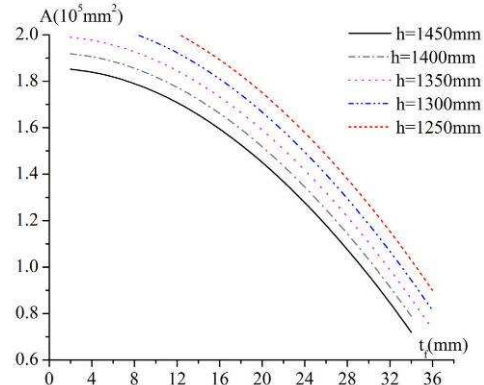


Fig.7 The plot $A-t_f$

Deflection limit value of the beam supporting SCR reactor is 41.25 millimeters according to relative design standard, so the maximum height of the beam should be less than 1458.75 millimeters in order to reserve the deformation space. The minimum height of the beam determined by the deflection requirement can be calculated by the expression given below [4].

$$h_{\min} = \frac{\gamma_x \cdot 0.8f \cdot l^2}{6.5E[\omega]} = \frac{1.05 \times 0.8 \times 295 \times 16500^2}{6.5 \times 2.06 \times 10^5 \times 41.25} = 1221[\text{mm}]. \tag{1}$$

According to checking standard for bending strength and flakiness ratio limit of compression flange, section optimization can be transformed to optimal solution of the expressions given below.

Objective function:

$$A = 2(h - 2t_f) \cdot t_w + 2bt_f. \tag{2}$$

Constraint function:

$$\begin{cases} \frac{M_{\max}}{1.05W_x} \leq 0.8f \\ \frac{b - 2t_w}{t_f} \leq 32 \sqrt{\frac{235}{f_y}} \end{cases} \tag{3}$$

where, $M_{\max} = 10587[\text{kN} \cdot \text{m}]$, $W_x = \frac{1}{6h}[bh^3 - (b - 2t_w)(h - 2t_f)^3]$, f is steel design strength and f_y is steel yield strength. Flange width b and web thickness t_w can be transformed to the expressions about flange thickness t_f by variable substitution. The plot $A-t_f$ shown in Fig.7 indicates that section area A decreases with the increase of h and t_f . Considering that flange is thicker than web in actual engineering, box $1450 \times 800 \times 22 \times 30$ is selected as the section of beam supporting SCR reactor. The strength-stress ratio of beam in simplified model is 0.755 and the deflection is 32.4 millimeters.

According to structural arrangement and selected section of members above, the integrated structural analysis model is built in SAP2000 software (see Fig.8). The control force combination for section design of the box beam is 1.35DL (short for dead load)+0.98LL (short for live load). The strength-stress ratio of the beam in the integrated model is 0.86 and the deflection is 34.2 millimeters, each of them meets the requirements of current design standard. Four beams supporting two SCR reactors consume 46.4 tons steel, which accounts for approximately 15% of the total steel consumption of frame for denitrification.

Effective-length factor calculation of special frame column. The method for effective-length factor calculation in current design standard is not fit for the columns located in the axis-A below EL+20.500 and the axis-B between EL+16.000 and EL+26.000. According to Euler Formula, effective-length factor can be calculated by the expression given below if the critical load of the member is obtained.

$$\mu = \sqrt{\pi^2 EI / (P_{cr} L^2)}. \quad (4)$$

The critical load of special column can be obtained by the linear elastic buckling analysis of the integrated structure. Linear bulking load is related to the axial force of members, so force combination which is 1.0DL+1.0LL could be selected as the load case of linear bulking analysis [5]. The critical load of special column is the product of axial force and critical load factor of the lowest buckling mode. The lowest buckling mode of special column can be identified by its obvious deformation, and Fig.8 shows the first buckling mode of steel frame for denitrification.

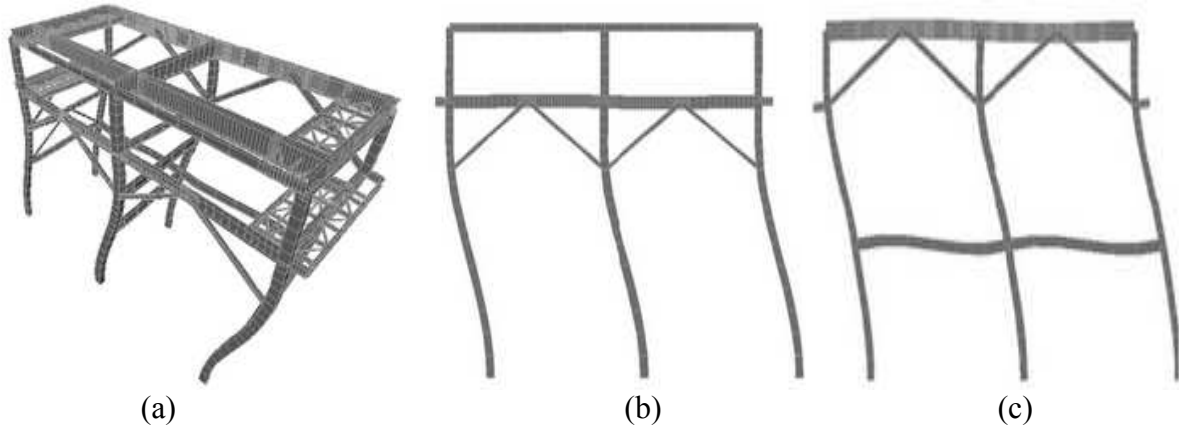


Fig.8 The first buckling mode of structure (a) integrated structure (b) axis-A (c) axis-B

The critical load and effective-length factor μ_y of special column are shown in Table 1. According to Code for Design of Steel Structures (GB 50017-2003), effective-length factor of the column with no bracings is also shown in Table 1. It indicates that setting bracings between long columns could reduce the slenderness ratio effectively.

Table 1 Effective-length factor calculation of special frame column

Special frame column		GZ1	GZ3	GZ8	GZ10
Critical load [kN]		40567.2	73711.4	28728.3	60370.4
Effective -length factor	Bracings	0.89	0.85	1.18	0.93
	No bracings	1.63	1.57	1.42	1.31

Conclusions

Through comparative analysis of safe reliability, construction cost and period among different schemes, it is considered to be a reasonable scheme that steel frame for denitrification works alone and the column affected by existing structure selects solid-web column with openings. Considering that dead load the beam supports is larger than live load, it could be simplified to a beam under dead load only. Optimal design of its section should be made in simplified model to improve design efficiency and economize the cost. Setting bracings between long columns could reduce the slenderness ratio effectively, but the method for effective-length factor calculation in current design standard is not fit for some of them. According to Euler Formula, effective-length factor can be calculated and the critical load of them can be obtained by the linear elastic buckling analysis of the steel frame for denitrification.

References

- [1] Guibo Luo and Xinliang Huang: Building Structure. Vol.43 SI (2013), p.410 (In Chinese)
- [2] Yaping Xu: China Construction Metal Structure. Vol.3 (2013), p.73 (In Chinese)
- [3] Ji Chen: Stability of Steel Structures Theory and Design (Science Press, China 2011). (In Chinese)
- [4] Jian Yao and Zhibin Xia: Steel Structures Behavior and Design (China Architecture & Building Press, China 2011). (In Chinese)
- [5] Qunchang Zhao: Special Structures. Vol.30 (2013), p.13 (In Chinese)

Design and Numerical Simulation on

Concrete two-way Slab Strengthened with partially Bonded Steel Plate

HU Jihong^{1,2, a} LI Xiucui^{2, b}

¹ School of Science, Wuhan University of Technology, Wuhan 430070, China)

² Design and Research institute, Wuhan University of Technology, Wuhan 430070, China)

^ahujh11@sina.com, ^b271516860@qq.com

Keywords: partially bonded steel , strengthen design, strength, stiffness, the numerical simulation

Abstract. Taking structure strengthen of a large hotel as the engineering background, based on superposition principle, put forward the design method of concrete two-way slab strengthened with partially bonded steel plate. According to the finite element analysis, the solid finite element model is established, and then the stress, strain and deflection of two-way slab strengthened with bonded steel plate is obtained, at the meantime compared with the load test datum in situ. The analysis results show that the finite element software is a reliable tool applied to analyze the design of two-way slab strengthened with bonded steel plate. When the increasing load is larger, partially bonding steel plate strengthening has more advantage and economize than bonding carbon fiber strengthening on two-way slab, meanwhile that slab strengthened with partially bonded steel plate has better mechanical properties, strength and stiffness.

Introduction

Bonding steel strengthening method is a common strengthening method. Its basic principle is that on the basis of the strengthening design using structure glue paste plate on the concrete structure surface, then the steel plate and the concrete structure can resist the load and deformation as a whole, so as to increase the bearing capacity and stiffness of structure.

In the existing concrete structure strengthening technology, bonding steel plate strengthening method has been applied more and more because bonding steel plate strengthening has many advantages such as that increasing the structure bearing capacity greatly, changing the structure weight and size small, decreasing construction period and so on. In recent years, the bonding steel strengthening concrete beam and slab has been more widely used in the world, and at the same time corresponding experimental and theoretical research has also made great progress. This shows that bonding steel strengthening method is a safe and reliable method, but the two-way concrete slab using partially bonding steel strengthening theory and practice are less^[1]. In this paper, a partially bonding steel plate strengthening concrete two-way slab was analyzed, so as to provide reference for the strengthening design in the future.

Two-way slab bonded steel plate strengthening design

A concrete structure hotel in Yichang, after the main structure completed, partially building using function changes as follows: 1. Expanding the area of some guest room, 2. Expanding the the area of some toilet. From above, increase partition wall is on the concrete floor, and partially guest room floor is took placed by bathroom with bath crock. According the hotel owner requirements, give up the lightweight plasterboard as partition wall material, and after comprehensive comparison, choose calcium silicon plate as guest room partition wall material whose density is 90 kilograms per square meter; and choose aerated concrete as toilet room partition wall material . By calculating, after increasing the partition wall, concrete slab in the original design can't bear the load, and must be strengthened.

When choosing strengthen method, through the comparison of two schemes such as strengthening with bonded carbon fiber and strengthening with bonded steel plate. When the bearing capacity of concrete slab is insufficient, strengthening with bonded carbon fiber is more used before, therefore bonding carbon fiber method is chosen firstly. Calculation result shows that there is need to bond two layers of carbon fiber cloth on the bottom of whole slab. Instead of bonding steel plate on the bottom of slab, by calculating, only bonding a few steel can meet the design requirements. The construction method of strengthened with bonding steel plate is more concise than with bonding carbon fiber, through comparison, finally decided to strengthen it with bonding steel plate.

When calculating bearing capacity of slab, the load is used to be generally uniformly distributed on the whole slab. But the strengthening method in this paper is partially bonding steel plate to strengthen slab on the bottom, so must select the new design method because the Design Code for Strengthening Reinforce Concrete Structures(GB50367-2006) is not introduce the strengthen method for this structure. Generally, elastic design method of concrete slab commonly is safe. So myopia using superposition principle, the load divided into two parts are applied to the slab in accordance with two orthogonal direction, and then the dosage of strengthening steel plate can be calculate according to specification method. The calculation figure is as follows Figure 1.

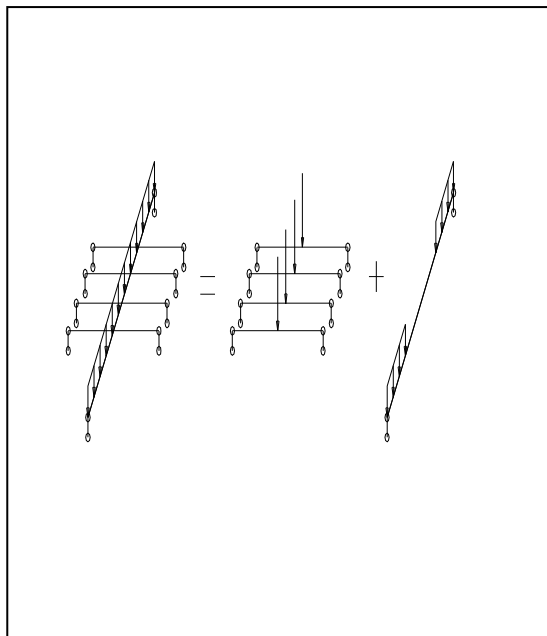


Figure 1 Load superposition figure

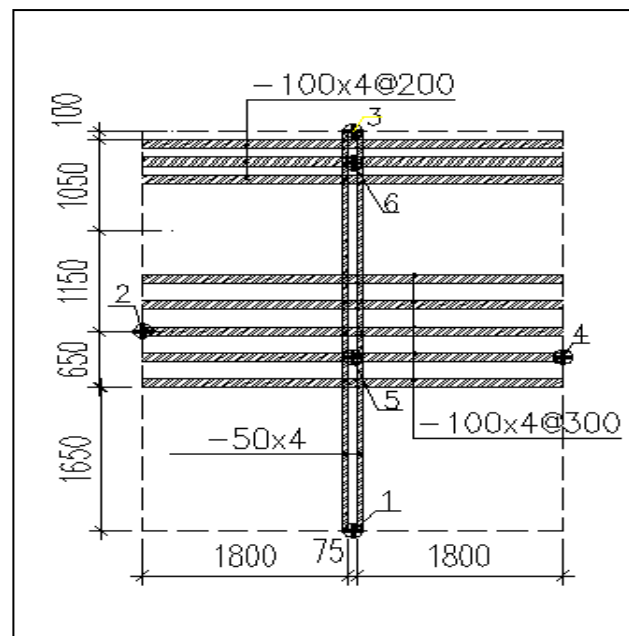


Figure 2 Bonding steel and test points arrangement

Through calculation, the result shows only ten pieces steel plates pasted on the bottom of slab by two across direction can meet the design requirements. Specific arrangement is as follows: along the partition wall bonding two piece steel plates which is 50 x4 @ 75, and reserved 75 millimeter place in the middle of concrete slab for bolt which fixing partition wall., at the same time bonding five piece steel plates which is 100 x4 @ 300 in the vertical direction in the middle, In the bath room bonding three piece steel plates which is 100x4 @ 200. Strengthen project detailed as figure 2.

Load test in situ

To verify the effect of the strengthening, the deflection test in situ on the structure is applied, and the development of cracks is observed, so as to get the actual stress of the concrete slab at working, and to provide necessary experimental datum for strengthen design theory and calculation method of slab.

The main content of this experiment is to test the deflection and deformation of the slab. Test point arrangement is as above figure 2, in which cross thick line is deflection test points), the deflection test using dial indicator.

There are two sub-areas for deferent load, the maximum load on first sub-area where putted bath crock is 10.3KN/m², and the maximum load is 6.5 KN/m² on other sub-area. Test load on the slab use grading way, loading sequence is as follows: 50%→70%→85%→95%→100%。

Pay close attention to the concrete slab in the process of loading, if there are any abnormal stop loading immediately lest destroy exist building. The deflection datum at the biggest load is as chart 1.

Load level	1	2	3	4	5
Deflection(mm)	1.67	2.05	2.34	2.54	2.65

In the process of loading, there are not visible cracks; the maximum deflection of slab is $L / 1396$ (L stands the short edge length of plate) which is far less than the code standard ($L/200$), test datum show that the slab stiffness meet the design standard . After unloading the maximum residual deflection value is 6.2%, which is less than 20% that is the standard permissible structure deformation value. The above datum can illustrate the slab is in the elastic work stage, and strengthening design is reliable, the bearing capacity of the slab can meet the design standard.

Bond steel strengthening slab numerical simulation

Material properties and parameter. The plane size of slab strengthened is 3700mm x4600mm, and thickness is 100 mm. The concrete strength grade is C30 ($f_c = 14.3$ MPa); the concrete elastic modulus is 3×10^4 MPa .concrete poisson's ratio is 0.2 [3]. Steel plate strength grade is Q235 - B ($f_y = 215$ MPa) . The elastic modulus is 2.05×10^5 MPa; poisson's ratio is 0.3 [4], the thickness of the steel plate is 4 mm, and width is 100mm and 50mm, arrangement of steel plates is as figure 2.

The establishment of the finite element model. Concrete is complex building material and can be simulate by solid65 element which is hexahedral unit at eight notes. When division concrete element, the mapping pattern is adopted, reinforcing steel bar in the slab is dispersion into the concrete model according to the specific volume rate. To simplify the strengthen steel plates into steel bar according the same cross-section area ,which is simulated by the Link8 element. When mesh steel bar element length of the steel bar is as same as the concrete element attached to steel bar, after establish independence model coupled with the concrete slab body. Due to the structure and the load is symmetric arrangement, so the finite element model can only established 1/2 model.

Because the building has not been put into use, at bonding steel plates the slab only bear gravity load, so can not consider stress hysteresis effect. When establishing the finite element model, the load is applying to the node on surface of slab, and steel bars and concrete are connect completely, and does not produce relative slip.

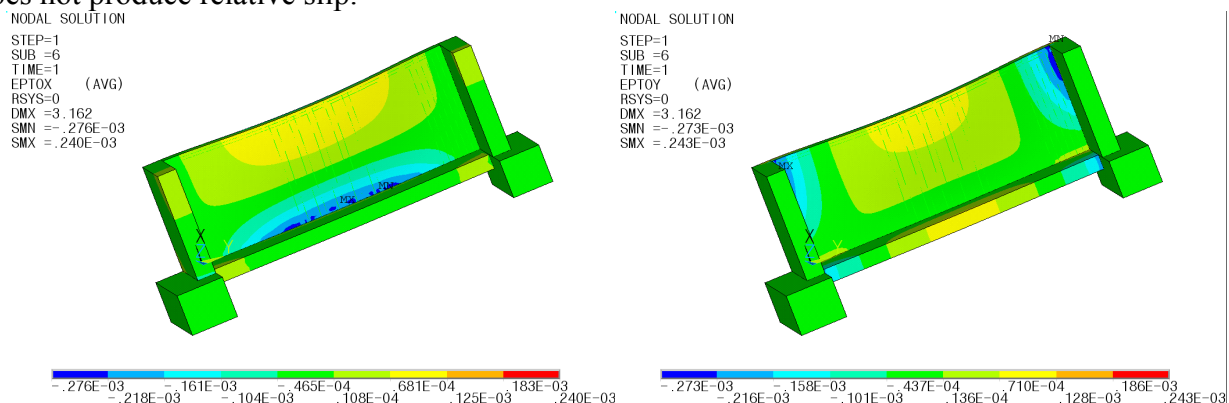


Figure 3 x direction strain at the bottom of the slab Figure 4 x direction strain at the bottom of the slab

The calculation results analysis. The X and Y direction strain at the bottom of the slab is as figure 3 and figure 4 respectively. Showing from the follow figures, the X and Y direction strain at the bottom

of the slab is far less than the yield strain of concrete which is 0.002, and concrete is in elastic working stage. So the slab has enough safety reserve.

The stress of the steel bars is in figure 5. The maximum first principal stress of steel bars is 25.559 N/mm² which is far less than the yield stress (210 N/mm²). So steel bars have certain safety reserve.

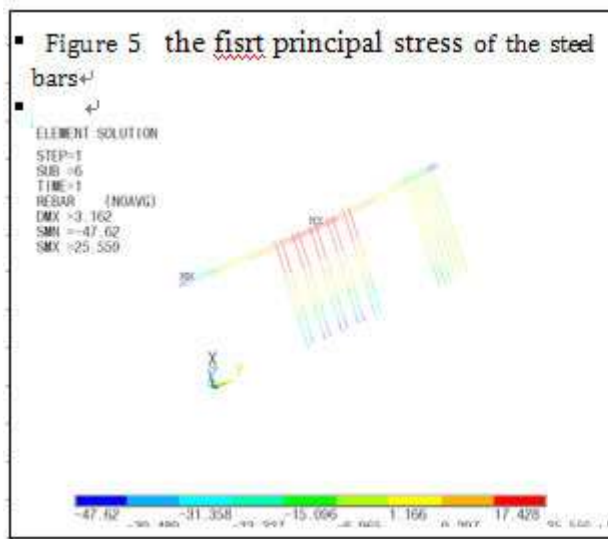
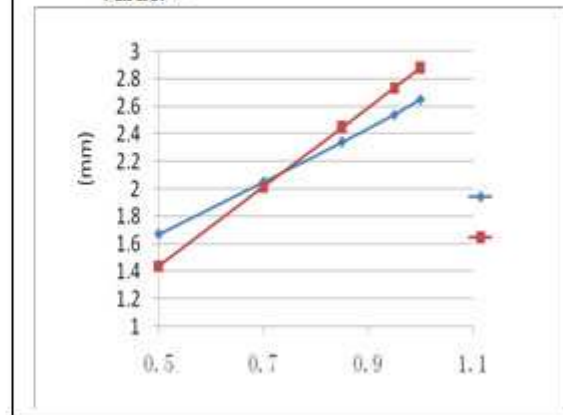


Figure 6 contrast of deflection test values and the finite element simulation value.



Deflection test values and the finite element simulation value at the central of the slab is contrast as in figure 6.

From above, with the increase of load ratio, the finite element simulation values and the test values are close to the linear growth. The slab strengthened has been working in elastic state when the load is reach maximum. At the first and second load grade in the process of loading simulation value is less than calculated value, but at the other load grades simulation value is greater than the test values. In the process of loading, the maximum deviation between the simulation value and the test values is 8.4%. The results show that using finite element software to check structure strengthening is reliable.

Conclusion

Based on the superposition principle, using partially bonding steel plate strengthening design method to strengthen concrete two-way slab, The load test and finite element numerical simulation show that the strengthened concrete slab was working in elastic stage, and not found visible cracks, which prove that the bearing capacity of the slab can meet the design requirement. The result shows that in some load condition the partially bonding steel plate strengthening slab is reasonable and reliable, which has certain economic advantage relative gluing carbon fiber strengthening when the increase load is bigger.

References

- [1] Zhang Jiwen ;Teng Jinguang; Lv Zhitao; Huang Yulong The Behavior Two-way Reinforced Concrete Slabs Externally Strengthened With Steel Plate To Subject Patch Load (China Civil engineering Journal, China 2002.04 p20~25)
- [2] Design Code for Strengthening Reinforce Concrete Structures (GB50367-2006) (China Building Industry Press, China ,2006)
- [3] Code for Design of Concrete Structures (GB50010-2010).(China Plan Press, China, 2010)
- [4] Code for Design of Steel Structures (GB50007-2003).(China Building Industry Press, China ,2003)

Discussion on the rationality simplified calculation method of reinforced concrete two-way slab

Shuzhi Liu

Inner Mongolia University of Science and Technology, Baotou 014010, China

nkdsz@sina.com

Key words: reinforced concrete slab; two-way slab; elastic analysis; plastic hinge line

Abstract: We analyzed the rectangular slab with four sides supported, respectively elastic and plastic methods of calculation the slab. Generally considered $l_2/l_1 \leq 2$ calculated as the two-way slab, $2 < l_2/l_1 < 3$ should be calculated as the two-way slab, however $l_2/l_1 \geq 3$ calculated as one-way slab, consider these provisions is not reasonable, analysis shows, if using elastic or plasticity theory analysis, $l_2/l_1 < 3$, or $l_2/l_1 < 4$ as the two-way slab. Otherwise, it is one-way slab. Reasonable distinction between one-way slab and two-way slab are meaningful, not only simplifies the calculation, but also makes the design economical, safe and reliable.

Introduction

Reinforced concrete slab is a common structural elements in civil engineering, its force calculation also works in one of the problems, engineering common slab is a rectangular slab, divided by the number of sides have the support shown in Figure 1.

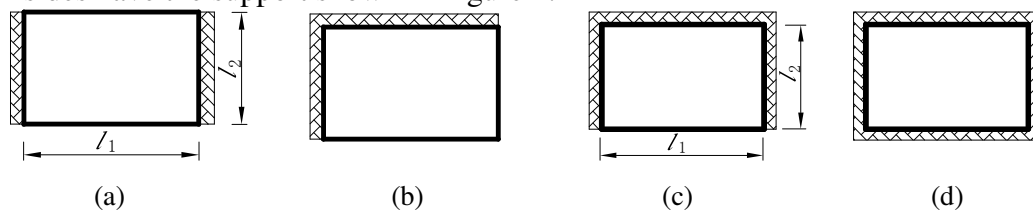


Fig. 1 Rectangular slabs

Of course, in addition to the rectangular slabs, there are circles, triangles and other forms; This article discusses only rectangular slab.

People are used to call unidirectional slab that the slab surface load transfer in one direction or the main pass in one direction, and is a one-way curved slab, otherwise known as two-way slab. For general uniform load, figure 1 (a) shows a one-way slab, and for (b), (c) and (d) three cases, however, according to two different edge length ratio l_2/l_1 , the number of passes in one direction load is changed, when l_2/l_1 reaches a certain value, loads transmitted primarily in one direction, slab in some way almost bent strip, its forces close to the one-way slab, think this slab can be used as one-way slab, greatly simplifies the design. The literature [1] considered $l_2/l_1 \leq 2$, calculated by two-way slab, when $2 < l_2/l_1 < 3$ should be calculated by two-way slab, $l_2/l_1 \geq 3$ calculated by one-way slab. Since $2 < l_2/l_1 < 3$ belongs to one-way or two-way slab is not clear, the actual design, simple to calculate, as one-way slab considered most. Therefore, the practical application, when $l_2/l_1 > 2$, it was calculated by one-way slab. This division slab method is simple, but too rough, although the safe side, but not economic, unreasonable, there is need for further analysis.

Elastic analysis of slab

Calculated simply supported slab. For simply supported elastic slab, let the deflected surface equation is $w = w(x, y)$, action uniformly distributed load q , deflection surface can be deduced from the differential equation [2].

$$D\left(\frac{\partial^4 w}{\partial x^4} + 2\frac{\partial^4 w}{\partial x^2 \partial y^2} + \frac{\partial^4 w}{\partial y^4}\right) = q \tag{1}$$

Where $D = \frac{Eh^3}{12(1-\mu^2)}$ is the bending stiffness of the slab; h is the slab thickness; μ is a Poisson's ratio; E is the modulus of elasticity. For the solution of Eq.1, general use inverse method, Navier and Levy solution, Navier solution which answers are re-trigonometric series, and its convergence is slow, therefore, in practical application is limited, Levy displacement function is a single trigonometric series, for simply supported slab calculation is simple, figure 2 simply supported slab, according to Eq.1, solved deflection surface equation [2]:

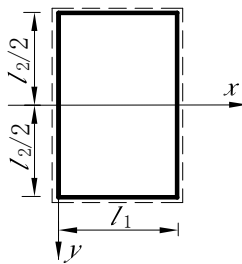


Fig. 2 Simply supported slab

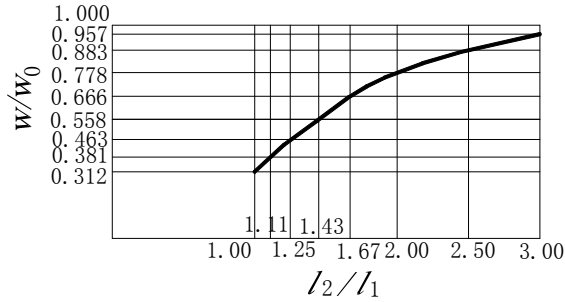


Fig. 3 Variation of deflection

$$w = \frac{4ql_1^4}{\pi^5 D} \sum_{m=1,3,5,\dots}^{\infty} \left(\frac{1}{m^5}\right) \left(1 - \frac{2 + \alpha_m \operatorname{th} \alpha_m}{2 \operatorname{ch} \alpha_m} \operatorname{ch} \frac{2\alpha_m}{l_2} y + \frac{\alpha_m}{2 \operatorname{ch} \alpha_m} \frac{2y}{l_2} \operatorname{sh} \frac{2\alpha_m}{l_2} y\right) \sin \frac{m\pi}{l_1} x \tag{2}$$

Where $\alpha_m = \frac{m\pi l_2}{2l_1}$; Such as taking Poisson's ratio $\mu=0$, $\frac{4ql_1^4}{\pi^5 D}$ is equal to one-way slab deflection

$w_0 = \frac{5ql_1^4}{384D}$, since $w_0 = \frac{4ql_1^4}{\pi^5 D}$, then the formula (2) simplification into:

$$w = w_0 \sum_{m=1,3,5,\dots}^{\infty} \left(\frac{1}{m^5}\right) \left(1 - \frac{2 + \alpha_m \operatorname{th} \alpha_m}{2 \operatorname{ch} \alpha_m} \operatorname{ch} \frac{2\alpha_m}{l_2} y + \frac{\alpha_m}{2 \operatorname{ch} \alpha_m} \frac{2y}{l_2} \operatorname{sh} \frac{2\alpha_m}{l_2} y\right) \sin \frac{m\pi}{l_1} x \tag{3}$$

Deflection at mid-span, $y = 0$, $x = l_1/2$, $\operatorname{ch} 0 = 1$, formula (3) becomes:

$$w = w_0 \sum_{m=1,3,5,\dots}^{\infty} \left(\frac{(-1)^{\frac{m-1}{2}}}{m^5}\right) \left(1 - \frac{2 + \alpha_m \operatorname{th} \alpha_m}{2 \operatorname{ch} \alpha_m}\right) \tag{4}$$

When $l_2/l_1 = 2$, $\alpha_m = m\pi$, maximum deflection center of the slab $w_{\max} = 0.7746w_0$, literature [3] gives $w_{\max} = 0.778w_0$, difference of 0.44%, when $l_2/l_1 = 2.5$, $\alpha_m = 1.25m\pi$, Solved $w_{\max} = 0.8795w_0$, when $l_2/l_1 = 3.0$, $\alpha_m = 1.50m\pi$, $w_{\max} = 0.9536w_0$, when $l_2/l_1 = 3.0$, the maximum deflection of the slab has been very close to the one-way slab deflection.

Slab moment calculation, $M_x = -D \frac{\partial^2 w}{\partial x^2}$, by the formula (3) Solution of

$$M_x = Dw_0 \frac{\pi^2}{l_1^2} \sum_{m=1,3,5,\dots}^{\infty} \left(\frac{1}{m^3}\right) \left(1 - \frac{2 + \alpha_m \operatorname{th} \alpha_m}{2 \operatorname{ch} \alpha_m}\right) \sin \frac{m\pi}{l_1} x \tag{5}$$

As can be seen $Dw_0 \frac{\pi^2}{l_1^2} = D \frac{4ql_1^4}{\pi^5 D l_1^2} \frac{\pi^2}{l_1^2} = 0.129ql_1^2$, corresponding simply supported slab at the maximum bending moment $M_{x0} = ql_1^2 / 8 = 0.125ql_1^2$, both values are very close,

$$Dw_0 \frac{\pi^2}{l_1^2} = 1.032M_{x0}, \text{ when } x = l_1 / 2,$$

$$M_{x\max} = M_{x0} \sum_{m=1,3,5,\dots}^{\infty} 1.032 \left(\frac{(-1)^{\frac{m-1}{2}}}{m^3} \right) \left(1 - \frac{2 + \alpha_m \operatorname{th} \alpha_m}{2 \operatorname{ch} \alpha_m} \right) \quad (6)$$

By the formula (6) and the formula (4) can be seen, two type of variation is the same, when $l_2/l_1=2$, using Eq. 6, calculation of bending moment $M_{x\max} = 0.7732M_{x0}$, exact solution $M_{x\max} = 0.772M_{x0}$, when $l_2/l_1=2.5$, $M_{x\max} = 0.8815M_{x0}$, $l_2/l_1=3.0$, $M_{x\max} = 0.9584M_{x0}$, variation of deflection shown in Figure 3.

Calculation of rectangular slab with four edges fixed

For the four sides of the fixed slab, the literature[3] indicates that $l_2/l_1=2.0$, the maximum deflection of the midpoint of the span $w_{\max} = 0.9715 \cdot \frac{ql_1^4}{384D}$, the maximum span deflection slab fixed at both ends of a one-way $w_0 = \frac{ql_1^4}{384D}$, be seen $w_{\max} = 0.9715w_0$, thus at this time, two-way cross-deflection slab is very close to the one-way span deflection of the slab. Cross the moment $M_{\max} = 0.96 \cdot \frac{1}{24} ql_1^2$, fixed at both ends of a one-way across the slab maximum moment $M_0 = ql_1^2 / 24$, $M_{\max} = 0.96M_0$, difference of 4.0%, also very close to one-way slab.

For simply supported rectangular slab and a fixed rectangular slab were analyzed, by similar analysis, in most cases $l_2/l_1 > 3$, internal forces close to the one-way slab. Four sides of the fixed slab $l_2/l_1 > 2.0$, calculated with high accuracy by the one-way slab, other cases $l_2/l_1 > 2.0$, by one-way slab calculation error is large, the maximum moment difference of 36%, when calculated using the theory of elasticity, $l_2/l_1 \geq 3$ calculated by one-way slab, otherwise shall be two-way slab. Should be noted, two-way slab computing is generally calculated look-up table, when $l_2/l_1 > 2.0$ often unable to look-up table, makes it difficult to calculate, when $l_2/l_1 > 2.0$, moment slowly change with l_2/l_1 , as can be seen from figure 3, changes in the moment as a straight line, the error is small, when $l_2/l_1=2$, moment to look-up table, when $l_2/l_1=3$, moment is calculated according to the one-way slab, when $2 < l_2/l_1 < 3$, moment is calculated by linear interpolation, so you can make up for deficiencies of incomplete data in the table.

Plastic analysis of slab

In addition to the calculation method of the elastic slab, there is a plastic calculation method, when calculated as the plastic method can obtain considerable economic benefits. In plastic calculation method, limit equilibrium method often used to slab, that plastic hinge line method, as shown in figure 4, acts uniformly distributed load q , span midpoint and supports ultimate moment was M_1 , M'_1 , M_2 , M'_2 , according to the principle of virtual work, solve the ultimate moment

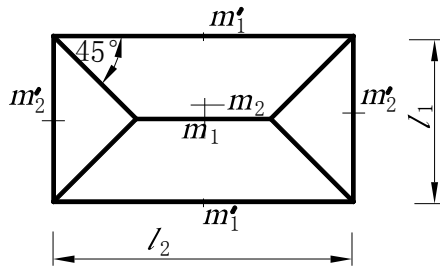


Fig. 4 Plastic analysis

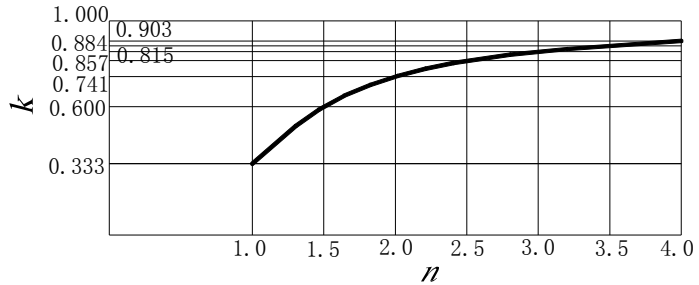


Fig. 5 $n-k$ diagram

$$m_1 = \frac{ql_1^2}{8} \cdot \frac{(n-1/3)}{(n\beta + \alpha\beta + n + \alpha)} \tag{7}$$

Where, $n=l_2/l_1$, $\alpha=M_2/M_1$, take $\alpha=1/n^2$, $\beta=M'_1/M_1=M'_2/M_2$, set up $\beta=2.0$, if $\beta=0$, it is the four sides simply supported plate. Put into $\alpha=1/n^2$, by the formula (7),

$$m_1 = \frac{ql_1^2}{8} \cdot \frac{(3n-1)}{(3n+3/n^2)} \tag{8}$$

Where, $ql_1^2/8$ is maximum moment of simply supported one-way slab m_0 , set up $k = (3n-1)/(3n+3/n^2)$, $m_1 = km_0$ for the four sides of the fixed plate, when $\beta=2.0$,

$$m_1 = \frac{ql_1^2}{24} \cdot \frac{(3n-1)}{(3n+3/n^2)} \tag{9}$$

Since $ql_1^2/24$ is maximum moment m_0 of fixed supported one-way slab, set up $k = m_1/m_0$, the relationship between k and n in Figure 5, analysis shows $l_2/l_1=4$, $k=0.91$, so $l_2/l_1 \geq 4$, calculated according to the one-way slab, that is economical and reasonable.

Summary

Accurate calculation two-way slab is very complicated, by using the appropriate method to divide the one-way and two-way slab can simplify the calculation, this paper argues that the elastic computing $l_2/l_1 \geq 3$, plastic calculation method $l_2/l_1 \geq 4$, calculated according to the one-way slab, otherwise, shall be calculated in accordance with the two-way slab, that is economic and security.

References

[1] Code for Design of Concrete Structures. (GB50010-2010) (in Chinese)
 [2] Xu Zhilun. Concise Guide of Elastic Mechanics. Higher Education Press (2006). (in Chinese)
 [3] Southeast University, etc. Concrete Structures. Higher Education Press (2006). (in Chinese)
 [4] Jiang Lei, Yai Jitao. Discussion on Several Provisions of Code for Design of Concrete Structure in Two-Way Slab. Sichuan Building Scienc. Vol. 37-03 (2011), 84-86 (in Chinese)
 [5] Shen Pushing. Floor Structure Design Principles. Science Press, 2003 (in Chinese)

Displacement Control Technology on High-rise Steel Structure about Main Power House of Thermal Power Plant

Liu Huanqin^{1a}, Li Weibin^{1b}, Ma Kang^{1c}

¹School of Civil Engineering, Southeast University, Nanjing 210096, China

^alhq_to@163.com, ^bliwbliwb@163.com, ^c380515287@qq.com

Key Words: intergration powerhouse, boiler frame, structural displacement, wind load, response spectrum, time history analysis

Abstract: With the background of optimal design study on main powerhouse of Power Plant, the finite element software ANSYS is adopted to control the overall structure's displacement. After the choice of structural form and loads bearing system, the static and dynamic characteristics of this boiler steel frame are analyzed in detail. And the structure's displacement response of this boiler steel frame will also be discussed under permanent load, wind load and seismic action. The structural displacement response causing by four wind load cases (front wind, back wind, left wind and right wind) is emphatically discussed and the dynamic characteristics and response spectrum analysis are also be studied. Results show that this main powerhouse owns good seismic performance and excellent lateral displacement resistance capacity because of the high structure stiffness. It shows that the horizontal displacement of the whole structure under all load cases can meet the requirements of the limit value, which demonstrates the feasibility of this structural program.

Introduction

As a result of the power plant main building layout pattern and the conventional difference is bigger, the structure system of the boiler room no longer as an independent existence, but with the framework to bear loads. Because of its overall structure is complex, uneven distribution of load, the bottom shear method in the boiler steel structure design specification is no longer suitable for integrated the main factory building structure.

The study more concentrated on high-rise steel structure in civil construction, compared with the civil buildings, high-rise industrial buildings have many differences, for example, more big industrial live load, the floor decorated with large equipment, the very irregular layout, sometimes the relatively high layer. structure often appear wrong layer phenomenon to meet the technological requirements, along the height distribution quality uniformity are destroyed because incomplete structure floor structure, reverse may occur under seismic action. Although the literature referred to the application of high-rise steel structure in industrial buildings, but the main building height is less than 50 m, in terms of design and the main reference to "technical specification for steel structure of tall buildings". In addition, both at home and abroad, there is no precedent which be of boiler steel frame body and joint framework plant as a whole to carry on the design in the main integrated workshop.

On the premise of meet the structure bearing capacity this paper research on relative displacement in main workshop. Through the analysis of the structural displacement response and verify the feasibility of the scheme, provide the basis for the application of the new power structure.

Finite element model of the main integrated factory building

Main comprehensive building adopts steel structure, the overall structure system selects the frame-support structure system.

The main integrated workshop longitudinal 12 across, Total length 128.50 m, the largest span 12.00 m, horizontal total length 91.30 m. The small workshop area, 1 to 13 axis and A to B axis into area, distance between A and B axis 34.00 m, the top level of A and B axis is 39.60 m and 40.20 m in Small workshop with slope roof.

The main high-rise building area, 1 ~ 13 axis and B ~ D axis into area, the transverse span 20.00 m. the distance B and C axis 6.00 m, the distance C and D axis 14.00 m, the top level of workshop 100.00 m.

Boiler area, 5 ~ 10 axis and K1 ~ K3 axis into area, the longitudinal length 58.00 m, the horizontal length 37.30 m. The main steel frame lies between 6 and 9 axis. Boiler steel with four rigid platform layer, the respectively elevation, 21.00 m, 52.00 m, 78.60 m and 110.19 m. Pillar elevation 135.90 m, boiler steel top elevation 143.00 m.

Boiler steel frame and joint frame plant distance of 8.60 m, mainly position to connect in four rigid layer. The main integrated workshop plane diagram, as shown in figure 1 a and b.

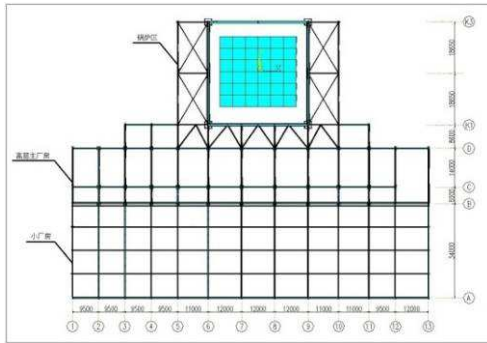


Fig. 1a Structure plane sketch

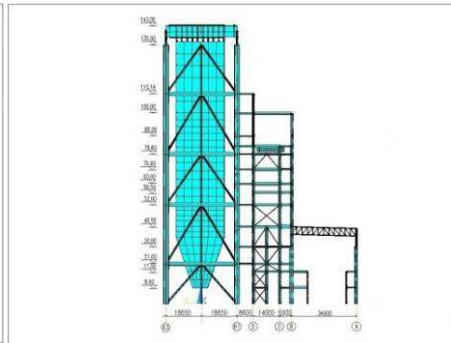


Fig. 1b Schematic structure façade

Boiler steel static analysis

Dead load effect analysis: Steel (including furnace) weight 250670 kN, Platform of constant total load 31526 kN. Boiler mainly produce vertical displacement and horizontal displacement is smaller in load under the action of gravity and platform. Finite element vertical displacement structure, as shown in figure 2a and b.

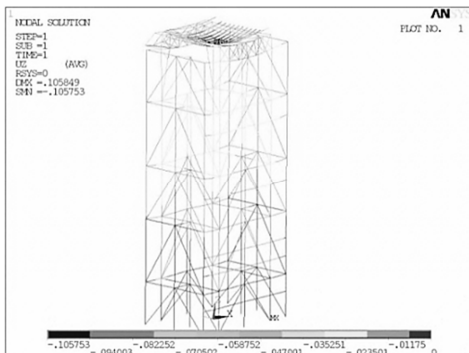


Fig. 2a Displacement to Z under the gravity action

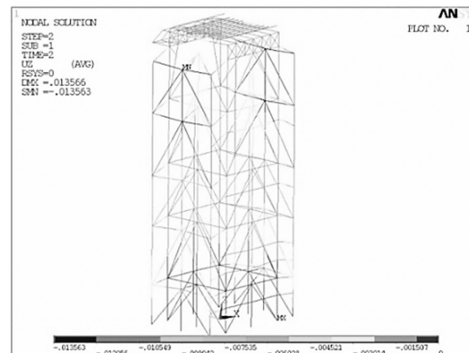


Fig. 2b Displacement to Z under constant load

Under the action of gravity, the maximal displacement on the middle of plate girders -0.106 m, the maximum displacement of the boiler steel frame 0.01 m to X, the maximum displacement of

0.015 m to Y, the displacement of the main steel 0.0036 m to Z. The boiler steel structure design code regulation, permanent loads, interlayer displacement permissible value for $h / 400$, structure displacement meet the requirements.

Analysis the influence of live load: Total live load of platform 70408 kN, live load of platform mainly for vertical load. The calculation results as shown in figure 3 a and b.

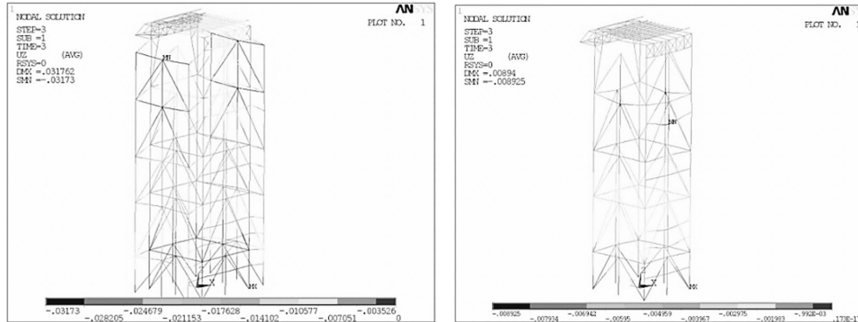


Fig. 3a Boiler steel integral displacement to Z Fig. 3b Main steel displacement to Z

Because the auxiliary steel frame stiffness is small, and the main steel frame stiffness is big, and live load acts on the platform layer rigidity between main steel frame and the auxiliary steel frame. So auxiliary steel produced by the displacement is greater than the main steel frame under the vertical load. Auxiliary steel maximum vertical displacement is -0.032m, The maximum displacement of the steel frame is 0.009 m.

The wind load is analyzed: In this project, boiler steel ontology is symmetric completely about the Y axis, the operation condition of the left and right wind is opposite, as a kind of wind conditions considered, Because the wind load of level, Z direction displacement is very small, no longer consider Z direction of displacement in the finite element analysis. The working condition of the wind finite element calculation results as shown in figure 4 a and b ~ 6 a, b.

(1) the wind load - before the wind

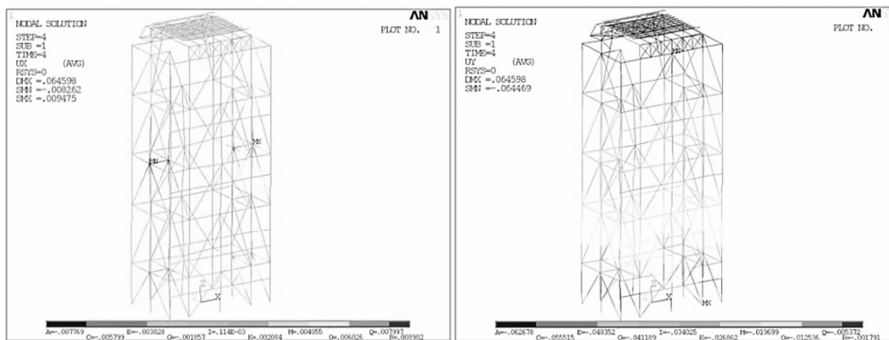


Figure 4a Boiler steel overall X direction displacement

Figure 4b Boiler steel overall Y direction displacement

The wind conditions, Boiler steel mainly produces Y direction displacement. X direction maximum displacement is 0.009 m, Y direction maximum displacement is 0.065 m, the main steel X direction maximum displacement is 0.009 m, Y direction maximum displacement is 0.064 m. The biggest displacement position of Y direction of structure : middle position of the wind suction surface roof truss side

(1) the wind load – after the wind

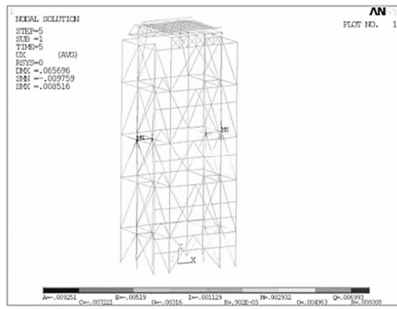


Figure 5a Boiler steel overall X direction displacement

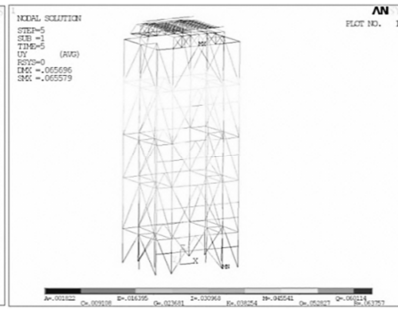


Figure 5b Boiler steel overall Y direction displacement

The wind conditions, X direction maximum displacement is 0.010 m, Y direction maximum displacement is 0.066 m, In the main steel frame, X direction maximum displacement is 0.09 m, Y direction maximum displacement is 0.066 m. The biggest displacement position of Y direction of structure : middle position of the wind pressure surface roof truss side.

(1) the wind load –Right (left) wind

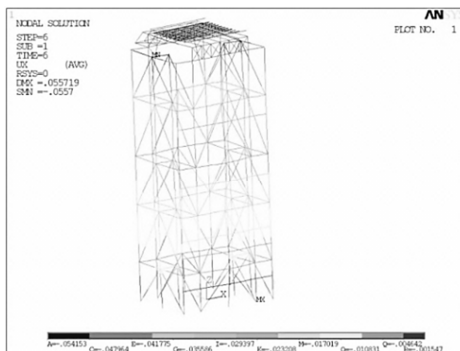


Figure 6a Boiler steel overall X direction displacement

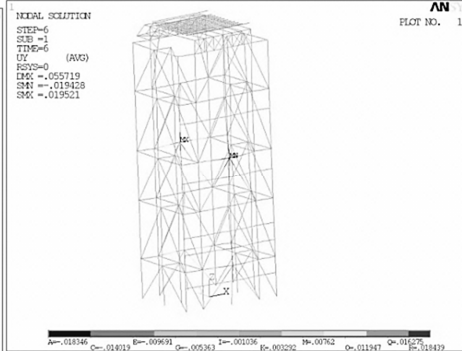
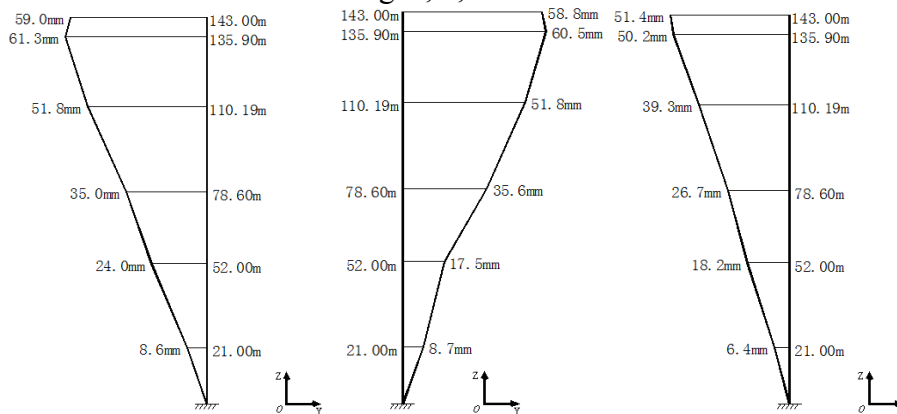


Figure 6b Boiler steel overall Y direction displacement

In this condition, boiler produces X displacement. The maximum displacement of X is 0.056m. The maximum displacement of Y is 0.019m. The X maximum displacement of mainly steel frame is 0.055. The maximum Y displacement is 0.019m. The Y maximum displacement position is at the top of the column which is in center of wind suction auxiliary steel frame.

The main steel box columns displacement curve Under wind loads: Take the main steel box columns in the main directions of the wind conditions arising from displacement, that is, anterior wind and posterior wind: UY; left and right wind: UX, summary and draw a displacement curve. Displacement curves are shown in Fig7a, b, c.



A former wind - box column B after the wind - box column C right (left) the wind UY displacement curve UY displacement curve column UX - box displacement curve

Figure 7 Displacement of main steel box columns under various wind conditions

From displacement curve of columns, you can see the boiler steel under wind loads, its deformation performs shear-bending. Between elevation +78.60 m and elevation +110.19 m, the maximum layer displacement is very big. Below 78.60m the structure deformation is mainly bending. Above 78.60m structural deformation is mainly play a shear, the frame systems play an important roles. Since the frame system and support system coordinated with each other, the whole deformation of structure is relatively smalln

According to the "boiler steel structure design" and "high steel Regulations" states: structures under wind loads, the allowable displacement values between layer is $h/400$.

By checking the displacement between layers are all meet the requirements. The results are shown in Table 1.

Table 1 Checking the structural layer displacement under wind conditions

Storey (m)	Displacement between the structural layer (m)	Allowable displacement between layers (m)	Storey (m)	Displacement between the structural layer (m)	Allowable displacement between layers (m)
21.00	0.0087	0.0525	31.59	0.0168	0.0780
31.00	0.0154	0.0775	25.71	0.0109	0.0643
26.60	0.0181	0.0665			

According to the "boiler steel structure design" and "high steel Regulations" provides that: In the permanent loads and wind loads, structural vertex horizontal displacement does not exceed $H/500$. Where H total height between the top of foundation and top of the column, It is.135.90 m. Vertex allowable displacement value is $135.90 \times 1000/500 = 271.8\text{mm}$. The maximum horizontal displacement of the structure under various loading conditions is 66mm \ll 271.80mm, therefore the structural displacement meet the requirements.

Boiler steel frame body response spectrum analysis

Finite element modeling and static calculation is basically the same, it need to take the constant load and live load of platform into structural quality.

The results of the analysis: because the structure is relative rules, Under the earthquake excitation, Previous order vibration mode in structure is mainly for translation, Didn't appear until the 10th order vibration mode when the torsional vibration mode, then translate into translational mode.

Due to lateral stiffness is larger than X to Y, X direction are easy to be inspired under the action of earthquake, as the first vibration mode. Translational motion of Y direction take second place.

The structure vibration mode distribution with conventional boiler steel does not consider the chamber differ from that of the vibration mode of distribution. In previous design, Despite the furnace load is great, Tend to just add the furnace in the form of load on the top of the big plate girder, Without considering the actual distribution of the center of gravity of the chamber of a stove or furnace will be beneficial to structural seismic, In fact between furnace and boiler steel plays a restraining each other, In fact the existence of the chamber of a stove or furnace structure torsional vibration mode is not easy to be inspired.

ANSYS response spectrum analysis:

In response spectrum analysis, Structural damping ratio is 0.035, Basic earthquake intensity is 7 degrees (0.10 g), α_{max} is 0.08. $T_g=0.9s$.

X direction structural response under seismic excitation (EX) :X direction maximum displacement is the 61.7 mm, The total displacement is 62.0 mm。 At the bottom of the structure of shear $F_X = 0.11459 \times 10^8 \text{ N} = 11459 \text{ Kn}$. Displacement finite element calculation results as shown in figure 8.

Y direction structural response under seismic excitation (EY) :X direction maximum displacement is the 6.0 mm, The total displacement is 52.2 mm, At the bottom of the structure of shear $F_Y = 0.12133 \times 10^8 \text{ N} = 12133 \text{ kN}$ 。 Displacement finite element calculation results as shown in figure 9.

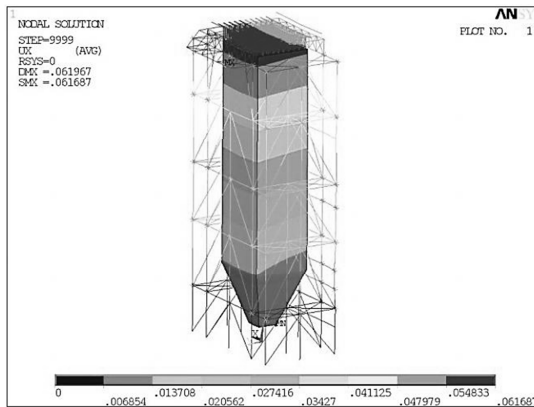


Figure 8 X direction displacement in X direction under the action of earthquake

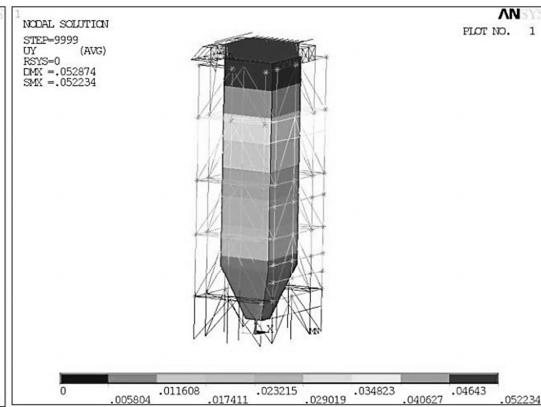


Figure 9 Y direction displacement in Y direction under the action of earthquake

Seismic action interlayer displacement is calculated: Specified in the specification, vertex displacement permissible value is $H / 400$ under the action of the earthquake。 Interlayer displacement permissible value is $h/300$ 。 The max Vertex displacement is 61.70 mm, clearly meet the requirements, Interlayer displacement calculation results are shown in table 2.

Table 2 Interlayer displacement calculation under seismic action

The height (m)	Structure displacement between layers (m)	Allow the interlayer displacement (m)	The height (m)	Structure displacement between layers (m)	Allow The interlayer displacement (m)
21.00	0.0063	0.0700	31.59	0.0168	0.1053
31.00	0.0154	0.1033	25.71	0.0109	0.0857
26.60	0.0181	0.0886			

Summary

1 Through the boiler steel body's static analysis, the maximum horizontal displacement of the structure under the different load conditions is 66mm, less than 271.80mm, which can meet the requirements well.

2 Through the boiler steel body's response spectrum analysis, the actual center of gravity will be conducive to the structure earthquake-resistant performance and the torsional vibration mode will not be easily excited.

3 Response spectrum analysis by ANSYS shows that the maximum top point's horizontal displacement is 61.70 mm, which also meets the specification's requirements.

Reference

- [1] Specification for design of boiler steel structures (GB/T 22395—2008) (In Chinese)
- [2] T.G. Zheng. *High-rise steel structure design* (Mechanical industry press,china2005) (In Chinese)
- [3] Load code for the design of building structures (GB 5009—2001) (In Chinese)
- [4] Finite element analysis of boiler steel structure's seismic dynamic characteristics, 2004. (In Chinese)

Dynamic analysis of tapered plates based on higher order beam theory

S.M. Ibrahim^{1,a}, Y.A. Al-Salloum^{1,b} and H. Abbas^{1,c}

¹Department of Civil Engineering, MMB Chair for Research and Studies in Strengthening and Rehabilitation of Structures, King Saud University, P.O. Box 800, Riyadh 11421, Saudi Arabia

^asrahim@ksu.edu.sa, ^bysalloum@ksu.edu.sa, ^cabbas_husain@hotmail.com

Keywords: Tapered plate, free vibration, higher order beam theory.

Abstract. Modal solutions of plates with uniformly varying cross section using unified beam theory are presented. The results are given in the form of Euler-Bernoulli, Timoshenko and quasi 3D solutions. Numerical results for cantilever and CFCF supported rectangular planform plates are presented. Different types of modes, *i.e.* axial, bending and torsional modes are observed. The frequency values are in good agreement with 3D finite element results as well as published literature. Due to uniform taper in plate cross section, bending vibration modes become asymmetric along the longitudinal axis of the structure. Further, it can also be noticed that the vibration behavior of thick tapered plates is characterized by the appearance of significant number of axial and torsional modes at lower frequency values.

Introduction

Vibration analysis of rectangular plates is necessary for designers to understand the dynamic behavior of many common structures. Studies on plates with variable geometric parameters have attracted interest of researchers not only because of the need for rational and economic profiling of structures but also due to specific shape requirements at certain locations. Cheung and Zhou [1] presented solutions for the natural frequencies of tapered plates with different boundary conditions using finite strip method. Differential quadrature method (DQM) in conjunction with First Order Shear Deformation Theory (FSDT) was employed by Malekzadeh and Karami [2] for the vibration analysis of non uniform thick plates on elastic foundations. Quintana and Nallim [3] used variational approach based on Reissner–Mindlin plate theory to analyze the free vibration of shear deformable polygonal plates with variable thickness. Manna [4] studied the free vibration of tapered plates using high precision triangular finite element. Only the frequencies corresponding to the first five bending modes of vibration were evaluated for different values of taper and aspect ratios. Employing extended Kantorovich method, Shufrin and Eisenberger [5] obtained frequency parameters for thick tapered plates using first and higher order shear deformation theories. It can be seen from the literature that the studies were limited to the vibration behavior of tapered plates considering only the first few lower frequency modes.

The objective of the present work is to obtain accurate frequency solutions of tapered vibrating plates using unified higher order beam theory [6]. Cantilever and clamped-free-clamped-free (CFCF) supported plates with linearly varying cross section are considered for the analysis. Different types of modes, *i.e.* axial, bending and torsional modes are observed. Three dimensional finite element analysis was also carried out using ANSYS. The frequency values are in good agreement with 3D finite element results as well as published literature.

Formulation

Geometry and the chosen coordinate system are given in Figure 1. y - axis is considered as the longitudinal axis and x - and z -axes describes the cross section represented by Ω . The beam boundaries over y are $0 \leq y \leq L_y$.

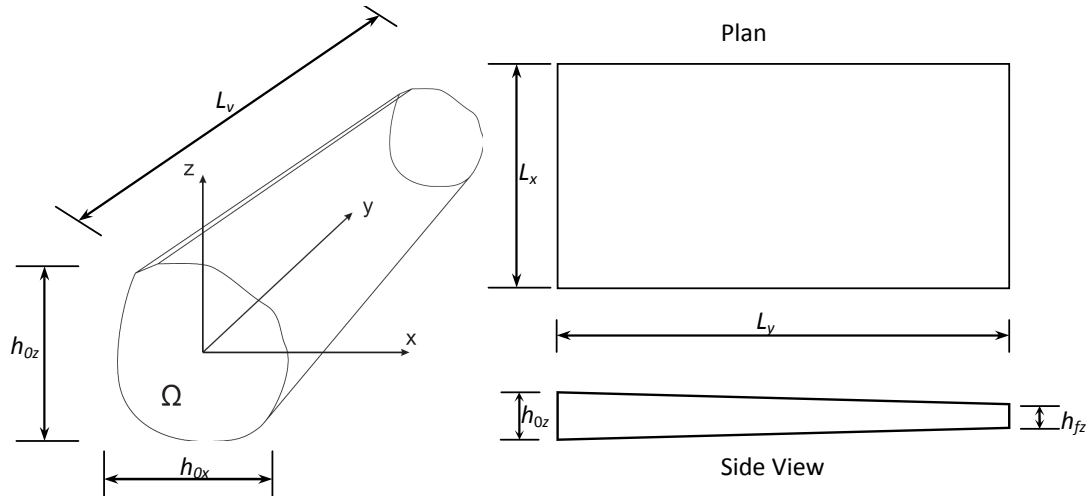


Fig. 1 Coordinate system and geometry of the tapered plate.

The displacement vector, representing the three displacement components, can be written as:

$$[\mathbf{u}_{(x,y,z)}] = [u_x \quad u_y \quad u_z]^T \quad (1)$$

Stress and strain components for any point $P_\Omega(x, y, z)$ can be given as [6]:

$$\begin{aligned} [\boldsymbol{\sigma}_p] &= [\sigma_{zz} \quad \sigma_{xx} \quad \sigma_{zx}]^T, & [\boldsymbol{\sigma}_n] &= [\sigma_{zy} \quad \sigma_{xy} \quad \sigma_{yy}]^T, \\ [\boldsymbol{\varepsilon}_p] &= [\varepsilon_{zz} \quad \varepsilon_{xx} \quad \varepsilon_{zx}]^T, & [\boldsymbol{\varepsilon}_n] &= [\varepsilon_{zy} \quad \varepsilon_{xy} \quad \varepsilon_{yy}]^T. \end{aligned} \quad (2)$$

The subscript n stands for terms lying on the cross section, while p represents the terms lying on reference planes which are orthogonal to Ω . The, strain-displacement and subsequently stress-strain relations:

$$[\boldsymbol{\varepsilon}_p] = [\mathbf{D}_p][\mathbf{u}], \quad [\boldsymbol{\varepsilon}_n] = [\mathbf{D}_n][\mathbf{u}] = ([\mathbf{D}_{n\Omega}] + [\mathbf{D}_{ny}])([\mathbf{u}], \quad (3)$$

$$[\boldsymbol{\sigma}] = \begin{Bmatrix} [\boldsymbol{\sigma}_p] \\ [\boldsymbol{\sigma}_n] \end{Bmatrix} = [\tilde{\mathbf{C}}][\boldsymbol{\varepsilon}], \Rightarrow [\boldsymbol{\sigma}_p] = [\tilde{\mathbf{C}}_{pp}][\boldsymbol{\varepsilon}_p] + [\tilde{\mathbf{C}}_{pn}][\boldsymbol{\varepsilon}_n], \quad [\boldsymbol{\sigma}_n] = [\tilde{\mathbf{C}}_{np}][\boldsymbol{\varepsilon}_p] + [\tilde{\mathbf{C}}_{nn}][\boldsymbol{\varepsilon}_n], \quad (4)$$

where $[\mathbf{D}_p]$, $[\mathbf{D}_n]$, $[\mathbf{D}_{n\Omega}]$ and $[\mathbf{D}_{ny}]$ are strain differential operators and $[\tilde{\mathbf{C}}_{ij}]$ are material constant relations. Now, in the displacement based formulation, the related displacement field is assumed as an expansion in terms of generic functions and can be written in compact form as:

$$[\mathbf{u}] = F_\tau[\mathbf{u}_\tau], \quad \tau = 1, N \quad (5)$$

where, $[\mathbf{u}_\tau]$ represents the introduced displacement variables of $P_\Omega(x, y, z)$ which lie on reference beam/plate surface Ω , F_τ are the introduced functions of coordinates x and z on the cross section and N is a free parameter which represents the number of terms in expansion. Maclaurin polynomial function is adopted for displacement field expansion. For example, considering expansion up to quadratic terms, the displacement field becomes:

$$u_x = u_{x1} + xu_{x2} + zu_{x3} + x^2u_{x4} + xzu_{x5} + z^2u_{x6}, \quad u_y = u_{y1} + xu_{y2} + zu_{y3} + x^2u_{y4} + xzu_{y5} + z^2u_{y6},$$

$$u_z = u_{z1} + xu_{z2} + zu_{z3} + x^2u_{z4} + xzu_{z5} + z^2u_{z6}. \tag{6}$$

From above equations, Timoshenko beam theory (TBT) and EBBT can be obtained [6]. By introducing the shape function N_i in the longitudinal direction and using cubic beam elements [7], the nodal displacement vector, $\mathbf{q}_{\bar{\alpha}}$ ($[\mathbf{q}_{\bar{\alpha}}] = [q_{u_{x\bar{\alpha}}} \quad q_{u_{y\bar{\alpha}}} \quad q_{u_{z\bar{\alpha}}}]^T$), and displacement field can be related as:

$$[\mathbf{u}_{\tau}] = N_i F_{\tau} [\mathbf{q}_{\bar{\alpha}}]. \tag{7}$$

The virtual variation of the strain energy can be written using Principle of virtual displacement and Eqs. (3), (4) and (7), in a compact format as:

$$\delta \Pi_{int} = \delta [\mathbf{q}_{\bar{\alpha}}^T [\mathbf{K}^{ij\tau\sigma}] \mathbf{q}_{\bar{\sigma}}], \tag{8}$$

where $[\mathbf{K}^{ij\tau\sigma}]$ is the stiffness matrix in the form of the fundamental nucleus. For illustration, the first component of the fundamental nucleus can be written as:

$$K_{xx}^{ij\tau\sigma} = \tilde{C}_{22} \int_{\Omega} F_{\tau,x} F_{s,z} d\Omega \int_{L_y} N_i N_j dy + \tilde{C}_{66} \int_{\Omega} F_{\tau,z} F_{s,z} d\Omega \int_{L_y} N_i N_j dy + \tilde{C}_{44} \int_{\Omega} F_{\tau} F_s d\Omega \int_{L_y} N_{i,y} N_{j,y} dy \tag{9}$$

The virtual variation of the work of the inertial loadings is:

$$\delta \Pi_{ine} = \int_V \rho [\ddot{\mathbf{u}}] [\delta \mathbf{u}]^T dV, \tag{10}$$

where ρ is the mass density; $[\ddot{\mathbf{u}}]$ represents double derivate of displacement with respect to time. In terms of displacement vector and mass matrix $[\mathbf{M}^{ijts}]$, the above equation can be rewritten as:

$$\delta \Pi_{ine} = [\delta \mathbf{q}_{\bar{\alpha}}^T [\mathbf{M}^{ijts}] \dot{\mathbf{q}}_{\bar{\sigma}}]. \tag{11}$$

Similar to $[\mathbf{K}^{ijts}]$, $[\mathbf{M}^{ijts}]$ is also in the form of 3×3 fundamental nuclei. Using the above equations, undamped free vibration problem can be solved as:

$$[\mathbf{M}][\ddot{\mathbf{a}}] + [\mathbf{K}][\mathbf{a}] = [\mathbf{p}], \tag{12}$$

where $[\mathbf{a}]$ is the vector of the nodal unknowns and $[\mathbf{p}]$ is the loadings vector. Natural frequency for the k^{th} modes, ω_k can be obtained by the following eigenvalues problem:

$$(-\omega_k^2 [\mathbf{M}] + [\mathbf{K}])(\mathbf{a}_k) = 0. \tag{13}$$

Numerical Results and Discussion

In this section, natural frequencies of vibrating plates based on the different theories are discussed which are expressed in terms of the frequency factor $\lambda = \omega L_x^2 (\rho h_{0z} / d_0)^{1/2} / \pi^2$, where ω is the natural frequency, L_x is the length of the plate along x - axis; h_{0z} is the initial thickness and $d_0 = Eh_0^3 / (12(1-\nu^2))$. For validation purposes, cantilevered plates having aspect ratio (L_y/L_x) of 2.0 and taper ratio (h_{fz}/h_{0z} ; where h_{fz} is the thickness of plate at $y = L_y$) as 0.5 with thickness ratio (h_{0z}/L_x) = 0.3 are considered and the first five frequency factors along with the mode types (a – axial; z – bending along z - axis; t – torsional) are given in Table 1. Present results are confirmed with ANSYS 3D solutions and with the available results [5]. Because of the displacement field considered along three axes, even the results obtained using classical theories predict in-plane modes (a -axial modes; z - bending modes in z axis).

However, twisting type modes come in to picture only with theory expansion order $N > 1$. It can be seen that results obtained using $N = 4$ gives comparable results with that of obtained using ANSYS 3D as well as with published results. Results for CFCF plates with $h_{0z}/h_{fz} = 0.5$ and $L_y/L_x = 2.0$ are given in Table 2. It can be seen from Table 2 that frequency values are matching very well with ANSYS 3D results. It can be observed that in-plane modes come up earlier as compared to that of the previous case. Also, except for the first few modes, it can be seen that different types of modes appear in narrow band of frequency.

Table 1: Frequency factors λ for cantilever taper plates with thickness variation in y direction.

h_{0z}/L_x	Mode	EBBT	TBT	$N = 1$	$N = 4$	ANSYS 3D	Ref. [5]
0.3	1	0.0918	0.0909	0.0909	0.0924	0.0929	0.0941
	2	0.3287 ^z	0.2949 ^z	0.2949 ^z	0.2920 ^z	0.2927 ^z	-
	3	0.4344	0.4150	0.4150	0.2997 ^t	0.2985 ^t	0.2980
	4	0.9999 ^a	0.9999 ^a	0.6275 ^t	0.4193	0.4229	0.4261
	5	1.0987	1.0009	0.8202 ^a	0.7722 ^t	0.7714 ^t	0.7731

Table 2: Frequency factors λ for CFCF taper plates with thickness variation in y direction.

h_{0z}/L_x	Mode	EBBT	TBT	$N = 1$	$N = 4$	ANSYS 3D
0.3	1	0.3931	0.3703	0.3703	0.3779	0.3787
	2	1.0646	0.9163 ^z	0.9163 ^z	0.5746 ^t	0.5719 ^t
	3	1.5941 ^z	0.9455	0.9455	0.8804 ^z	0.8799 ^z
	4	1.7431 ^a	1.7041	1.0832 ^t	0.9542	0.9610
	5	2.0344	1.7431 ^a	1.4517 ^a	1.2278 ^t	1.2266 ^t
	6	3.2548	1.7994 ^z	1.7041	1.6812	1.6414
	7	3.5015 ^a	2.5824	1.7994 ^z	1.7079 ^z	1.7274 ^z
	8	3.5256 ^z	2.8795 ^z	2.1724 ^t	1.7343 ^a	1.7341 ^a
	9	4.6787	3.0813 ^z	2.5824	1.7600 ^a	1.7618 ^a
	10	5.2569 ^a	3.5015 ^a	2.8760 ^a	1.9920 ^t	2.0001 ^t

Conclusions

Different types of modes, *i.e.* axial, bending and torsional modes are observed in the modal solutions of plates using unified beam theory. Results are in good agreement with 3D finite element analysis and available results. Due to uniform taper in plate cross section, bending vibration modes become asymmetric along the longitudinal axis.

Acknowledgements

The authors acknowledge the technical support provided by MMB Chair for Research and Studies in Strengthening and Rehabilitation of Structures, Dept. of Civil Engineering, King Saud University.

References

- [1] Y.K. Cheung and D. Zhou D: Journal of Sound and Vibration Vol.260 (2003), p. 693–709.
- [2] P. Malekzadeh G. Karami: Engineering Structures Vol. 26 (2004), p.1473–1482.
- [3] M.V. Quintana and L.G. Nallim: Applied Acoustics Vol. 71 (2010), p. 393– 401.
- [4] M.C. Manna: Journal of Vibration and Control Vol.18 (2012), p. 76–91.
- [5] I. Shufrin and M. Eisenberger: Journal of Sound and Vibration Vol. 290 (2006), p. 465–489.
- [6] E. Carrera, G. Giunta and M. Petrolo: Beam structures: classical and advanced theories. (John Wiley & Sons, US 2011).
- [7] K.J. Bathe: Finite element procedure. (Prentice Hall of India, India 1996).

Effect of Loading Pattern on Performance of FRP-HSC-Steel Double Skin Tubular Columns

Butje Alfonsius Louk Fanggi^{1,a} and Togay Ozbakkaloglu^{1,b}

¹School of Civil, Environmental and Mining Engineering, The University of Adelaide, Adelaide, South Australia, Australia 5005

^abutje.loukfanggi@adelaide.edu.au, ^btogay.ozbakkaloglu@adelaide.edu.au

Keywords: Fiber reinforced polymer (FRP); High-strength concrete (HSC); Confinement; Columns; FRP tubes; Steel tubes; DSTCs.

Abstract. This paper reports on part of an ongoing experimental program at the University of Adelaide on FRP-concrete-steel double-skin tubular columns (DSTCs). The main emphasis of the study reported in this paper was to investigate the influence of loading pattern on the axial compressive behavior of DSTCs. To this end, 12 hollow and concrete-filled DSTCs were manufactured and tested under monotonic or cyclic axial compression. All of the specimens were manufactured using high-strength concrete (HSC). The results of the experimental study indicate that that concrete in cyclically loaded hollow DSTCs exhibits slightly larger strength and strain enhancement ratios than concrete in companion monotonically loaded DSTCs. The results also indicate that concrete in filled DSTCs exhibit slightly larger strength enhancement ratios than and similar strain enhancement ratios to concrete in monotonically loaded DSTCs.

Introduction

Over the last two decades, the use of fiber reinforced polymer (FRP) composites as a confinement material has received a great deal of attention as demonstrated in a recent review by Ozbakkaloglu et al. [1]. The success attained in using FRP as a concrete confinement has provided increased impetus for research into two main research directions: 1) the performance of FRP composites in retrofitting existing concrete columns (e.g., [2-3]); and 2) the construction of new high-performance composite columns in the form of concrete-filled FRP tubes (CFFTs) (e.g., [4-13]). Following from the research on CFFTs, a new type of composite system was proposed by Teng et al. [14] in form of FRP-concrete-steel double-skin tubular columns (DSTCs). This composite system consists of a steel tube inside a FRP tube with concrete in between, and combines the advantages of all three materials to achieve a high-performance structural member. The performance of this composite system has been investigated extensively by the research group led by Teng in Hong Kong [14-16] and the second author in Australia [17-19]. The results of these studies demonstrated that concrete in DSTC is confined very efficiently, which in turn leads to a highly ductile member behavior. However, the studies on the comprehensive behavior of DSTCs have so far focused on the behavior under monotonic loading, and only two studies investigated the behavior of DSTCs under cyclic axial compression [16,18], with each reporting on only three pairs of specimens. Additional studies are, therefore, required to better understand the influence of loading pattern on the compressive behavior of DSTCs.

To this end, this paper presents the results of an experimental program that was aimed at investigating the behavior DSTCs under monotonic and cyclic axial compression. The results of the experimental program are first presented and followed by a discussion on the influence of loading pattern on the compressive behavior of FRP-high-strength concrete (HSC)-steel DSTCs.

Test Program

Test Specimens and Materials. A total of 12 specimens including hollow and filled DSTCs that were confined by FRP tubes were prepared and tested under monotonic and cyclic compression. The FRP tubes were formed using a manual wet lay-up process by wrapping epoxy resin impregnated the fiber sheets around precision-cut high-density Styrofoam templates in the hoop

direction. The outer tubes of the specimens were made of 6 layers of S-glass fiber sheets, with nominal ply thickness of 0.2 mm, ultimate tensile strength of 3040 MPa, and ultimate tensile strain of 3.5%. A formwork was developed and used to support the tubes during the process of concrete pouring to ensure the FRP and steel tubes remained concentric. The specimens had a diameter of 152.5 mm, measured at the concrete core, and a height of 305 mm. Two nominally identical specimens were tested for each unique specimen configuration. Details of the specimens are shown in Table 1.

Table 1. Properties of test specimens

Specimens	Number of FRP layers	Strength of concrete, f'_c (MPa)	Steel tube diameter, D_s (mm)	Steel tube thickness, t_s (mm)	DSTC type	Loading type
DSTCs 1 & 2			60.3	3.6	Hollow	Monotonic
DSTCs 3 & 4	6	96.2	88.9	3.2	Hollow	Monotonic
DSTCs 5 & 6			88.9	3.2	Filled	Monotonic
DSTCs 1C & 2C			60.3	3.6	Hollow	Cyclic
DSTCs 3C & 4C	6	82.4	88.9	3.2	Hollow	Cyclic
DSTCs 5C & 6C			88.9	3.2	Filled	Cyclic

Two different HSC mixes were used in the manufacture of the specimens. Both mixes consisted of crushed bluestone as the coarse aggregate with a nominal maximum size of 10 mm, and silica fume added at 8 percent of the binder content by weight. The average unconfined concrete strengths (f'_c) attained during the period of testing are shown in Table 1, together with the corresponding axial strain (ϵ_{co}) calculated using the expression given by Popovics [20].

Instrumentation and Testing Procedures. For each specimen, four linear variable differentiated transformers (LVDTs) were used to measure axial deformation of the specimens, which were mounted at the corners between the loading and supporting steel plates of the compression test machine. The recorded deformations were used in the calculation of the average axial strains along the entire height of the specimens.

The specimens were tested under concentric compression using a 5000-kN capacity universal testing machine. The initial elastic portion of the monotonic and cyclic loading and the unloading/reloading cycles of the cyclic loading were performed with the load control at 3 kN per second, whereas displacement control was used at approximately 0.003 mm per second beyond initial softening, and for the segments between each unloading/reloading curve. Specimens were subjected to a single unloading/reloading cycle that was applied at approximately 0.25% axial strain intervals. Prior to testing, a capping process was completed at both ends of all specimens to ensure uniform distribution of the applied pressure, and the load was applied only to the concrete core and inner steel tube through 15-mm thick and 150-mm diameter precision-cut high-strength steel loading discs placed at each end of the specimens.

Test Results

Axial Stress-Strain Behavior. The axial stress of concrete inside the DSTCs was calculated by dividing the axial load resisted by the concrete (P_c) with the net cross-sectional area of the concrete section. The load applied to the concrete was determined by subtracting the axial load resisted by the steel tube (P_s) for a given axial strain, from the total load resisted by the DSTC (P_T) at the same axial strain. The load acting on the steel tube was calculated by assuming that the load-strain behavior of the steel tube inside a DSTC is similar to the load-strain behavior of the corresponding unconfined steel tube obtained from a compression test. The ultimate axial stress (f'_{cu}) and strain (ϵ_{cu}) of the concrete inside DSTCs were calculated using the approach summarized in this section and are given in Table 2.